Journal of Energy Storage 101 (2024) 113863

Contents lists available at ScienceDirect

Journal of Energy Storage

journal homepage: www.elsevier.com/locate/est

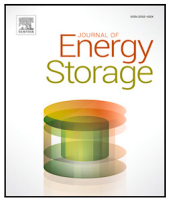

Review article

# Review of recent progress in sintering of solid-state batteries: Application and modelling

Amirreza Sazvar [a], Masoumeh Hajibandeh [a], Pariya Vafaei [b], Elham Hosseinzadeh [c], Masoud Jabbari [d,*]

[a] School of Metallurgy and Materials Engineering, Iran University of Science and Technology, Tehran, Iran
[b] School of Metallurgy and Materials Engineering, University of Tehran, Tehran, Iran
[c] School of Physics, Engineering and Technology, University of York, York, YO10 5DD, UK
[d] School of Mechanical Engineering, University of Leeds, Leeds, LS2 9JT, UK

## ARTICLE INFO

*Keywords:*
Solid-state batteries
Cold sintering
Flash sintering
Modelling

## ABSTRACT

The increasing demand for advanced energy storage solutions has fuelled an increasing need for cutting-edge technologies that can provide high battery capacity, safety, and environmental sustainability. This comprehensive review article embarks on an exploration of the latest advances in solid-state batteries, offering a panoramic view of their evolution. Another pivotal aspect of this review is an in-depth analysis of recent advancements in battery materials sintering techniques, with a particular focus on cold sintering and flash sintering. By delving into the fundamental principles of sintering, we illustrate the substantial potential of these innovative methods in shaping the future of energy storage technologies. These techniques are instrumental in streamlining the manufacturing process of solid-state batteries, making them more efficient and sustainable. Additionally, the review extends its scope to encompass the modelling of these sintering processes, emphasising their helpful role in the sintering of solid-state batteries. Furthermore, the article ventures into the modelling of solid-state batteries, introducing the powerful tool of machine learning to enhance the understanding and optimisation of these advanced energy storage systems. This synergy between modelling and machine learning promises to expedite the development of robust and cost-effective solid-state batteries.

**Contents**



* Corresponding author.
*E-mail address:* m.jabbari@leeds.ac.uk (M. Jabbari).

https://doi.org/10.1016/j.est.2024.113863
Received 29 May 2024; Received in revised form 24 August 2024; Accepted 19 September 2024
Available online 26 September 2024

**List of Abbreviations**

| | |
|---|---|
| SSBs | Solid-state batteries |
| LIBs | Lithium-ion batteries |
| LCO | Lithium cobalt oxide |
| NCA | Lithium nickel cobalt aluminum oxide |
| NMC | Lithium nickel cobalt aluminum oxide |
| LMO | Lithium manganese oxide |
| LNMO | Lithium nickel manganese oxide |
| TM | Transition metal |
| ZTO | $ZrTiO_4$ |
| LLZO | $Li_7La_3Zr_2O_{12}$ |
| NASICON | sodium (Na) super ionic conductor |
| LATP | $Li_{1.3}Al_{0.3}Ti_{1.7}(PO_4)_3$ |
| SPS | Spark plasma sintering |
| SE | Solid electrolyte |
| PDMS | Polydimethyl-siloxane |
| MCI | Mixed conducting interphases |
| CAM | Cathode active materials |
| CEI | Cathode electrolyte interphase |
| HBs | Heterogenous blocks |
| ISCs | Internal short circuits |
| DRT | distribution of relaxation times |
| AIMD | Ab Initio Molecular Dynamics |
| DFT | Density Functional Theory |
| ML | Machine learning |
| SVM | Support vector machine |
| SVR | Support vector regression |
| RUL | Remaining useful life |
| GPR | Gaussian process regression |
| EN | Elastic net |
| FAST | Field Assisted Sintering Technology |
| VLC | Volatile lithium compounds |
| HP | Hot pressure |
| OPS | Oscillatory pressure sintering |
| NZSP | $Na_3Zr_2Si_2PO_{12}$ |
| CSP | Cold sintering process |
| ICC | Inverse co-precipitation and compaction |
| UCS | Uniaxial Cold Sintering |
| PEO | Plyethyleoxide |
| PVDF | Polyvinylidene fluoride |
| CNF | Carbon nanofibre |
| HEVs | Hybrid electric vehicles |
| FS | Flash sintering |
| RFS | Reactive flash sintering |
| DC | Direct current |
| AC | Altering current |
| KNN | Potassium Sodium Niobate |
| FSPS | Flash spark plasma sintering |
| ERFS | Electric resistance flash sintering |
| SLFS | Selective laser flash sintering |
| AI | Artificial intelligence |
| ML | Machine learning |

## 1. Introduction

Solid-state batteries (SSBs) have emerged as a promising solution to revolutionise various sectors, including electric vehicles (EVs), renewable energy systems, and portable electronics [1,2]. Their higher energy density allows them to store more energy in a smaller space. SSBs are also considered safer than conventional options due to their inherently non-flammable properties. Enhanced safety is essential, especially with the growing demand for reliable, efficient energy storage solutions. Moreover, these batteries boast longer lifetimes due to their robust construction. Despite these promising attributes, SSBs have faced obstacles [3,4]. Issues related to manufacturing challenges and cost concerns have slowed down market penetration. However, ongoing research and development efforts aim to address these barriers and bring SSBs closer to realising their full potential in transforming energy storage systems [5].

As demand for advanced energy storage solutions increases, SSBs require efficient and cost-effective manufacturing methods. It is essential to develop advanced manufacturing processes that can control the microstructure, density, and chemical composition of a SSB. Sintering is a fundamental process in materials science and engineering that results in solid materials with desired properties. By applying heat to a powder compact, the particles bond together, reducing porosity, and eventually forming a dense, cohesive material [6,7]. Over time, advances in sintering techniques have reduced the temperature and duration required for producing dense ceramic structures. New techniques like spark plasma sintering (SPS), microwave sintering, laser sintering, ultra-fast high-temperature sintering, cold sintering (CS), and flash sintering (FS) have been developed in recent years. In the future, embracing these innovative approaches can lead to a cleaner and more sustainable economy, reduced energy consumption, and faster processing times which can result in improved battery performance. Scientists are continuously researching the fundamental mechanisms underlying these newfound sintering techniques in the field of SSBs. This exploration is likely to result in even more transformative innovations in the future, bringing forth exciting possibilities for energy storage and sustainable technologies [8,9].

The sintering of multilayered systems and constrained films have been extensively studied because they are important in wide range of applications such as electronic packages, multilayer capacitors, ceramic sensors and actuators, batteries, and solid oxide fuel cells [10]. A comprehensive theoretical analysis of densification and shape distortion of bi-layer and tri-layer systems can be obtained from the free densification behaviour of each layer. The study of poly-crystalline ceramics involves experimental and theoretical studies of various parameters, such as impurities, second-phase particles, and defects. Theoretical concepts of sintering were originally based on ideas of a discrete organisation of porous media [11]. However, macroscopic variables also have a role in determining the kinetics of sintering, in addition to the characteristics of the powder particles and the type of contact they have. The use of experimentally acquired parameters in macroscopic models or meso-scale simulation utilising physical models has been the main focus of sintering systems theories and simulations. Ensuring accurate particle packing and pore/grain microstructures requires

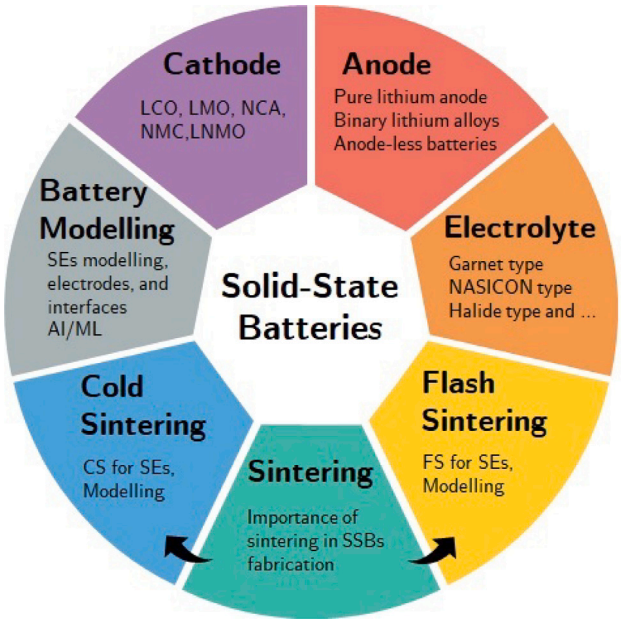


**Fig. 1.** Overview of our approach in the article.

robust meso-scale simulations in addition to a significant macroscopic investigation for technical reasons [12,13].

The shapes of grains and pores in the intermediate and final sintering stages could be described in a more detailed fashion based on idealised geometric simulations. Many numerical simulations have been conducted to investigate the sintering kinetics and microstructural evolution of nano-particles, including Molecular Dynamics (MD) [14,15], Continuum Mechanics [16], Surface Evolver Technique [17], Finite Element Method (FEM) [18,19], and Discrete Element Method (DEM) [20–22]. These simulations have shown good agreement with experimental data regarding the evolution of the contact area between particles and volume shrinkage. Among them, the FEM is widely used for the solution of problems of density distribution in real porous samples [13,23].

In this article, an extensive review of SSBs, and their potential as a groundbreaking energy storage technology is presented. An overview of our article is provided in Fig. 1. Initially, our discussion covers the core principles underlying SSBs technology, including the electrochemical processes that drive battery performance. We also explore the different parts of an SSB, such as the solid electrolyte (SE), the anode, and the cathode, detailing their roles and how they interact within the battery. Then, we examine the challenges associated with these advanced battery systems. Also, we shed light on two promising sintering techniques, namely CSP and FS. These techniques have shown immense promise in enhancing SSBs' performance and manufacturability. In addition, we discuss numerical simulations of these sintering methods in an attempt to unravel their complex processes. Our article aims to contribute to the understanding and realisation of efficient SSBs by gathering the latest research findings and technological advancements, opening new opportunities for future energy storage technologies.

## 2. SSBs

To make efficient, clean energy storage possible, lithium-ion batteries (LIBs) are the key technology with characteristics such as substantial reversibility, high energy density, and safety [24]. Generally, they consist of four components: the cathode, anode, electrolyte, and separator. Through the discharging process de-intercalated $Li^+$ from the anode moving via the electrolyte intercalates into the cathode, where electrons from the anode flow through an external circuit to the cathode and undergo a reduction-oxidation (redox) reaction — the charging process is the opposite. The separator prevents direct contact between the anode and cathode, while the electrolyte is used to transfer the $Li^+$ and block electrons. Each part of the battery has its distinctive purpose and works together so that the energy can be efficiently exchanged between chemical and electrical forms [25,26].

A conventional LIB typically consists of a liquid electrolyte to help transport Li ions from the cathode to the anode, and vice versa [27]. This may elevate the risk of electrolyte leakage if there are any defects or holes. Furthermore, the formation of dendrites of Li can make it prone to exploding. Additionally, the low ignition point and low boiling point make it vulnerable to dangerous conditions such as thermal runaway, and side reactions between the electrode and electrolyte, all of which can lead to electrolyte failure [26,28].

SSBs have gained significant attention because they offer potentially higher gravimetric and volumetric energy and power densities, a wider operating temperature range, and enhanced safety compared to conventional liquid electrolyte-based systems. The slower reactivity of solids compared to liquids suggests that SSBs may have longer lifespans, as demonstrated with micro batteries operating for more than 10,000 cycles [29]. The aging effects associated with liquid electrolytes in LIBs will not be present in SSBs; however, cathode material gas evolution can still cause safety and aging issues. The challenges that LIBs, are facing today must be understood in the context of the development of SSBs. In addition to the storage and active materials, existing LIBs also include a sizeable amount of cooling equipment and auxiliary materials [4].

### 2.1. Charge transfer mechanism in SSBs

Solid-state electrolytes (SEs) have a different charge transfer mechanism than liquid electrolyte-based batteries. Ion diffusion is what propels the charge transfer mechanism in SEs [30]. The charging process involves both lithiation in the anode by diffusion through the electrolyte and de-lithiation from the cathode. Similarly, the opposite reaction, which involves the ions' transit through the SEs, takes place during the discharging process. Accommodation of lithium in the host structure needs to be without restrictive forces, therefore it demands anode and cathode to be chosen correspondingly. The anode and cathode's Fermi potential difference determines the cell voltage and the number of Li ions that enter the electrodes increases the current delivered. Li-ion diffusion must occur through pores or vacancies in the

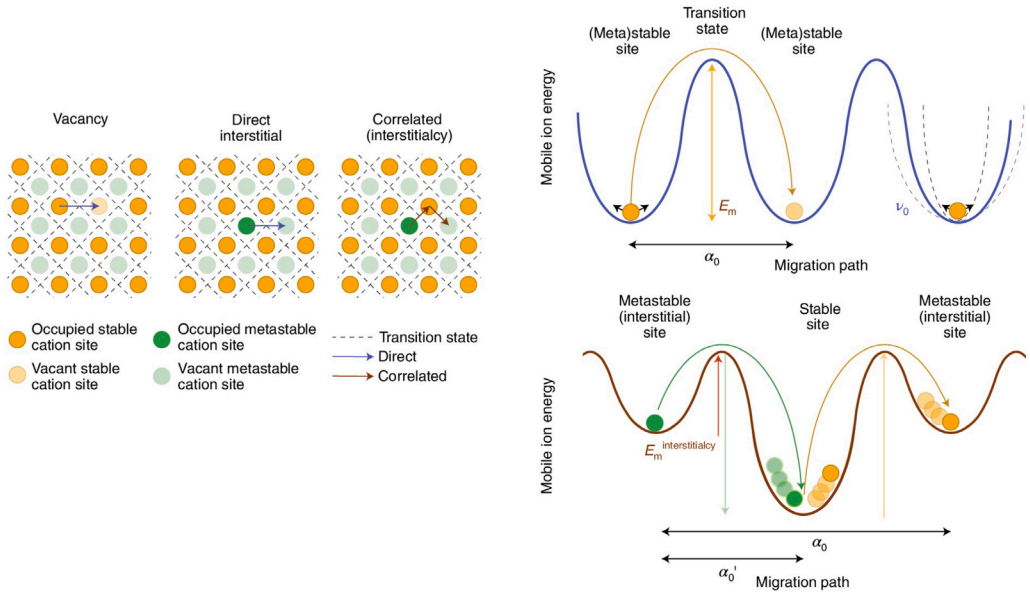


**Fig. 2.** Mechanisms of cation migration and related energy profiles — copied with permission from [29].

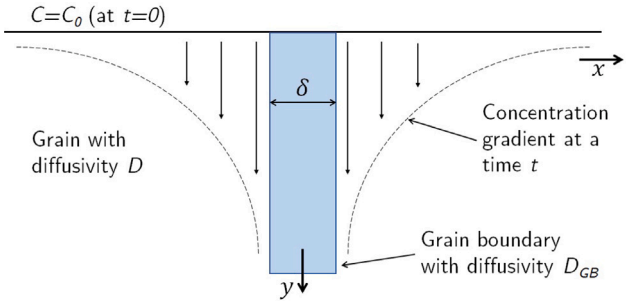


**Fig. 3.** Gradient in Li-ion concentration is formed at the grain boundary over time when the cell cycles between charging and discharging — redrawn with permission from [31].

host (electrode) lattice. Fig. 2 depicts a schematic illustration of the Li-ion diffusion mechanism across the grain boundary. This illustrates that the formation of a concentration gradient at the grain boundary aids in the process of grain boundary diffusion. However, compared to other methods of diffusion, this technique of lithiation demands extremely higher activation energy. The diffusion process for Li ions over the grain barrier is schematically represented in Fig. 3, which shows that the creation of a concentration gradient at the grain boundary facilitates the diffusion process [31,32].

### 2.2. All-SSB materials

#### 2.2.1. Cathode

The cathode plays a crucial role in SSBs, as it serves as the source of ions during the charging process and facilitates their transfer in the opposite direction during discharging. The cathode must remain structurally stable throughout these processes. Furthermore, ensuring a high level of ionic conductivity in the cathode is essential [33]. Researchers are studying the same active materials used in commercial LIBs. Prominent candidates include layered oxides such as lithium cobalt oxide (LCO), nickel cobalt aluminum oxide (NCA), and nickel manganese cobalt oxide (NMC), spinels like lithium manganese oxide (LMO) and lithium nickel manganese oxide (LNMO), and polyanionic olivines such as lithium iron phosphate (LFP) [34]. Cathode materials are classified through their structure. The $LiMO_2$ formula and its prototype is $\alpha$-$NaFeO_2$ structures which belong to the $R\bar{3}m$ space group (Fig. 4a) is mostly considered (M is a 3d transition metal, e.g. Ni, Co, Mn, Mg, Fe, Al). An octahedral occupancy of oxygens surrounds Li and M, which are arranged in alternate stacking layers within this structure. Spinel structured cathode materials, $LiM_2O_4$, Li, and M are occupied in tetrahedral and octahedral environments of O respectively, with the space group of $Fd\bar{3}m$ (Fig. 4b). In spinel structures, there are octahedra of $TMO_6$ within the TM layer, which together with Li tetrahedra form a three-dimensional network. Various polyanionic materials have also demonstrated promise as cathodes, including silicate, olivine phosphate, and tevorite. Fig. 4c shows the orthorhombic structure of olivine phosphate, or $LiMPO_4$, which consists of $MO_6$ octahedra, $PO_4$ tetrahedra, and $LiO_6$ octahedra that share edges. Tavorite-$LiMSO_4F$ and silicate-$Li_2MSiO_4$ (Fig. 4d and e) have also been suggested as cathode materials [35].

$LiNiO_2$, $LiMnO_2$, and $LiCoO_2$ are the three fundamental layered oxides that have been thoroughly investigated [36]. Selecting the ideal cathode material involves finding the right balance between costs, stability, safety, energy density, and power density. For instance, LFP stands out as a cost-effective, safe, and stable option, but it has relatively low energy density. On the other hand, NCA exhibits superior performance in terms of energy and power density, although safety concerns arise due to its tendency for thermal runaways, particularly in small devices. Depending on the targeted application, cell and battery manufacturers prioritise specific aspects while managing trade-offs with other factors [34]. Cathode materials typically have lower specific capacities, but the general efficiency of a SSB is still constrained by their performance. Introducing nano-particles to common cathodes, such as $LiCoO_2$, can enhance their properties. However, using these materials at high temperatures raises more safety concerns compared to when they are utilised on a smaller amount. This issue can be

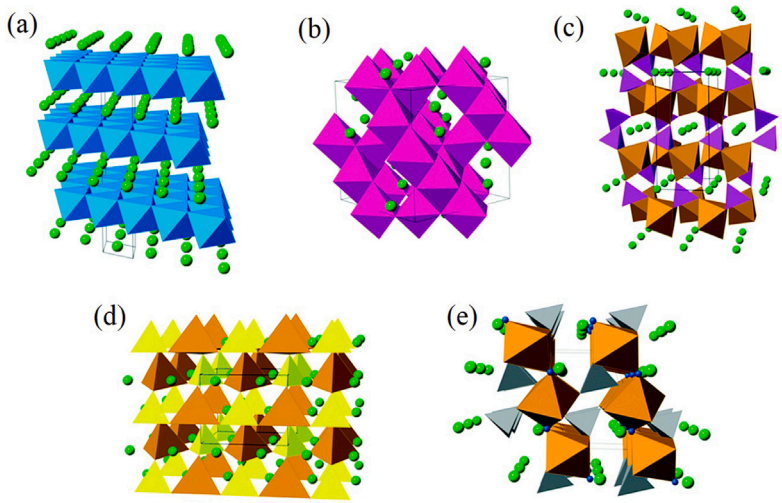


**Fig. 4.** Cathode materials for lithium-ion batteries have representative crystal structures: (a) layered $\alpha$-$LiCoO_2$, (b) cubic $LiMn_2O_4$ spinel, (c) olivine, (d) silicate, (e) tavorite — copied with permission from [35].

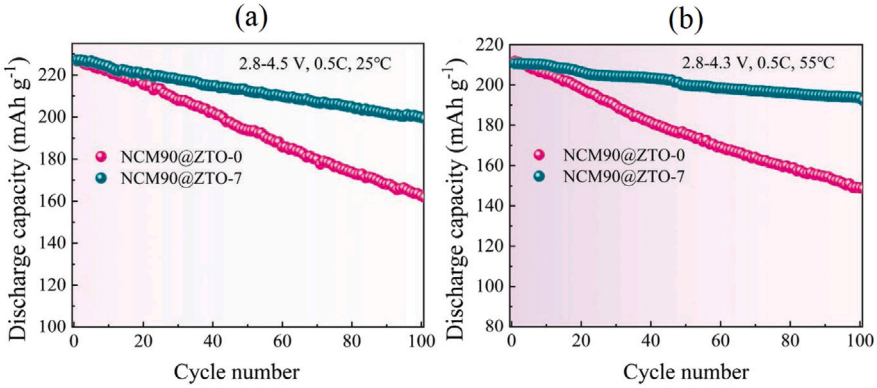


**Fig. 5.** Cycling performance was done at two different temperatures: (a) at 25 °C in the range of 2.8–4.5 V, and (b) for NCM90@ZTO-0 and NCM90@ZTO-7, at 55 °C in the range of 2.8–4.3 V The NCM90@ZTO-0 cathode displays a capacity retention of 70.5%. Conversely, the NCM90@ZTO-7 still shows a capacity retention of 90.1% after 100 cycles under the same test conditions. The enhanced performance probably derives from the epitaxial ZTO cladding, which maintains the lattice oxygen/transition metal structure by preventing the surface corrosion — copied with permission from [38].

mitigated by coating the nanoparticles with a stabilising layer that lowers the cathode's rate of lithiation/delithiation (it is important to note that cathode lithiation occurs during discharge). Due to their improved specific capacity and thermal stability, $LiNi_xMnyCo_{1-x-y}O_2$ (NMC) layered oxides have drawn more attention. The benefits of all three transition metals are incorporated in NMC-based cathode materials; nickel can give high specific capacities, while Co and Mn can offer superior kinetics in layered structures and enhanced structural stability [37,38]. Tan et al. [38] have developed a new method to improve the mechanical stability of ultrahigh-Ni (NMC90) by using $ZrTiO_4$ (ZTO) as an epitaxial layer. As a result of the ZTO modification (c.f. Fig. 5), the NMC90 exhibits a significant increase in cyclability under high voltage (4.5 V), as well as a 17% increase in capacity retention (71% vs. 88%) after 100 cycles.

### 2.2.2. Anode

Potentially good anode materials are typically those that have a large capacity for storing $Li/Li^+$. This is so because, during the charging process, lithiation occurs at the anode. With a suitable layer structure (layer spacing of 0.335 nm), graphite, one of the stable carbon allotropes, enables reversible $Li^+$ intercalation/deintercalation [39]. Graphite has been the preferred anode material for commercial LIBs due to its relatively low cost, superior capacity (372 mAh $g^{-1}$), high cycling stability, and low operating temperatures. However, graphite encounters low lithiation voltage (0.08 V vs. $Li/Li^+$) and slow lithium intercalation kinetics [40]. Spinel lithium titanium oxide ($Li_4Ti_5O_{12}$, LTO) is a promising alternative to graphite anodes in lithium-ion batteries due to its high lithium insertion/extraction voltage of approximately 1.55 V (vs. $Li/Li^+$) and excellent cycle stability. However, despite these advantages, LTO's low electronic and ionic conductivities necessitate further engineering to improve the power performance of batteries [41]. Ultimately, Li metal is the best option as an anode in SSBs. Li et al. [30] have investigated lithium anodes in solid-state cells using chitosan-based SSE, which led to a stable discharge capacity of 160 mAh $g^{-1}$ for up to 50 operational cycles. Also, pure lithium metal anodes have some limitations. Due to lithium metal's extremely high sensitivity to elevated temperature conditions, one significant issue with lithium anodes is that they cannot be used in high-temperature operational conditions.

Moreover, the instability of lithium anodes in SSBs poses a significant challenge to maintaining desirable charging and discharging rates and extending the battery's lifespan. The chemical and mechanical degradation of alloy anodes at higher current rates or through repeated alloying and dealloying processes can become a critical issue, for instance, in the case of the Mg-70 wt% Li system, there is a tendency for the redox plateau to weaken with repeated cycling [42]. Various strategies have been investigated to address this issue. One approach involves applying high stack pressures to prevent the formation of pores during the stripping process. However, it is important to keep the applied stack pressure as low as possible in practice because high pressures

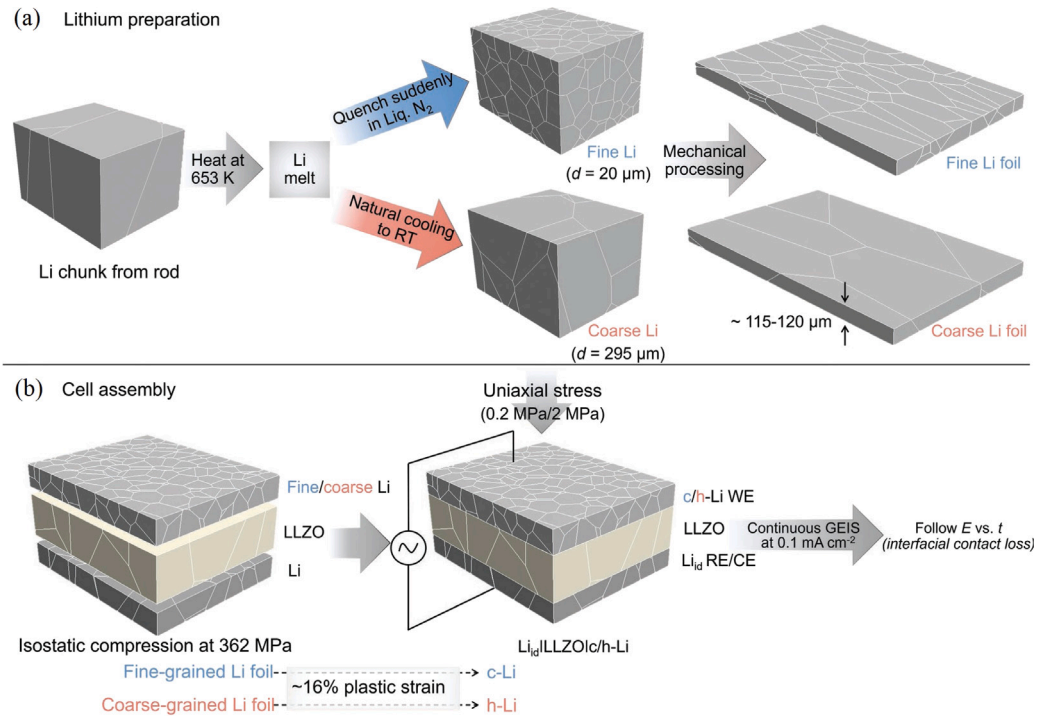


**Fig. 6.** (a) Creating samples of polycrystalline lithium metal with fine and coarse grains, (b) studying creep deformation behaviour of assembled cells — copied with permission from [42].

can lead to extensive interfacial fractures, which reduce the critical current density [42,43]. Singh et al. [42] have proposed an innovative approach to combat lithium anode degradation by controlling the microstructure (outlined in Fig. 6). They utilise the creep behaviour of polycrystalline lithium to address the interfacial instability associated with pore formation during anodic stripping. This is accomplished by employing fine-grained polycrystalline lithium (with a grain size of 20 micrometers) as anodes and taking advantage of shorter diffusion pathways with high diffusivity channels.

Another method is to use binary lithium alloys to mitigate the issue of pore formation. However, these alloys face constraints related to both electrochemical and mechanical issues, and the shift in redox potential with changing composition limits the theoretical and practical specific capacity of these alloys [44,45].

Fuchs et al. [46] look at how current density affects the morphology of lithium growth shown in Fig. 7. The lithium plating with various current densities was characterised using the in-situ SEM plating process. The micrographs demonstrate how the current density increases together with the heterogeneity of the lithium-particle size, shape, and density deposited at the Cu|LLZO interface. Cu|LLZO and Cu|LIPON interfaces were subjected to image analysis to compare the nucleation quantitatively. According to their investigation, the dispersion of $A_{\text{Li-Particle}}$ similarly reduces with increasing current densities, and the area of each lithium particle decreases with bigger $n_{\text{Li-Particle}}$. It was feasible to measure the lithium particle density as a function of the applied current density and by examining thin copper sheets (d = 100 nm). Fig. 8 illustrates a significant increase in lithium particle density and area coverage at increasing current densities.

Researchers have been investigating different electrode designs, specifically focusing on the anode side, to enhance the energy density of all-SSBs (ASSBs). The anode-less concept, which eliminates the need for an active material on the anode side, shows potential in achieving energy density close to the theoretical maximum while also reducing material costs and simplifying the manufacturing process [47]. However, operating anode-less cells at room temperature and low pressure poses challenges, such as sluggish lithium plating and stripping kinetics and the formation of interfacial voids. To address these issues,

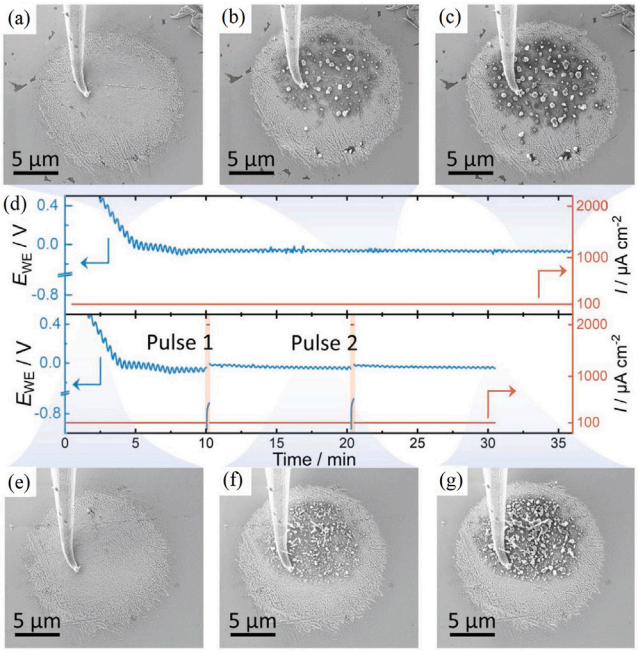


**Fig. 7.** (a–c) SEM micrographs taken at various times while plating lithium using 100 µA cm$^{-2}$. On top of (d), the relevant voltage and current profiles are shown. The voltage and current profiles during plating with 100 µA cm$^{-2}$ and interrupting current pulses of 2000 µA cm are displayed in the lower section of (d) — copied with permission from [46].

Oh et al. [48] introduces a dual thin film comprising a magnesium (Mg) upper layer and a $Ti_3C_2T_x$ MXene buffer layer. The Mg layer enables reversible Li plating and stripping at room temperature through a low-energy (de)alloying reaction, while the MXene layer preserves the electrolyte-electrode interface, even under low pressure conditions (2 MPa), thanks to its high ductility. The integration of these layers

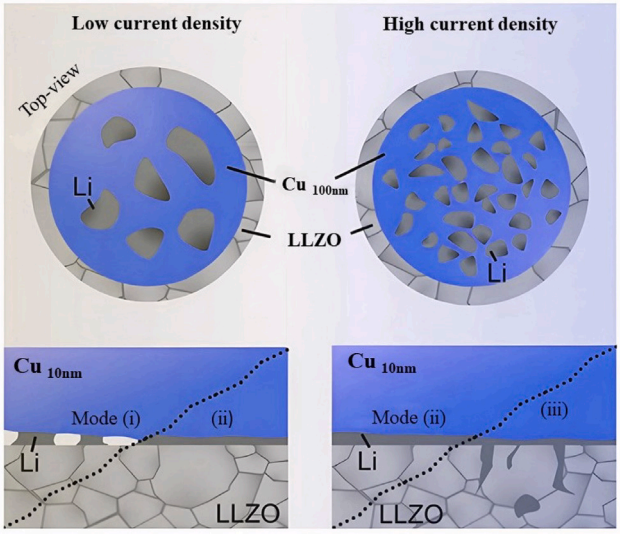


**Fig. 8.** Diagram illustrating the occurrence of several lithium growth modes when applying varying current density to thick current collector foils (bottom) or thin current collector films (top) — redrawn with permission from [46].

allows anode-less ASSBs to operate simultaneously at room temperature and low pressure, opening new possibilities for practical and efficient anode-less battery systems.

### 2.2.3. Electrolyte

One of the most crucial components of LIBs is the electrolyte. Fig. 9 provides a general comparison of various electrolytes used in LIBs, including liquid, hybrid, and SEs, and aims to introduce the different types of electrolytes and illustrate how each one performs in key areas. It highlights their distinct properties such as ionic conductivity, leakage tendencies, and energy density [49,50]. The primary characteristic of SEs is their rapid and effective ion transport. Recent research has also demonstrated that crystalline electrolytes are often required for SEs to have a high ionic conduction rate [51]. Despite certain drawbacks such as instability upon contact with metallic Li, and relatively lower Li-ionic conductivity compared to most liquid electrolytes, ceramic SEs exhibit slightly better performance in terms of ionic conductivity when compared to polymer-based electrolytes — due to their predominantly ionic bonding. Additionally, ceramic SE-based batteries are well-suited for applications requiring higher temperatures, as they offer greater structural stability — and the ionic conductivity typically increases with rising temperature [52].

In general, oxide electrolytes exhibit strong chemical stability, good ionic conductivity, and broad electrochemical windows. They have therefore attracted a lot of interest over the past few decades. Because of its stability against Li metal, garnet-type SEs (e.g., $Li_7La_3Zr_2O_{12}$, LLZO) are among the most widely used oxide-type electrolytes. Furthermore, owing to their high conductivity and accessibility of initial components, SEs of the NASICON type (e.g., $Li_{1.3}Al_{0.3}Ti_{1.7}(PO_4)_3$, LATP) have been extensively studied. Due to the high-temperature processing requirements of oxide electrolytes, their integration with other electrode materials poses challenges due to potential side reactions during co-sintering. To address this issue, the development of soft-electrolytes containing sulfide species has gained significant attention and has been widely studied in previous studies due to the high conductivity and feasibility of the synthesis method. The ceramic SE consisting of oxides, oxy-nitrides, nitrides, phosphates, and sulfides could represent the more significant class of SEs, enabling even greater safety for LIBs [31]. Lately, halide SEs have become a promising option due to their ability to combine the advantages of sulfides and oxides. They exhibit good mechanical sinterability and (electro)chemical stability [53]. One issue of achieving densification of oxide electrolytes is that high-temperature sintering at approximately 1000 °C is typically required. To address this challenge, ternary oxide glasses in the $Li_3BO_3$–$Li_2SO_4$–$Li_2CO_3$ system were prepared through mechanical milling. These glasses were then converted into glass-ceramics by heating to induce crystallisation. To further enhance the conductivity of the glass-ceramic electrolyte, the glass was hot-pressed near its glass transition temperature of 210 °C under a pressure of 360 MPa for 12 h, followed by heat treatment at 260 °C for 2 h. The resulting hot-pressed pellet exhibited an impressive relative density of 98%. At room temperature, the glass-ceramic electrolyte demonstrated a conductivity of $1.0 \times 10^{-5}$ S cm$^{-1}$ and was kinetically stable against a lithium metal negative electrode [54].

It is essential to use ceramic electrolytes with noticeable room-temperature ionic conductivity and functional Li-ion transportation in required ambient temperatures. It must be noted that the synthesis and sintering method chosen, as well as the microstructure and interface quality characterisation, have an impact on the Li-ion conductivity of the ceramic electrolytes. Greater significance exists in the relative difference of absolute values of the ionic conductivity of the SEs obtained after SPS as compared to processing after conventional routes. The processing and microstructure of ceramic SEs significantly influence their performance [55]. Therefore, the utilisation of techniques like SPS becomes crucial to control microstructural length scales and engineer interfaces at the atomic level, enhancing the overall performance of the SE materials [55,56]. Important major parameters which are mentioned in the following, must be considered in the selection of the electrolytes.

**Ionic conductivity**

For a SSE to effectively perform its function of facilitating ion flow while preventing electron conduction, the ion transference number should be close to unity [57]. This implies that a majority of the required ionic species can freely move through the electrolyte and this is due to the electrolyte's primary function of facilitating ion (cation) flow and obstructing electron movement. The ion transference number, however, is usually only about 0.5 in reality, meaning that only half of the ions are transferred across the electrolyte [58]. Therefore, the selection of an electrolyte with an ion transference number as close to unity as possible is crucial to enable efficient cation transport, reduce concentration polarisation, and ultimately achieve higher power density. To achieve high Li+ transference composite electrolytes, two major approaches can be used: one is to give $Li^+$ a continuous channel, and the other is to immobilise anions through interactions with other components. [59]. As a result of the concentration gradients being eliminated throughout the cell, particularly at the dendritic front, a unity transference number ($t_+ = 1$) may inhibit dendritic development,

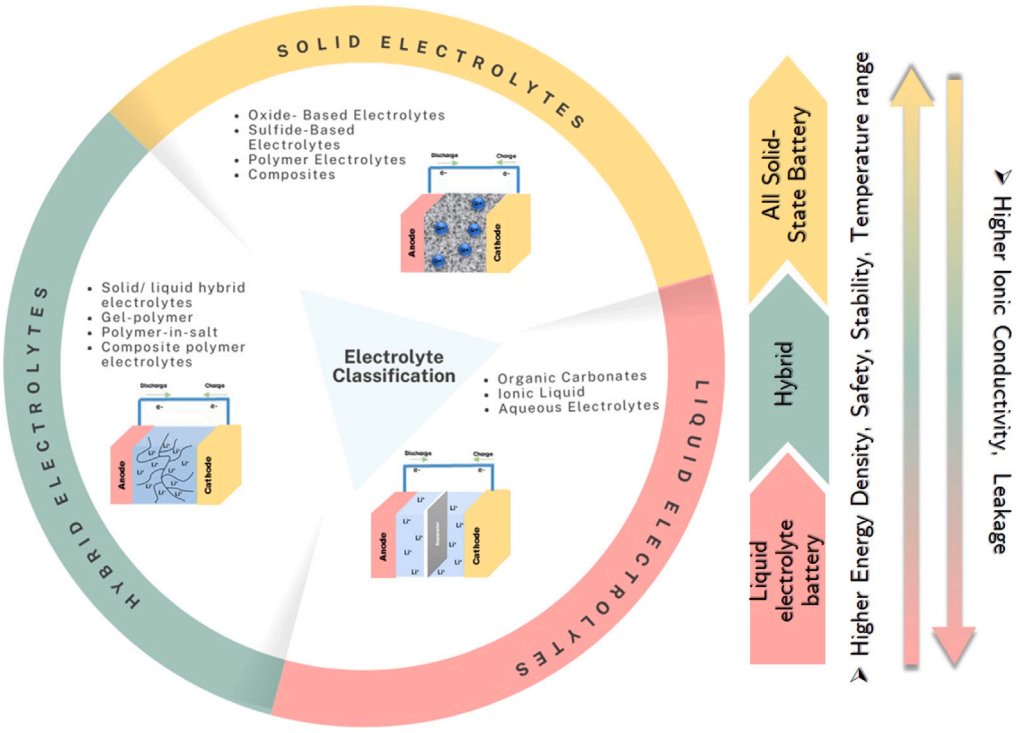


**Fig. 9.** Comparison of different electrolytes in LIBs, including liquid, hybrid, and solid types.

according to simulation results by Monroe and Newman. Additionally, a unity transfer number can lead to high energy density and peak power density [57,60]. Improving the ionic conductivity can be achieved by carefully selecting materials with inherent conductivity, introducing dopants, controlling grain size, and optimising processing techniques [61,62]. For example, Li et al. investigated the structural landscape of existing and potential superionic halide SEs. They demonstrated that, in many cases, a significant increase in ionic conductivity could be achieved by transitioning the base structure from hexagonal close-packed (hcp) to cubic close-packed (ccp) [63].

**Chemical and thermal stability**

The electrolytes need to perform precisely in an electrochemical range of 0 V to roughly 4.5 V. Therefore, a SSE must possess chemical and electrochemical stability. An electrolyte's stability window is the voltage range that it can withstand without undergoing redox degradation. As shown schematically in Fig. 10, the electrode voltage (vs. $Li^+/Li$) is linked to the Li chemical potential ($\mu_{Li}$), which can change significantly in the interfacial region. Similar to the double layer at solid/liquid interfaces, a space-charged layer forms at low potential. Due to the $\mu_{Li}^+$ difference between metallic lithium and SSEs, the anode pushes mobile cations into the electrolyte. Meanwhile, these cations move towards the cathode, creating space-charged regions at high potentials. This rearrangement leads to concentration gradients, causing the SSEs to react with the electrodes, forming a lithium-rich interphase at the anode and a lithium-poor interphase at the cathode [29]. The broad operational temperature range is a another critical requirement for the versatility of SSBs and lithium-based rechargeable batteries often range between 50 °C and 80 °C. Therefore, the electrolyte needs to exhibit excellent performance within this specific temperature range and remain thermally stable without experiencing any degradation [64].

To increase chemical stability, an LLZO scaffold has been suggested lately. This design seems to be effective in addressing two issues: the creation of voids and the dynamic volume variations of the Li anode. Compared to conventional LIBs, cells with cathodes containing LPS or LLZO SEs achieve much higher volumetric energy densities. The obtainable gravimetric and volumetric energy densities sharply decrease with increasing volumetric concentration of SEs in the cathode. To get high power densities, however, a high LLZO concentration in the cathode is required. It has been suggested that to reduce the production of Li dendrites caused by the reduced real current density during Li plaiting, self-standing porous LLZO membranes might be utilised in place of dense LLZO membranes (Fig. 11a–b). This way, it is possible to greatly decrease the initial Li plating current density [65]. However, one issue is that LLZO and Li transition metal oxides are incompatible during co-sintering and it is challenging to introduce cathode particles into LLZO porous scaffold [66].

Inorganic SEs, such as sulfides and halides, are sensitive to humid air and requires stringent dry-room conditions during processing, leading to increased production costs [67]. To address this issue, surface treatments have been proposed to enhance the air stability of sulfide SEs. Kim et al. [68] demonstrated that ultra-thin superhydrophobic coatings (around 5 nm) of polydimethylsiloxane (PDMS) or fluorinated PDMS (F-PDMS) can significantly improve the stability of air-sensitive sulfide ($Li_6PS_5Cl$) and halide ($Li_{2.5}Zr_{0.5}In_{0.5}Cl_6$) SEs in ASSBs. These coatings are applied using a scalable vapour-phase deposition process. Impressively, the $Li^+$ conductivity retention after coating was remarkably high, with 92% retention for $Li_6PS_5Cl$ attributed to the thin coating layer. In another study, fluorine substitution in $Li_2ZrCl_6$ improves solid-state Li metal battery performance by forming a LiF-containing interphase. While it also decreases ionic conductivity, it exhibits superior cycling performance compared to the F-free $Li_2ZrCl_6$ [69]. Similarly, fluorinated $Li_3YBr_{5.7}F_{0.3}$, which exhibits a structure similar to $Li_3YBr_6$, has been developed, demonstrating high ionic conductivity of $1.8 \times 10^{-3}$ S $cm^{-1}$. This novel electrolyte can function directly with a lithium metal anode and shows significantly enhanced stability due to the densely formed, in situ, fluoride-containing interface layer [70].

### 2.3. Electrolyte interfaces

It is significant to highlight that battery function is not always driven out by electrochemical processes at the SE/electrode interface.

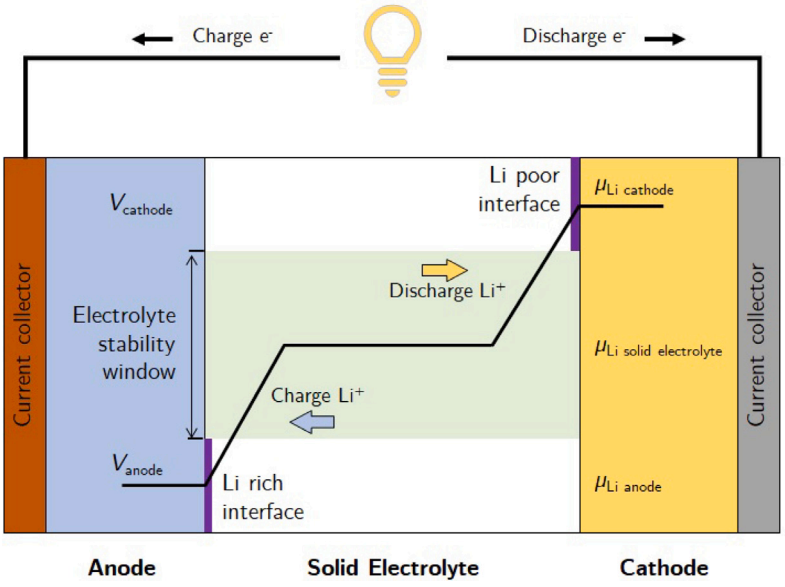


**Fig. 10.** Chemical potential evolution in contact with an anode and cathode across a SE.

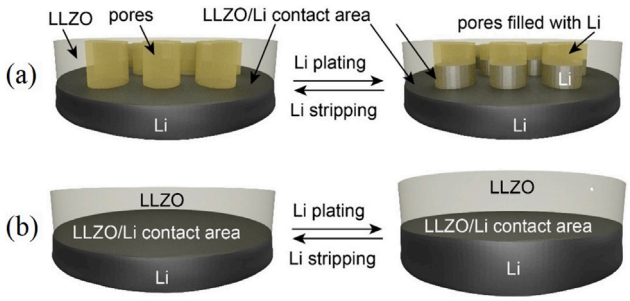


**Fig. 11.** Illustration of Li plating/stripping Li-LLZO interface for (a) porous and (b) dense LLZO — copied with permission from [65].

The reactivity of the interface is an important factor therefore, the interfacial transport qualities control the kinetics and subsequently the magnitude of the reaction. In SSBs, interphase layers are formed at the interface of electrode/electrolyte and both chemical and electrochemical processes act simultaneously to cause interphase appearance [71]. Based on their electrical and ionic conducting characteristics, interfaces between SEs and anode (e.g. metallic lithium) can essentially be classified into three categories — c.f. Fig. 12. (1) Li metal that is not reacted with thermodynamically stable surfaces; (2) mixed conducting interphases (MCI), which can carry ions and electrons concurrently and cause ongoing interfacial deterioration; (3) ionic conductive and electron insulator interphases, which hinder the electrolyte reaction with electrode surface and also allow Li-ion conduction [26,72]. Additionally, three different types of functional interfaces that are capable of being utilised to operate for SSBs have been depicted in Fig. 13. Those are intrinsically stable, kinetically stabilised, and artificially protected. For instance, when there is no reaction involving the two materials, the situation is known as intrinsic stability [29].

As described before, the ideal interphase exhibits good ionic conductivity and an excellent electron transfer impeding. This will provide an interphase that is durable against electrochemical decomposition. Mixed-conducting interphase, which is adequately conducting for both metal ions and electrons, can trigger extensive reactions that result in a metallic anode's thickness continuously increasing, an insurmountable resistance, and a short circuit [26]. Metal elements in SEs have an extensive desire to reduce reaction which will lead to the formation of such interphases at low voltage, for example, Ge in NASICONs and $Li_{10}GeP_2S_{12}$ or Ti in NASICONs and perovskites [73]. At the interface between the electrolyte and electrode, side reactions may take place, lowering area-specific resistances. Furthermore, Li-ion redistribution zones may result from variations in Li-ion chemical potential between electrolytes and active materials, which may impede Li-ion transport across electrolyte/electrode interfaces. Fig. 14 summarises the interface issues at the electrolyte's contact with both the cathode and anode [74].

The interface between the SE and cathode in SSBs can suffer from instability and degradation at elevated temperatures required for sintering processes [51]. Researchers aimed to identify the key factors contributing to this degradation by studying the co-sintering of $Li_7La_3Zr_2O_{12}$ (LLZO) SE and a layered transition metal oxide cathode. Co-sintering the materials at high temperatures is often an attempt to maximise the contact between the SE and cathode and reduce the interfacial impedance [75,76]. Also, the effects of different gas species during annealing, including $O_2$, $N_2$, $CO_2$, and humidified $O_2$, ranging from 300 to 700 °C were systematically examined. Sintering in pure $O_2$ resulted in excellent chemical stability and low interfacial resistance, comparable to LLZO interfaces with protective coatings. Sintering in $N_2$ prevented the formation of secondary phases but caused oxygen loss at higher temperatures. In humidified $O_2$, hydration and dehydration of the cathode material occurred. Notably, sintering in $CO_2$ led to the formation of insulating secondary phases that hindered charge transfer. To achieve successful co-sintering without interfacial degradation, it is crucial to minimise $CO_2$ and $H_2O$ during sintering processes [77].

The stability and compatibility of compounds in SSBs with electrodes have been extensively studied, often resulting in bi- or multilayer designs [78,79]. A study analysed the structural stability and chemical

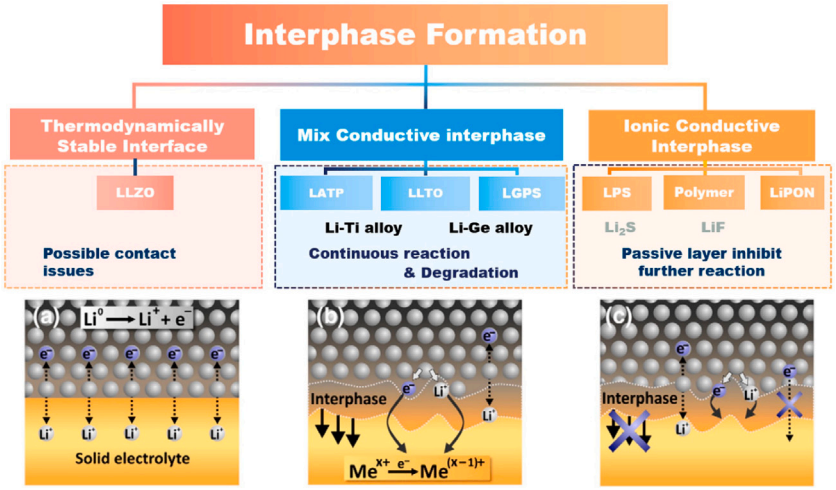


**Fig. 12.** Three different forms of interphases between metallic lithium and SSE — copied with permission from [26].

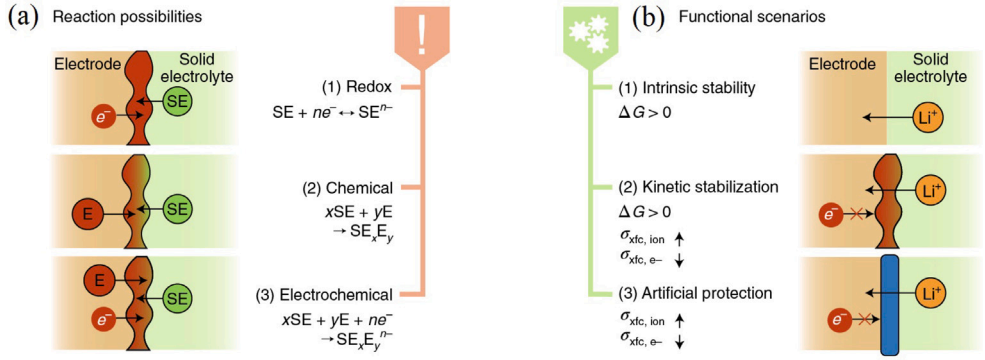


**Fig. 13.** SE/electrode interface (a) reaction potentials and (b) functional situations in SSBs — copied with permission from [29].

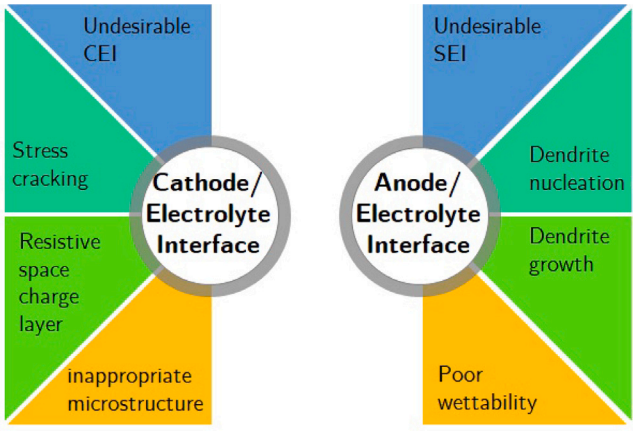


**Fig. 14.** A summary of electrolyte/electrode interface problems in ASSLBs.

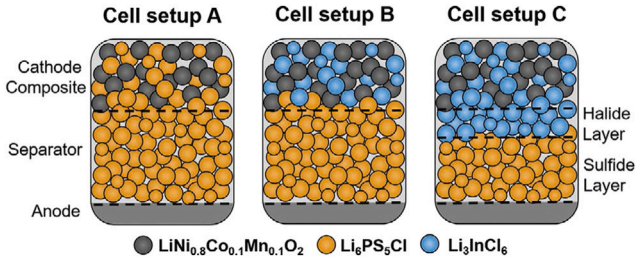


**Fig. 15.** Different configurations of cells are utilised, employing various combinations of separators and cathode composites, with NMC811 as the cathode active material (represented by the colour black) — copied with permission from [80].

compatibility of a composite mixture of NCM523 and LLZO-Ga. The phase transition of the cathode and SE materials varied depending on the quantity of lithium in the layered cathode and the presence of oxygen gas during co-sintering. It was demonstrated that the oxygen-free $N_2$ atmosphere caused the transition metals in NCM523 to be reduced to the metallic state, causing LLZO-Ga to undergo a cubic to tetragonal phase change [78]. Moreover, the reactivity beyond electrodes has been overlooked, leading to capacity fading and poor cycling stability. To address this, Rosenbach et al. [80] investigated the impact of a bilayer separator in halide electrolyte $Li_3InCl_6$ in combination with the typical cathode active materials (CAM) $LiNi_{0.8}Co_{0.1}Mn_{0.1}O_2$ and the separator material $Li_6PS_5Cl$. Their objective was to gain a better understanding of the impact of the additional layer by exploring various setups of SSBs — see Fig. 15. Their findings revealed that the additional halide separator layer is crucial for improved cycling stability, enhancing capacity retention and suppressing impedance evolution. The formation of an interphase, observed through degradation products, occurs primarily at the triple phase boundary with contact to the cathode active material. Overall, a bilayer separator is necessary for long-term stability in $Li_3InCl_6$-based composite cathodes combined with sulfide electrolyte-based separators like $Li_6PS_5Cl$ [80].

The number and quality of Li-ion and electron transfer channels may also be ascertained by looking at the spatial distributions of

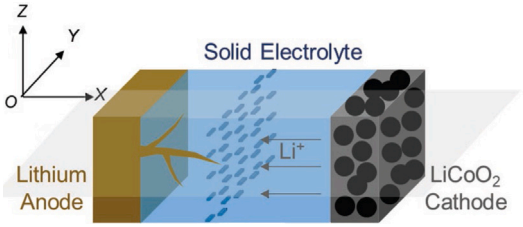


**Fig. 16.** The schematic of the 3D structure of the battery, showcasing how HBs are introduced as a part of the design strategy — copied with permission from [83].

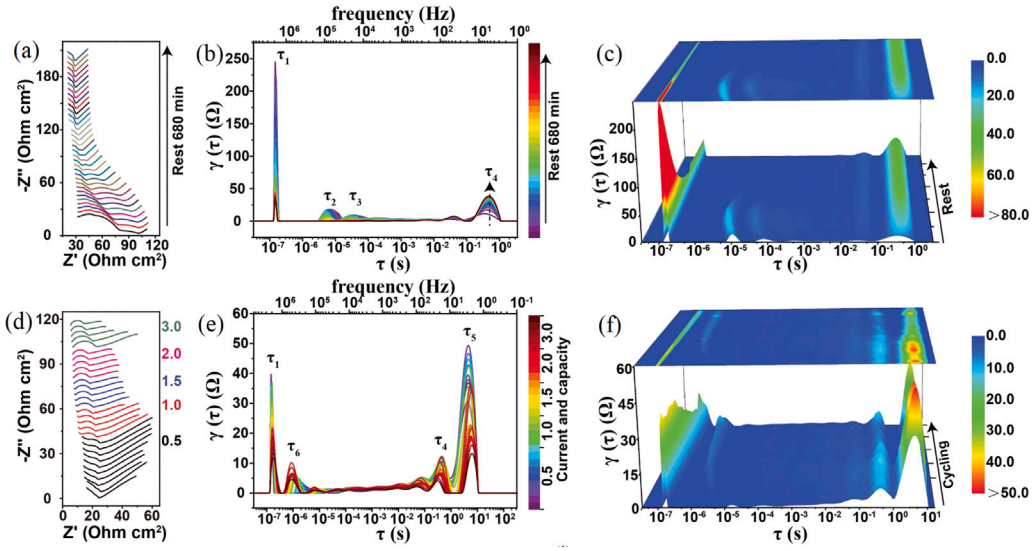


**Fig. 17.** The evolution of electrochemical impedance spectroscopy (EIS) and its corresponding distribution of relaxation times (DRT) transformation were studied in Li/SL/LPSC/SL/Li batteries during the initial rest process (a–c) and cycling at different current densities (d–f) — copied with permission from [84].

electrolytes, active materials, and electron conductors. Direct mixing is a popular method for creating electrode and electrolyte microstructures, but without perfect control over relative factors, the results are frequently random distributions that cannot guarantee effective contact [74]. Additional research has revealed that the quantity and size of electron conductors, active materials, and electrolytes are critical for establishing a successful contact. Wider electrochemical stability windows are possible for oxide electrolytes, and co-sintering leads to improved side reaction kinetics, which mostly causes Cathode-electrolyte interface (CEI) production at LLZO/cathode contacts [81]. Also, ion implantation has the potential to induce the migration and clustering of defects, which can subsequently lead to surface contact degradation and elevated interfacial impedance. Yao et al. [82], use ion implantation to apply compressive stress to the ceramic SSE pellets' surface and study the connection between the electrochemical performance and mechanical parameters. A series of successive ion energy implantations were utilised to attain a uniform and extensive layer of Xe ion implantation at various depths. The notably diminished crystalline structure in LLZTO indicates structural damage, likely accompanied by the formation of numerous defects. These defects are responsible for contact deterioration and the subsequent increase in local current density. Certain SEs may have internal compression that significantly reduces their ionic conductivities, and they may be able to stop dendrite penetration if their shear modulus is more than twice that of lithium metal.

### 2.4. Lithium dendrite growth

Lithium dendrite formation in the interface is another significant phenomenon, especially occurring in SSBs under high current density, and is driven by localised overpotential due to electrolyte/Li interface inhomogeneity. Two things, however, can prevent the formation of Li dendrites, and the electrolyte's critical overpotential can be determined by these two resistive forces. Defects are the source of electrolyte inhomogeneity; following charging, holes, and cracks close to the interface between the electrolyte and Li anode easily fill with Li dendrites without obstructing the flow of current. Grain boundary softening takes place at the nanoscale region close to grain boundaries; while charging, Li accumulates along the softer grain boundary regions as a result. Elemental segregation can also cause intergranular dendrite growth [74]. Compared to Ga-doped LLZO, Li dendrites in Al-doped LLZO mostly developed through grain boundaries, indicating inferior suppression capacities [85]. Ning et al. [86], investigated crack propagation in interface due to dendrite formation. They claimed the effect of critical current density for dendrite crack initiation is determined by the local fracture strength of the SE, and the pore pressure exceeds the local fracture strength at a sufficiently high current density, inducing fracture.

Researchers suggest embedding heterogeneous blocks (HBs) within the SE to mitigate and suppress dendrite growth-induced internal short circuits (ISCs). Fig. 16 illustrates the approach of incorporating HBs into SSBs. By employing a phase-field-based multiphysics model, the research team investigated the behaviour of dendrite growth and identified the characteristic length ratio between the HBs and SE as a crucial factor governing dendrite growth paths [83]. Their findings indicate that a single long HB or multiple HBs with specific layouts can effectively block dendrites and prevent short circuits, while shorter HBs can delay the occurrence of ISCs to some extent. Furthermore, the multilayer SE structure, particularly when comprised of thicker and multiple embedded layers with lower Young's modulus, shows promise in mitigating dendrite growth and delaying short circuits [83]. However, further consideration of actual microstructural effects is necessary for the implementation of these findings.

The development of 3D Li metal anodes has shown promise in addressing dendrite-related issues in liquid batteries. However, implementing this approach in SSBs has presented challenges due to the limited interfacial contact with rigid inorganic SEs. In a recent study, Duan et al. [84] successfully constructed a 3D Li anode for SSBs through spontaneous chemical reactions between halide SEs and Li metal. This in situ formation of Li–Al alloys and well-maintained sulfide electrolytes inside the 3D structure created continuous pathways for electron and Li ion transport, facilitating uniform charge carrier distribution. The lithiophilic Li alloy regulated Li deposition behaviour, enabling homogeneous Li nucleation and deposition. As a result, both symmetric Li|Li batteries and full SSB exhibited favourable electrochemical performance even at high current densities. The proposed strategy by Duan et al. [84] offers a reverse train of thought to construct 3D Li anodes for SSBs, enhancing stability and capacity in Li-based battery systems. To analyse the reaction process and interfacial evolution during rest time, in situ EIS experiments were conducted and studied using the distribution of relaxation times (DRT) method (Fig. 17). Results showed the emergence and completion of the reaction between Li metal and $LiAlCl_4$ (LAC), along with distinct relaxation times representing different electrochemical processes. The stabilisation of certain relaxation times indicated the successful formation of a 3D Li metal anode, while fading relaxation times demonstrated ongoing reactions between Li metal and a sacrificial layer. Monitoring the symmetric battery during cycling revealed new processes related to Li metal plating/stripping and SEI formation.

The dynamics of contact evolution and electrochemical–mechanical interactions during plating and stripping at the Li-SE interface have been analysed. Incomplete contact between solid–solid interfaces influences the homogeneity of electrochemical reactions, which in turn impacts the anode's Li metal plating and stripping as well as the cathode's active material particle separation [87]. Solid–solid point contacts or isolated Li islands have been identified as a limitation that occurs with increasing stripping rates [88]. Applying pressure can prevent formation of voids at a Li metal anode during stripping because high pressures trigger Li to effectively creep and adapt to the coarse electrode/electrolyte interface [89]. Contact loss can also occur during plating, especially at faster deposition rates, but the criteria that govern void growth behaviour in stripping and plating are different which is shown in Fig. 18-(a). In the case of stripping, if the reaction current and creep deformation exceeds the mechanical deformation of the Li surface at a given contact point where the gap height is initially zero, contact will be lost and a gap will form. This occurs when the local reaction current outweighs the mechanical effect, resulting in a loss of contact [88]. Li et al. [90] directly observed lithium filament growth in LLZTO using Neutron Depth Profiling. The large volume changes and mechanical stress caused by lithium plating accelerate crack propagation in LLZTO. However, they discovered that a well-designed 3D framework for the negative electrode can accommodate the significant volume expansion during lithium plating and control lithium deposition, preventing lithium filament growth. The occurrence of contact loss during plating is critically governed by the difference in local deposition heights along the interface and the counteracting effect of $Li^+$ creep to replenish the underlying gaps. Non-uniformities in external pressure and temperature have a significant impact on the contact distribution, leading to disparate scenarios of void localisation. Contact loss is a key limitation towards achieving practical areal capacities and faster plating rates in SSBs [88]. Future research could explore the role of interphases between the SE and Li in influencing non-homogeneity in ionic transport and reaction kinetics.

### 2.5. Battery modelling

Modelling SSBs involves the construction of mathematical and computational representations of the electrochemical processes, and it involves complex interactions between multiple physical phenomena, including electrochemistry, heat transfer, and mechanical stress [91,92]. Through battery modelling, various design configurations and material choices can be virtually tested, significantly reducing cost-prohibitive trial-and-error experiments. For example, Vadhva et al. [93] utilised modelling to investigate the stress–strain behaviour of electrodes of varying thickness. Cell expansion was shown to be a trade-off when limiting maximum stress. Rajimakers et al. [94] extend the idea of design optimisation. Their model incorporates the kinetics of charge transfer between two electrode/electrolyte interfaces, diffusion, and migration of lithium ions in the electrolyte and positive electrodes. Further, to validate the simulations, 0.7 mAh Li/LiPON/$LiCoO_2$ thin film, SSBs were experimentally tested. Modelling of battery degradation and failure modes is becoming increasingly popular. Sultanova et al. [95] proposed a model to provide new insight into the effects of viscoplasticity and interfacial damage on the in situ diffusive-mechanical behaviour of a polymer-based cathode for a SSB. In addition, Bucci et al. [96] used Electro-chemo-mechanical FEM simulations to capture the onset and propagation of damage in a solid-state composite electrode.

Understanding the formation of the SEI is crucial for improving battery performance, lifespan, and safety. Researchers utilise ab initio or quantum chemistry methods, with Density Functional Theory (DFT) to elucidate how the SEI evolves during battery cycling. Also, quantum chemistry calculations are used to identify which molecules are most susceptible to reduction, shedding light on SEI composition [97,98]. Understanding the interactions between molecules and ions with electrode surfaces is essential for comprehending the process of electrolyte decomposition. These interactions can influence concentration gradients, alter reaction pathways, and introduce catalytic effects [99]. Moreover, continuum models are widely adopted due to their computational efficiency, but they rely on the assumption of homogeneity in cell behaviour, SEI formation, and the reactions occurring at SEI/electrolyte interfaces [97].

In a study by Miara et al. [100], the stability of LLZO and LLTO ($Li_5La_3Ta_2O_{12}$) against different cathode materials was investigated. It was determined that the interphase decomposed more easily at high sintering temperatures than during electrochemical decomposition. Ab initio molecular dynamics (AIMD) simulations offer a direct means to study electron and ion transfer at electrode interfaces. AIMD simulations help explore the energetics of decomposition reactions at electrode interfaces, providing insights into both fast and slow reactions [97]. AIMD simulations by Cheng et al. [101] for a Li–$Li_6PS_5Cl$ interface also highlighted the poor stability of sulfide electrolytes concerning Li-metal. There was a severe break in the P–S bond, followed by the formation of Li–P and Li–S bonds. Moreover, they use higher temperatures to accelerate possible reactions on a timescale that is practical for AIMD. Fig. 18(b) shows the corresponding interface structures. Even at 298 K, significant interface decomposition is observed after 500 ps.

The applications of battery modelling are expanding to address various challenges and innovations in the field. The integration of machine learning (ML) techniques with battery modelling has revolutionised the search for high-ionic-conductivity SEs, offering a systematic and efficient approach to materials discovery. The synergy between innovative materials and advanced algorithms paves the way for a brighter, more sustainable future in energy storage technologies. Also, the realm of battery interface simulations has witnessed a transformative shift with the integration of ML models. These models play a crucial role in predicting properties derived from time-dependent simulations, thus offering a more efficient way to unravel the mysteries of battery interfaces [102–104].

ML models fall into three main categories: Gaussian process-based learning, neural network potentials, and graph neural networks. Among these, graph neural networks have emerged as a recent development ideally suited for modelling the SEI, which is renowned for its complexity. ML potentials for electrode materials can provide accurate results even within the vicinity of equilibrium structures, focusing on

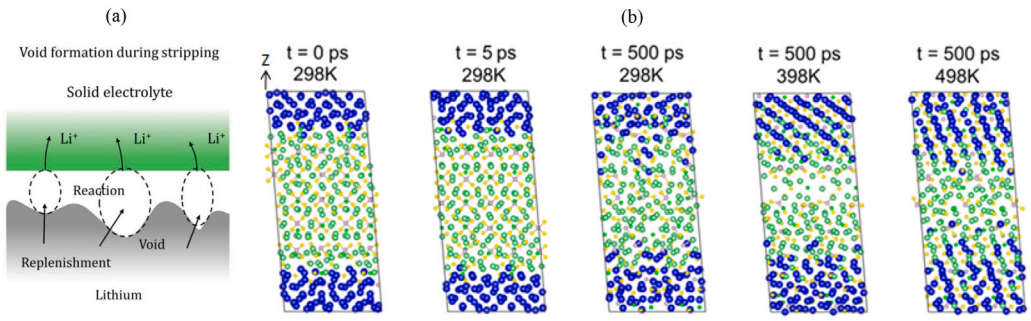


**Fig. 18.** (a) Different mechanisms that compete with each other play a role in determining the contact loss response during stripping — copied with permission from [88]. (b) Li-electrode/$Li_6PS_5Cl$-electrolyte interface degradation at NVT AIMD. Li electrodes (blue) — copied with permission from [101]. (For interpretation of the references to colour in this figure legend, the reader is referred to the web version of this article.)

short-range interactions. The SEI's intricate reaction network poses challenges for obtaining reliable energetics with high-accuracy DFT simulations. To tackle this complexity, systematic generation of relevant species is employed to map large reaction networks accurately. Here, ML models come into play, aiding in exploring the vast landscape of SEI reactions [97].

Support vector machines (SVMs) have been employed to predict ionic conductivity by classifying various samples into different labels. Fujimura et al. [105] used support vector regression (SVR) with a Gaussian kernel to predict the low-temperature conductivities of various compounds. Cubuk et al. [106] leveraged transfer learning by utilising 30 elemental descriptors from 40 materials to train a linear SVM via leave-one-out cross-validation. Using these methods, they screened $20 \times 109$ materials for the first time and proposed a handful of promising candidates for Li-ion conductors in SEs. They combined the output of this structure model with another research to train a generic descriptors model, enhancing prediction accuracy. Regression models, such as kernel ridge regression and gradient boosting regression, have been instrumental in the quest for SEs like LiOH, $LiAuI_4$, $LiBH_4$, $Li_2WS_4$, and $Ba_{38}Na_{58}Li_{26}N$. These models help identify potential candidates for high ionic conductivity [107].

One study used ML to predict the mechanical properties of potential solid-state electrolytes (SEs) for lithium batteries. Their predictions were accurate, as confirmed by first-principles calculations. They developed a predictive model for SEs with bulk modulus less than 100 GPa and shear modulus less than 70 GPa. Using this model, they analysed 2842 SSE candidates and found that oxide structures had good mechanical properties, while NASICON- and garnet-like structures had the worst (Fig. 19). They also used ML to identify influential factors for SEs, such as volume, density, and crystal structure. This demonstrates the potential of ML to improve the accuracy of SSE predictions [103]. Also, Solid-state lithium polymer batteries' RUL can be predicted using ML models enhanced by genetic optimisation employing symbolic regression. The model structure is shown in Fig. 20. The model can predict RUL values close to actual values in training battery data. It outperforms SVR, Gaussian process regression (GPR), and elastic net (EN) methods, demonstrating its utility in RUL prediction [108].

ML technology hinges on the selection of an appropriate dataset and its transformation into a format that algorithms can effectively handle. The quality of the input data representation significantly influences an algorithm's ability to accurately map it to the desired output data. Deliberate data pre-processing is crucial for mitigating simulation errors. This includes feature extraction, which transforms raw data into essential characteristics, providing a unique subset that can be continuous or discrete [102,103,108]. Despite the promise of ML algorithms, concerted efforts by materials scientists and algorithmic scientists are required to address challenges, including lack of training data, model complexity, and the necessity to obtain a quantitative relationship between material parameters and performance [102]. Fig. 21 provides a visual summary of how various ML models are integrated into battery modelling to address specific challenges and enhance the discovery and prediction processes.

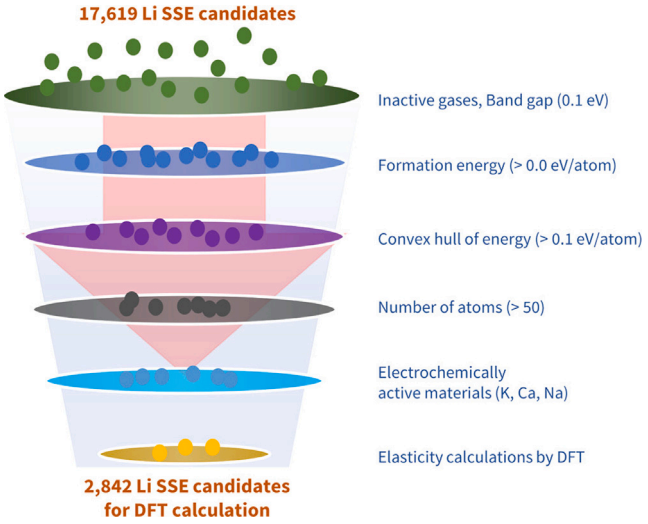


**Fig. 19.** Selecting Li SSE candidates (17,619 to 2842) using a screening procedure whose mechanical characteristics are computed using DFT calculations — copied with permission from [103].

## 3. Importance of sintering in SSB fabrication

Sintering methods in SSB fabrication are predominant. SE particles need to be bonded together by sintering before being used in batteries. The influence of sintering conditions on the properties of SSBs has been explored. The development of SSBs has been significantly hindered by serious side reactions that can happen between the electrode and the SSE. Lithium ion transport will be decreased and the interface resistance will rise if an ion-blocking interface forms [109,110].

### 3.1. Theory of sintering

Sintering is a process of volume and shape deformation of a porous body caused by substance flow of the porous body skeleton which causes densification and grain growth. Sintering is influenced by several factors, including temperature, time, pressure (if applied), and material properties. Moreover, the atmosphere can influence the structure of grain boundaries, which in turn can influence grain growth [111]. Sintering force is dependent on pore volume fraction and dihedral angle between grain surfaces as a function of porosity. The sintering stress increases with density for a fixed grain size but decreases with increasing grain size. The underlying theory of sintering can be explained using two main mechanisms: diffusion and surface tension [12]. Sintering deals with a particle collection's diffusion process at the microscopic level. Condensation, surface diffusion, grain boundary diffusion, volume diffusion, plastic deformation, or creep are the stages that it goes

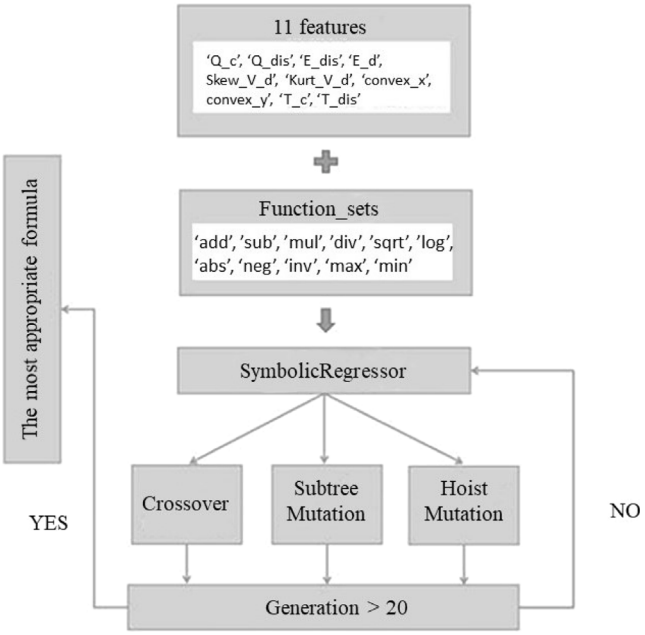


**Fig. 20.** Structure of symbolic regression model — redrawn with permission from [108].

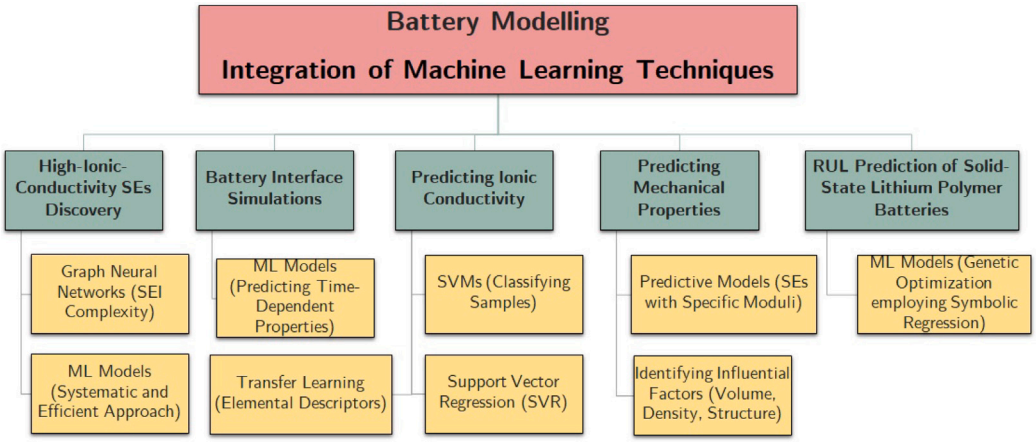


**Fig. 21.** A summary of the integration of ML techniques in battery modelling.

through as it evaporates. Sintering happens when the particle/pore contact is eliminated, lowering the surface energy [111,112].

### 3.1.1. Diffusion

At elevated temperatures, atoms in the solid state possess sufficient thermal energy to diffuse across the boundaries of neighbouring particles. The process of diffusion is governed by Fick's first law, which relates the diffusion flux vector (**J**) to the concentration gradient ($\nabla c$) and the diffusion coefficient ($D$):

$$\mathbf{J} = -D\nabla c \tag{1}$$

Here, $\nabla c$ represents the concentration gradient with respect to $x$, $y$, $z$, and across which diffusion occurs [113,114]. During sintering, atoms move from regions of higher concentration to regions of lower concentration, leading to the migration and accumulation of atoms at the particle interfaces. This diffusion of atoms at the interfaces promotes neck formation between adjacent particles, gradually consolidating the powder compact. As sintering continues, grain size and grain boundary substantially increase, and the grain boundary diffusion distance increases, the densification rate slows, and grain boundary mobility becomes significant for grain growth to proceed [111].

### 3.1.2. Surface tension

Surface tension is another crucial aspect of sintering, particularly in the later stages of the process when the necks between particles become well-developed. Surface tension arises due to the tendency of a liquid or solid surface to minimise its area, leading to the rounding of sharp corners and edges. Ceramic nanoparticles have a high specific surface area, which is accompanied by high surface energy [115]. Agglomeration causes loss of contacts and reduction in coordination numbers, which can mature into a critical defect if prevented from healing. Agglomeration leads to non-uniform densification of nano-powders, which can generate processing defects. However, in the context of sintering, surface tension drives the reduction of surface area by promoting the coalescence of adjacent particles and smoothing out irregularities in the compact's surface [111].

Understanding the kinetics of the sintering process is essential for optimising sintering conditions to achieve desired material properties. The sintering kinetics are influenced by the rate of diffusion and the rate of neck growth between particles. Several models have been proposed to describe the sintering kinetics, including the Herring–Nabarro model and the densification function model [23,115].

Conventional sintering has been the backbone of materials processing for decades, including the fabrication of SSBs. Pressure-less

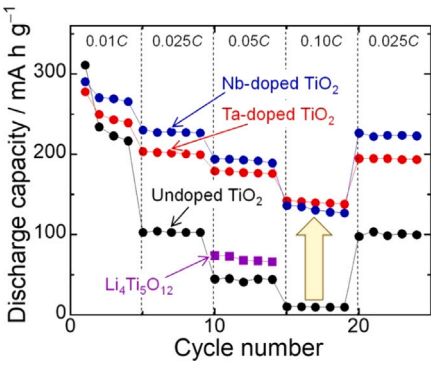


**Fig. 22.** Rate capabilities of $TiO_2$ electrodes cycled at 90 °C with different dopants (Nb, Ta) compared to a SSB with a $Li_4Ti_5O_{12}$ (LTO) anode and $Li_7La_3Zr_2O_{12}$ (LLZO) electrolyte cycled at 95 °C. — copied with permission from [119].

sintering has the desirable characteristics of simple equipment setup, the ability to sinter complex shapes, and low cost, but the densification rate is slow. Despite its widespread use, conventional sintering has some drawbacks, notably, high energy consumption, long processing times, and the risk of grain growth, which may lead to reduced battery performance. High-temperature sintering can limit the choice of materials, especially when dealing with temperature-sensitive components like SEs. Thus, exploring alternative sintering techniques has become imperative to overcome these limitations [7,111].

In recent years, CSP has gained significant attention due to its innovative, low-temperature sintering process. Compared to conventional sintering, CSP allows densification of materials at much lower temperatures, typically below half of their melting point. This novel approach combines the application of heat and pressure with the use of a chemical additive, often a liquid, to facilitate diffusion and promote densification. The key advantages of CSP include energy savings, shorter processing times, and the ability to process temperature-sensitive materials [116–118].

The driving force behind CSP is the reduction in activation energy for densification, which can be understood through the following modified Arrhenius equation:

$$D = D_0 e^{\frac{-E_a}{RT}} \tag{2}$$

where $D$ is the diffusion coefficient, $D_0$ is a pre-exponential factor, $E_a$ is the activation energy for diffusion, $R$ is the universal gas constant, and $T$ is the absolute temperature. By utilising chemical additives, CSP effectively lowers the activation energy, allowing for densification at lower temperatures.

FS, also known as field-assisted sintering, is another emerging technique that has shown remarkable potential in rapidly densifying materials. This innovative method uses an electric field to accelerate sintering, allowing for lower temperatures and faster processing times. It has been successfully applied to a wide range of materials, including ceramics for batteries. The exact mechanisms behind FS are still being researched. However, it is believed that the migration of charged defects and the application of electric field-assisted Joule heating can accelerate the diffusion processes [120–122]. The current density ($J$) and electric field ($E$) influence the sintering rate, and a critical threshold must be exceeded to initiate the FS phenomenon.

$$J = \sigma E \tag{3}$$

In this equation, $\sigma$ is the electrical conductivity of the material. When the electric field reaches a critical value, it triggers a sudden enhancement of diffusion and densification, significantly reducing the sintering time [123,124].

### 3.2. Parameters affecting the sintering process

#### 3.2.1. Temperature

Sintering is usually employed to achieve densification and consolidation of ceramic electrolytes from initial powders. However, in the case of oxide electrolytes, the high-temperature processing required poses challenges to their compatibility with other electrode materials, like undesired side reactions during co-sintering. Also, high-temperature co-sintering causes serious lithium loss in cathode active material [125]. Moreover, The sintering process can create a highly resistive interface between the SE and the active material, significantly reducing electrode performance. To address this, Usui et al. [119] developed SSBs using $TiO_2$ anodes and a $Li_3BO_3$–$Li_2SO_4$–$Li_2CO_3$ SE via room-temperature pressing, eliminating the need for sintering. These batteries operated at 90 °C and exhibited good reversible capacity. Additionally, doping $TiO_2$ with Nb or Ta significantly improved rate capability. As illustrated in Fig. 22, this battery's performance surpassed that of a $Li_4Ti_5O_{12}$ anode with a sintered garnet electrolyte, despite the non-sintered electrolyte used. Their work highlights the potential for efficient SSBs using non-sintered electrolytes.

In the study by Yan et al. [126], the effects of sintering temperature (950, 1000, 1050, 1100 °C) on the mechanical properties and ionic conductivity of LATP electrolyte was investigated. Overall, it is anticipated that the SE LATP would have adequate mechanical qualities to withstand deformation, cracking, and dendritic development in addition to high conductivity. The findings showed that while the quantity of secondary phase, density, and conductivity increased with higher sintering temperatures, the grain sizes of the four samples were equal.

The ion conductivity of solid oxide or phosphate-based electrolytes can be improved by using higher temperatures during the sintering process. Nevertheless, because of the high temperatures needed, the powder technology sintering method used for these electrolytes is energy-intensive. Elevation of the temperature might cause undesirable interactions with the electrode materials, including phase formation or element evaporation [72]. Reducing the sintering temperatures of such materials is therefore important. Using sintering aids is one method to lower the sintering temperatures. One well-known example is liquid phase sintering, in which densification is improved by creating a brief liquid phase during the sintering process. Another approach is the widely employed technique known as field assisted sintering technology (FAST) [125] or SPS [52]. These methods involve the direct application of electrical current to heat the material or the surrounding die, resulting in high heating rates, typically ranging from 50 to 200 °C $min^{-1}$ [55].

Recent studies have demonstrated that the presence of small quantities of water, even in the absence of an actual liquid phase, can enhance densification and significantly lead to lower sintering temperatures. In addition to the development of hydrothermal hot-pressing techniques, a novel method known as CSP was introduced first where the $CaCO_3$ was successfully densified at room temperature using carbon dioxide gas and mechanical pressure [125–127]. The procedure and the methodology of CSP are presented in Fig. 23. The method relies on densifying wet powders at low temperatures (less than 300 °C) using water or a

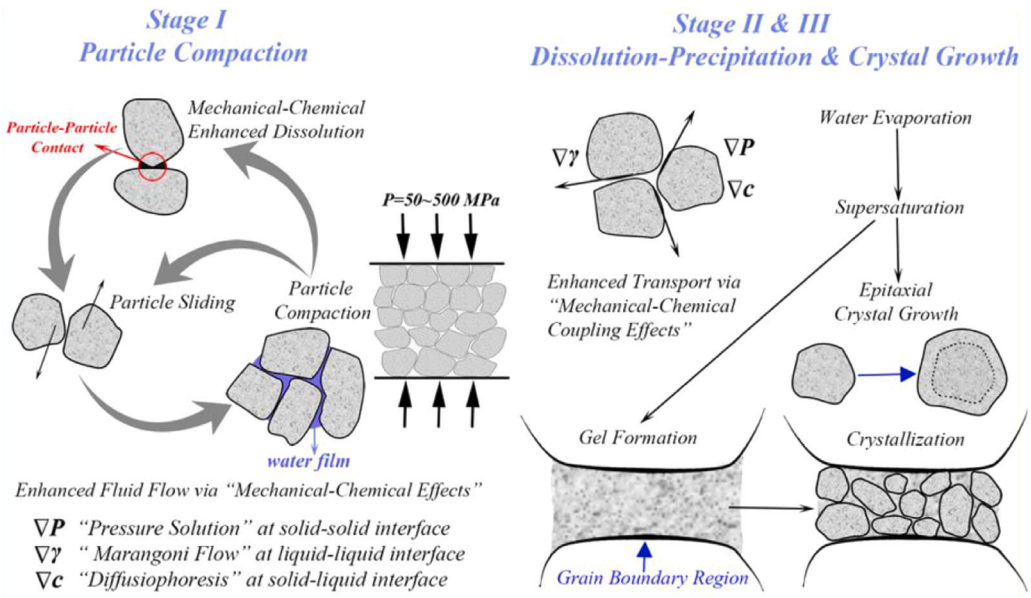


**Fig. 23.** The three steps of the CSP process; its principles and methodology — copied with permission from [127].

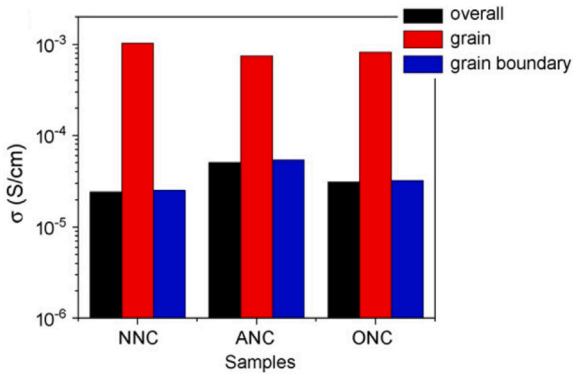


**Fig. 24.** Ionic conductivities of these LLTO ceramics sintered in various atmospheres, $N_2$ atmosphere (NNC), air (ANC), and $O_2$ (ONC) — copied with permission from [128].

precursor solution while applying high uniaxial pressures (up to 600 MPa). However, further heat treatment is required to complete the crystallisation process and achieve the requisite amount of densification for some materials, such as zirconia and barium titanate, for which the CSP process alone is insufficient to produce full densification [58].

### 3.2.2. Atmosphere

The lattice structure and ionic conductivity for lithium lanthanum titanate $Li_{0.5}La_{0.5}TiO_3$ (LLTO) and Li-Garnet (c-$Li_7La_3Zr_2O_{12}$, c-LLZO) SE sintered in different atmospheres were investigated. Geng et al. [128] have studied LLTO sintered in oxygen and nitrogen atmospheres compared with air. While $Li_{3x}La_{2/3-x}TiO_3$ has a superior lithium ionic conduction behaviour due to the existence of a correct ratio of lithium-ion to vacancy, the true lithium composition of LLTO would fall to a proper level due to lithium evaporation during the sintering at the high temperature. It is noteworthy that the grain boundary conductivity of LLTO sintered in nitrogen, oxygen, and air atmospheres increases progressively in each of these atmospheres (Fig. 24). The grain boundary conductivity of the LLTO samples sintered in a nitrogen environment is the lowest because of the prevalence of oxygen vacancies, which speed up lithium loss in the nitrogen atmosphere to maintain a charge balance of cations and anions. The LLTO samples sintered in a nitrogen environment have reduced grain boundary conductivity because fewer mobile lithium ions are participating in the transport mechanism at grain borders.

Li-garnet powder is used as a SSE in LIBs in the majority of published works to compensate for Li-loss [129,130]. Furthermore, the Li-loss issue has not yet been thoroughly investigated to determine the nature of the volatile lithium compounds (VLC) and how they affect the c-LLZO sintering [131]. Huang et al. [132] studied $Li_2O$(g) atmosphere impact on garnet grain evolution and proved that the garnet grains which were thoroughly sintered in a low VLC with long-term sintering resulted in no trans-granular fracture. Fig. 25A–D depict two example triple-point grain boundaries of the Ta-LLZO ceramics sintered under high and low levels of VLC atmosphere for three hours at 1250 °C. Samples made within these conditions have a relative density of 95% and a Li-ion conductivity of $4.3 \times 10^{-4}$ S $cm^{-1}$. With extended sintering in a high VLC, unusual grain growth takes place. The relative densities rise to 98% and $6.4 \times 10^{-4}$ S $cm^{-1}$, respectively.

### 3.2.3. Pressure

Achieving a high storage capacity in SSLIBs necessitates a dense sintered component structure. To enhance the densification of SEs through sintering, pressure is one of the most affecting parameters and various approaches have been explored. One method is to add sintering additives to the electrolyte systems, such as LiF or $Al_2O_3$. Some sintering additives, however, have the potential to generate grain boundary phases with low $Li^+$ conductivity. Several additional pressure-assisted sintering techniques, such as hot pressing (HP) [133], SPS, and chemical co-precipitation method [32], were employed to

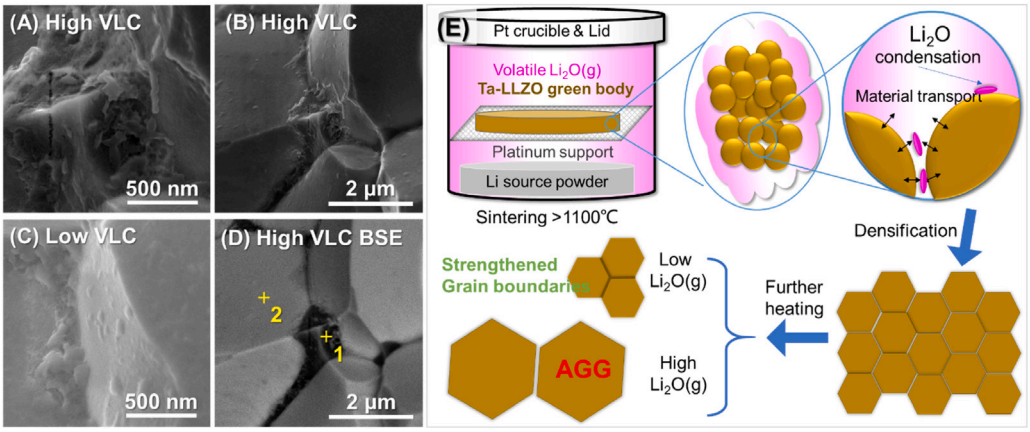


**Fig. 25.** Typical triple-point grain boundaries of Ta-LLZO samples sintered for three hours at 1250 °C in the high (A&B) and low (C) VLC atmospheres are shown in these field emission scanning electron microscopy (FESEM) pictures. The back-scattering electron (BSE) picture of (B) is represented by (D), where points 1 and 2 are chosen for energy-dispersive spectroscopy (EDS) element analysis. (E): schematic of sintering behaviour and probable mechanism of Ta-LLZO samples — copied with permission from [132].

sinter electrolytes with higher density. In this context, the oscillatory pressure sintering (OPS) technique has emerged as a novel sintering method [134]. In this method, periodic fluctuating pressure is applied during the sintering process, which noticeably improves the densification process. Li-garnet SEs (LLZO) were successfully prepared using OPS. SEs sintered by OPS exhibit better mechanical characteristics (241 MPa of bending strength) and excellent $Li^+$ ion conductivity compared to the sample sintered by traditional HP because of their greater density and finer grain structure [134].

An outstanding characteristic of the advanced high-pressure process is its ability to achieve a relative density exceeding 90% even at lower sintering temperatures, without any sintering aids [135,136]. Ihrig et al. [137] reported the application of high-pressure FAST/SPS for the fabrication of LLZO:Ta. A mechanical pressure of 50 MPa and 440 MPa was applied As expected, XRD patterns have shown higher crystallinity in higher pressure and the relative density slightly increases for a higher sintering temperature of 750 °C to 92% and 95% for the pure LLZO:Ta.

### 3.2.4. Time

Generally, the sintering process, including sintering temperature, powder content, sintering time, and other factors, has a significant impact on the Li concentration [138]. It makes sense that a shorter sintering time would result in lower density. A comparative study has been done by sintering the $Na_3Zr_2Si_2PO_{12}$ (NZSP) SSE of sodium-ion batteries, buried in its pristine powder for 20 h. Such long-time sintering increased the relative density value of the NZSP to 92%. Wang et al. [138], worked on different methods of synthesis of the sphene-type $Li_{1.125}Ta_{0.875}Zr_{0.125}SiO_5$ SE. The SE pellets have been prepared by a single-step (SS) cold press sintering, multi-step (MS) cold press, and SPS process with a variety of sintering times and heating rates. The bulk resistances of the electrolyte pellets were employed to calculate the related ionic conductivities of various electrolytes, and Fig. 26 also shows the correlation between the ionic conductivity and sintering time. A comparison between three different sintering methods shows the highest ionic conductivity and density in the SPS method despite the short time of sintering. Although the SS electrolyte requires close to 45 h to sinter, the pellet has the highest bulk resistance, which is possibly assigned to the large voids in its porous structure.

Using various current densities, Sazvar et al. [139] successfully flash-sintered the cubic garnet $Li_{6.25}Al_{0.25}La_3Zr_2O_{12}$ (Al-LLZO) at 850 °C in only 30 s. Increasing the current density had a substantial impact on the relative density, and control of the flash electric current was shown to be a crucial factor in densifying Al-LLZO. The LLZO sample sintered at 50 V $cm^{-1}$ and 200 mA $mm^{-2}$ showed a high relative density of 94%. In the FS technique, ceramic densification occurs in three stages as seen in Fig. 27. During incubation, the electric field remains constant as conductivity and energy density increase with temperature. In the sintering stage, conductivity spikes, leading to rapid increases in current and energy density, followed by stabilisation and slight grain growth. The electric field and energy density peak before gradually decreasing. In the stable stage, densification slows and stops, but grain growth continues until the electric field is removed [140].

### 3.3. CS

The cold sintering process (CSP) is a innovative technique that enables the densification of ceramics at low temperatures. This method consolidates powders by leveraging the combined effects of mechanical pressure and a solvent medium, typically water. By utilising an aqueous solution and applying uniaxial pressing pressure of 100–500 MPa at temperatures below 300 °C, researchers have developed a ceramic processing technology that offers exciting possibilities. In order to produce a supersaturated solution, CSP entails the dissolving of particle surfaces, particle rearrangement, and the evaporation of temporary solvent. There are two possible directions for this multistage non-equilibrium process: either crystal development or the creation of kinetically constrained glass/intermediate phases [117,118,141]. The relative density-sintering temperature curve for $BaTiO_3$ ceramics with respect to several sintering processes is summarised in Fig. 28 to present a comparison between different sintering methods [142].

With its unique combination of mechanical–chemical coupling effects and the creation of a proper solution system, CSP achieves improved mass transport aids in the densification process and demonstrates its potential at both macro- and micro-levels. The process can be divided into two stages: Stage I, where solid particles partially dissolve, Ostwald ripening occurs, and the sample starts drying, and Stage II, where solid particles make contact and form a rigid skeleton [141,143]. In Stage I, the system can be seen as non-contacting particles suspended in a liquid, with the pressure assumed to be isostatic due to the presence of the liquid “matrix”. The pressure-assisted solubility of a particulate compound decreases with increasing processing temperature, and the enthalpy of mixing influences the solubility. Ostwald ripening is the primary active process during Stage I, and the application of external pressure increases the solubility, leading to an accelerated rate of coarsening [143].

In Stage II, particle rearrangement takes place, accompanied by the formation of physical interparticle necks. This stage is crucial for achieving further densification of the material. The process differs depending on the nature of the material being used. For materials that dissolve in water as free ions, such as electrolytes, precipitation occurs during Stage II. On the other hand, materials like $SiO_2$, which are chemically bonded with water, undergo a poly-condensation reaction,

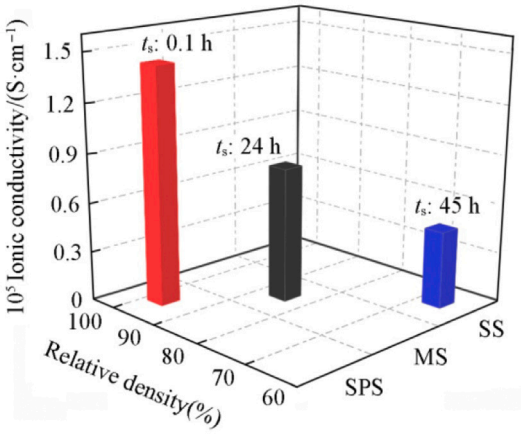


**Fig. 26.** A comparison of how sintering time affects the relative densities and ionic conductivities of various electrolytes — copied with permission from [138].

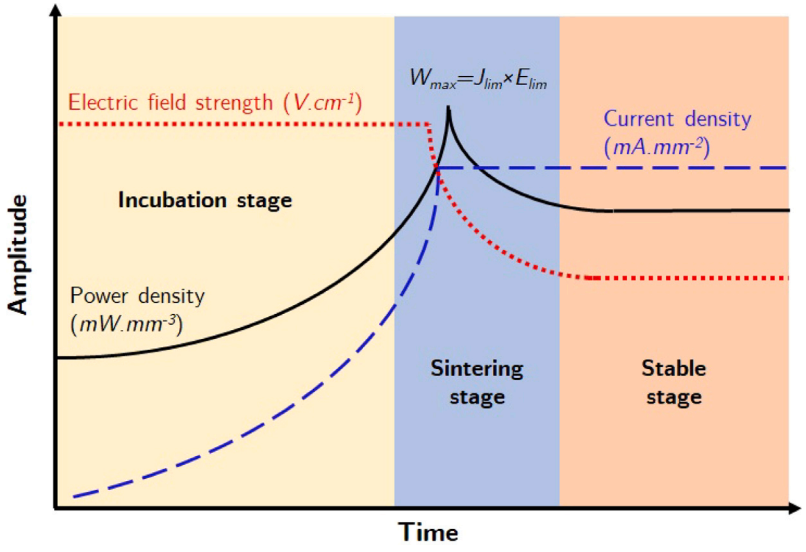


**Fig. 27.** Electric field, current density, and power density, over time in a typical FS method.

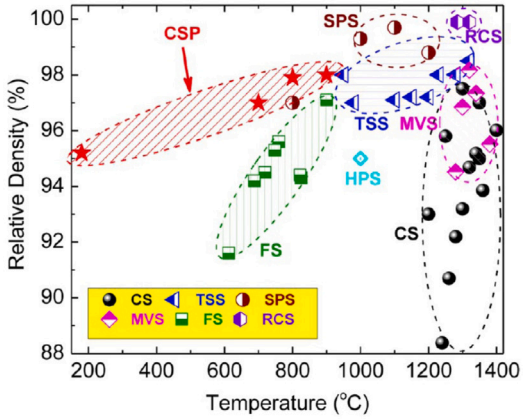


**Fig. 28.** The cold-sintered materials' relative density to alternative sintering methods (Cold sintering process (CSP), Two-step sintering (TSS), Flash sintering (FS), High-pressure sintering (HPS), Spark plasma sintering (SPS), Microwave sintering (MVS), Rate-controlled sintering (RCS)) — copied with permission from [142].

forming a gel that tends to shrink during drying [117,143]. During Stage II, the solid particles form a rigid skeleton, preventing further shrinkage. To achieve further densification, particle shape modification becomes necessary. Fig. 29 shows a comparison of isostatic cold consolidation (ICC) and uniaxial cold sintering process (UCS). In the (ICC) approach — Fig. 29(a) — the parent powder is embedded in a gel produced through dissolution and condensation. On the contrary, in the (UCS) approach — Fig. 29(b) — external pressure is maintained during Stage II, leading to the formation of polygonal grains and flat/thin boundaries. The amount of liquid used during UCS determines whether

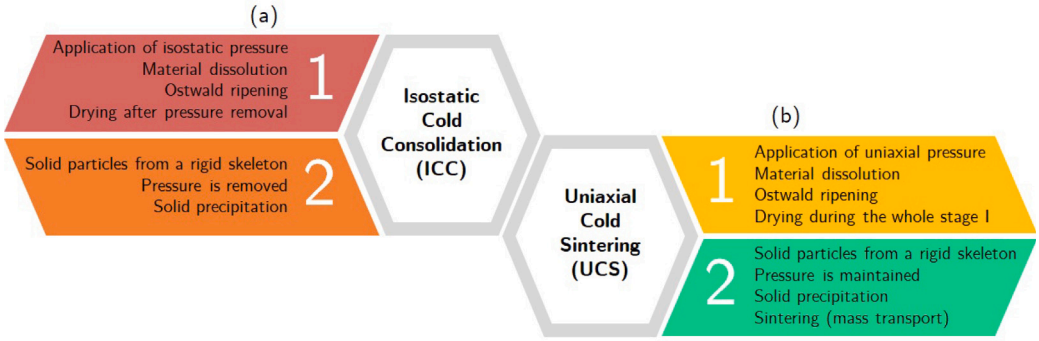


**Fig. 29.** Comparison of isostatic cold consolidation (ICC) pressing and uniaxial cold sintering (UCS), in which pressure is held constant throughout the sintering process.

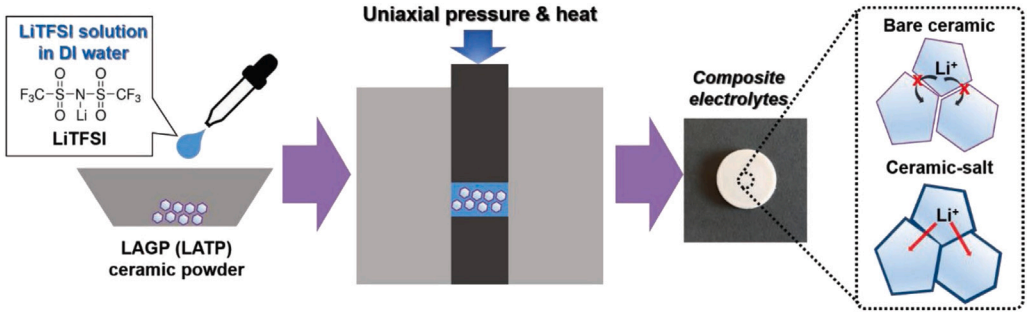


**Fig. 30.** A schematic illustration of a composite electrolyte made from ceramics and organic Li salts produced during CSP — copied with permission from [144].

the pores are filled or not. If the pores are filled with water, an interparticle liquid film is expected to remain, reducing the pressure gradients and driving force for sintering. However, if the pores are not filled, the liquid may be squeezed out from the interparticle region to the unfilled pores due to the applied external pressure. Understanding the mechanisms of densification during UCS is still an area of ongoing research. The driving force behind CSP lies in the reduction of activation energy required for diffusion. This reduction is achieved through the introduction of chemical additives that facilitate atomic mobility and assist in the formation of necks between particles. The additives lower the energy barrier for diffusion, promoting densification at lower temperatures. Additionally, the application of pressure helps to consolidate the material and enhance densification [143].

The success of CSP depends on a range of physical and chemical factors, including the selection of starting materials and solvents, as well as various physical parameters. An important step in the process is creating the appropriate aqueous solution with the necessary chemical constituents. The combination of liquid-assisted particle sliding and hydrothermal-assisted sintering procedures in CSP allows for operation within a relatively low-temperature region compared to conventional sintering processes [117,141]. One of the challenges of CSP is drying and solvent removal. To remove residual solvents completely, a meticulous drying process must be employed. It is still necessary to develop energy-efficient drying and sintering processes to further reduce energy consumption. As seen in Fig. 30, Lee et al. [144] added the salt by dissolving in the CS solvent. The resultant materials are cold sintered once pressure and heat are applied. In order to get densified electrolytes, they adjusted the uniaxial pressure during CSP and discovered that relative densities progressively rise as pressures rise.

CSP presents a promising opportunity to densify ceramic SEs, which are often temperature-sensitive and can be prone to degradation at high sintering temperatures. It is particularly suitable for fabricating thin-film SSBs. CSP not only enables the consolidation of ceramic particulates and composites at ultra low temperatures but also opens up new routes for integrating materials and devices, thus facilitating the fabrication of novel composites. Additionally, this technology allows for the sintering of thermally fragile ceramic SEs for both lithium ions ($Li^+$) and sodium ions ($Na^+$), while offering significant energy and cost savings compared to traditional sintering processes [117].

SEs used in batteries often face challenges due to resistive grain boundaries that impede the transport of lithium ions. To enhance interconnectivity between grains, high-temperature sintering is typically employed. However, this method has drawbacks, including lithium loss and the formation of secondary phases. While sulfide-type electrolytes can be densified at room temperature due to their low modulus, oxide-type electrolytes still require high-temperature treatment to improve mass transport between particles. Improved density, bonding between grain boundaries, and solubility of target materials in liquid solutions contribute to the enhanced ionic conductivity of SSBs. Cathodes require special protection, necessitating the study of surface protection techniques and coating materials [127,145,146].

The CSP presents an exciting opportunity to fabricate multi-layered ceramic devices without the need for a firing step. It offers a promising "all in one step" solution to device manufacturing, potentially surpassing conventional processing routes. One common SE material that has been successfully cold-sintered is lithium garnet oxide LLZO. $Li_{6.4}La_3Zr_{1.4}Ta_{0.6}O_{12}$ (LLZTO)/polyethylene-oxide (PEO) electrolyte containing a lithium salt was successfully fabricated into bulk pellets via the CSP. Above 80% dense composite electrolyte pellets were obtained, and a high Li-ion conductivity of $2.4 \times 10^{-4}$ S $cm^{-1}$ was attained at room temperature [146]. CSP offers a viable alternative, allowing for densification at lower temperatures and preserving the desired microstructure and ionic conductivity of LLZO. It is reported that two lithium-based compounds, $Li_{6.25}La_3Zr_2Al_{0.25}O_{12}$ (LLZAO) and $LiCoO_2$ (LCO), could be cold sintered using aqueous solutions. It was noted that LLZAO had a relative density of 87%, whereas LCO reached 95% using 10% LLZAO as a flux/binder. LLZAO sintered as-cold exhibited a low total conductivity ($10^{-8}$ S $cm^{-1}$), attributed to $Li_2CO_3$ blocking the grain boundary. To reduce the blocking layer, deionised water was replaced during CSP with 5M LiCl to achieve a total conductivity of $\approx 3\times10^{-5}$ S $cm^{-1}$. Fig. 31 shows the relative density of the LCO-LLZAO composite ceramics sintered at different pressures,

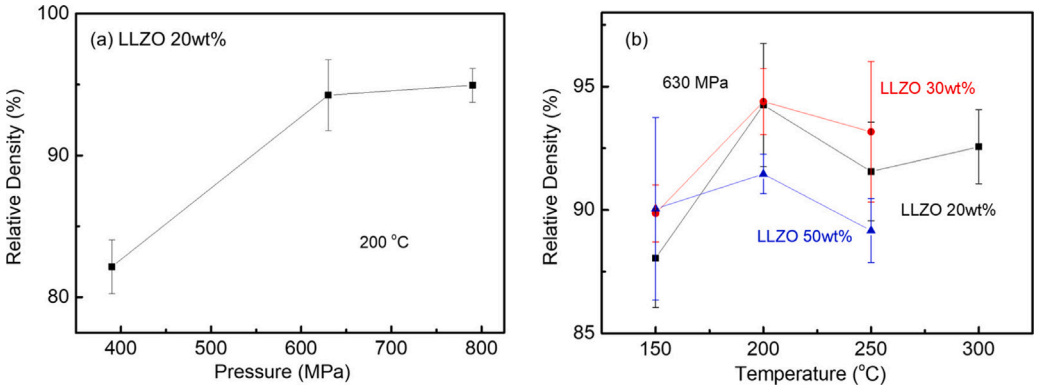


**Fig. 31.** LCO-LLZAO relative density sintered at various (a) pressures and (b) temperatures for different amounts of LLZAO — copied with permission from [147].

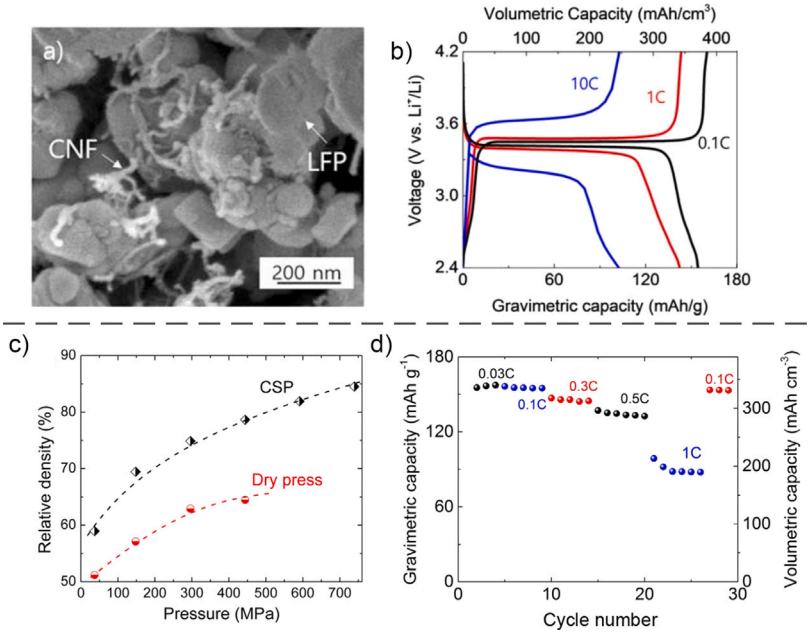


**Fig. 32.** (a) SEM image of LFP/CNF mixture, (b) voltage profiles of LFP cathode that at different current densities; — copied with permission from [148]. (c) Densities of $LiFePO_4$ ceramics sintered for 30 min at 240 °C and prepared by CSP at different pressure levels. Ceramics made without liquid phase addition are also included for comparison. Dry pressed pellets are not obtainable over 450 MPa. (d) The discharge rate cyclability of a cold sintered LFP/CNF at different current densities — copied with permission from [149].

temperatures, and LLZAO weight fractions. Up to 200 °C and 630 MPa, LCO-LLZAO composites increase initially in density but then remain unchanged. When LLZAO is at about 20%, its weight fraction does not have much impact on density, suggesting that it acts as a fluxing agent/binder whose concentration should be minimised to maximise the electrical properties [147].

In recent research, Carbon nanofibre (CNF)/$LiFePO_4$ (LFP) composite cathodes were synthesised and showed cycleability even at a high 10C current rate (Fig. 32(a–b)) [148]. Also, the CSP has shown great potential in bridging the sintering temperature gap between ceramic and polymer materials, particularly for improving the density of LFP-based cathodes. By utilising CSP, LFP ceramics can be densified and cathodes containing active carbon and Polyvinylidene fluoride (PVDF) can be produced at a low temperature of 240 °C. Density is clearly improved when compared to LFP ceramics that were dry pressed without the addition of aqueous solution (Fig. 32 (c)). These cathodes exhibit enhanced volumetric capacity, making them suitable for EVs and hybrid electric vehicles (HEVs) (Fig. 32 (d)) [149].

CSP was used to fabricate a densified binder-free LTO anode. Initially, the composite anode was tape cast with a binder, and then it was heat treated to remove the binder. A transient liquid phase was produced by humidifying the binder-free composite with water. Under a uniaxial pressure of 500 MPa, 120 °C cold sintered wetted composites were directly deposited on current collectors. LTO/CNF composite anodes have a density of 2.82 g $cm^{-3}$ (87% relative density). Cold sintered anodes had volumetric capacity densities of 380 mAh $cm^{-3}$ [150].

Additionally, Berbano et al. utilised CSP to fabricate $Li_{1.5}Al_{0.5}Ge_{1.5}(PO_4)_3$ (LAGP) SE, effectively improving its ionic conductivity. The CSP method has been successfully applied to obtain 80% dense LAGP electrolytes at 120 °C in just 20 min, followed by a short belt furnace treatment. The resulting LAGP SE exhibits improved ionic conductivity. Furthermore, the incorporation of water as a solvent during the CSP process for LAGP/(PVDF-HFP) composites has led to increased conductivity and reduced activation energy for ionic conductivity. A summary of the processing parameters on the obtained conductivities at 25 °C and suggested processes of lithium-ion conduction are presented in Fig. 33. Fundamental scientific problems need to be answered using computational and experimental methods in order to fully benefit from CSP [151].

In the case of NASICON materials, magnesium (Mg) doping has been found to substantially increase densification during CSP. By converting primary NASICON from the monoclinic to the rhombohedral phase and producing conductive $Na_3PO_4$ secondary and/or interfacial phases,

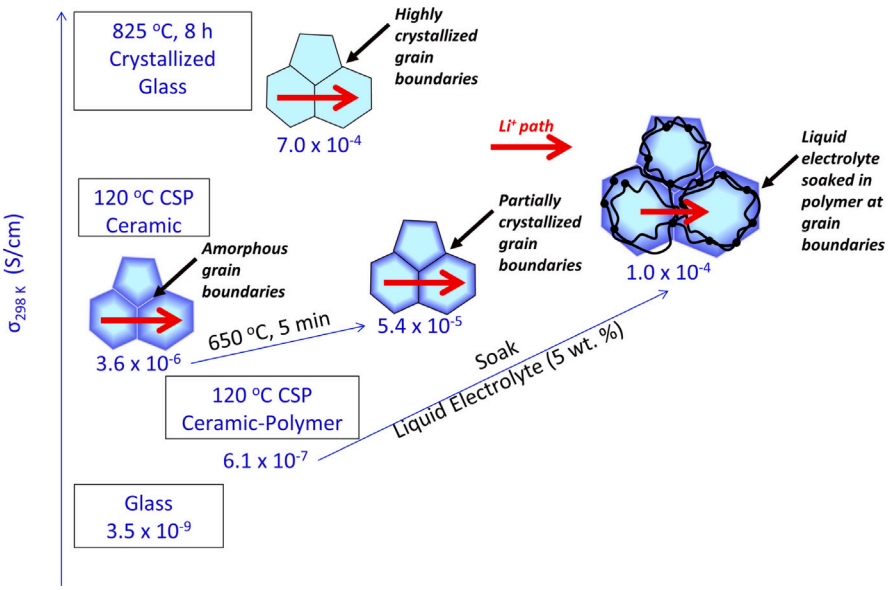


**Fig. 33.** An overview of how processing affected the overall conductivities at 25 °C for glass, bulk crystallised glass, cold sintered ceramic (both before and after a 5-minute, 650 °C belt furnace heat treatment), and cold sintered ceramic polymer composite (both before and after soaking in five weight percent liquid electrolyte). The red arrow indicates a series pathway that represents the anticipated lithium-ion conduction channel — copied with permission from [151].

magnesium doping facilitates CS. Mg-doped NASICON specimens that were cold-sintered showed a tendency to densify as pressure increased, with the CSP temperature having minimal impact on the ultimate density. However, the cold-sintered NASICON specimens exhibited relatively low ionic conductivity, which could be attributed to the presence of secondary phases that form when NASICON comes into contact with water. Fortunately, these secondary phase particles were reduced after annealing at temperatures of 800 and 900 °C [152]. Pereira da Silva et al. [125] demonstrated that both FAST/SPS and CSP enabled the fabrication of scandium-substituted NASICON electrolytes with electrical resistivity approximately an order of magnitude higher than those obtained through conventional sintering methods.

$V_2O_5$ and carbon-nanofiber composites were prepared at 120 °C (350 MPa, 20 min) as cathode materials using CSP. Furthermore, a composite of $V_2O_5$ and polymers was created, which exhibited a significant increase in electronic conductivity, surpassing that of pure $V_2O_5$ by more than two orders of magnitude. Additionally, a covalently bonded $MoS_2$/graphite composite showcased its potential as a high-capacity Li-ion electrode [153,154].

The future outlook for CSP in SSB is highly promising. The production of numerous components, such as electrolytes and cathodes, has shown incredible progress using CS, demonstrating the considerable potential of this process in the advancement of energy storage devices [118,127].

### 3.4. FS

FS is a revolutionary electric field-assisted sintering technique that offers remarkable advantages over conventional sintering methods for ceramics. By employing an electric field, FS can significantly reduce the initial sintering temperature and sintering time, resulting in substantial energy savings and the potential for achieving significant carbon emission reductions [120,122]. To carry out FS effectively, a specific experimental setup is required. This setup typically consists of three fundamental components: a furnace, a power supply, and electrodes. For studying the FS process, dog bone-shaped samples are often preferred due to their ability to reduce issues associated with current concentration. The application of an electric field is initiated when the furnace temperature is relatively low, and the power source initially operates under voltage control. As the furnace temperature reaches a certain threshold, the material's electrical resistivity abruptly drops, resulting in a sudden surge in current, known as the flash event. The power supply then switches to current control, maximising power dissipation. This flash transition phase is characterised by a thermal runaway of Joule heating and the highest power dissipation. Upon reaching the current limit, the system achieves an equilibrium stage, marking the onset of steady-state FS [120,122]. A schematic representation of a single FS setup is shown in Fig. 34. After passing two wires through the holes in the dog-bone specimen, the sample was hung in a vertical tube furnace [139].

FS is highly dependent on the electrical properties of the specimen, making it a versatile method that has been applied to a wide variety of ceramics. There are a variety of ceramics that exhibit diverse electrical properties, from ionic conductors to semiconductors to protonic conductors to Li-ion conductors to electronic conductors [155]. Specimen geometry, electrical field strength, current density, and atmosphere are parameters that have an impact on FS [120]. A notable characteristic of FS is the nonlinear increase in electrical conductivity, which creates an ultra-rapid heating effect. Interestingly, materials exhibiting a negative temperature coefficient for resistivity, indicating an increase in conductivity with temperature, are more amenable to FS. Despite the wide applicability of FS, the underlying mechanism behind this phenomenon remains unclear. Several mechanisms have been proposed to elucidate the rapid and unconventional densification observed during FS, with each closely related to one of three factors affecting mass transport: defects population, driving force for diffusion, and sintering stresses and defects concentration gradients. The thermal runaway model explains the conditions leading to FS based on the balance between electrical power input and heat dissipation by the specimen [124]. As well as the applied field, the electrical properties of the material being tested affect the onset of thermal runaway. It is important to recognise the extremely high heating rates experienced during FS when considering Joule heating. Another proposed mechanism revolves around preferential Joule heating at grain boundaries, leading to enhanced diffusion coefficients and the formation of space charge, thereby increasing local power dissipation. Furthermore, the field-induced generation of Frenkel pairs within ceramic grains has been suggested as an initial mechanism for FS, as these defects have the potential to generate electronic disorder and discharge lattice defects [120–122]. The formation of partially electrochemically reduced structures has also been proposed as a possible mechanism of FS [120].

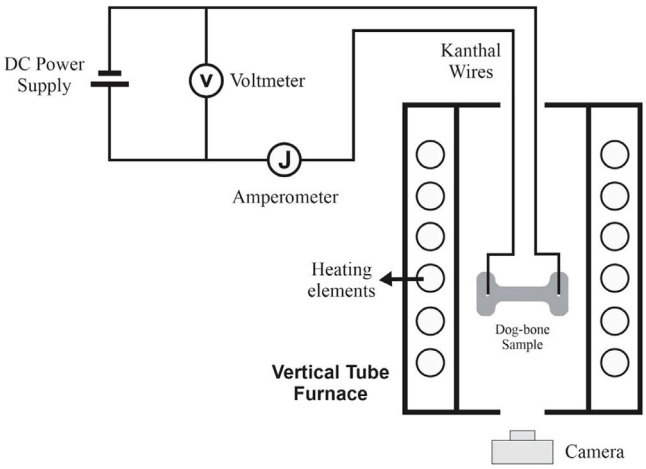


**Fig. 34.** Schematic of FS setup — copied with permission from [139].

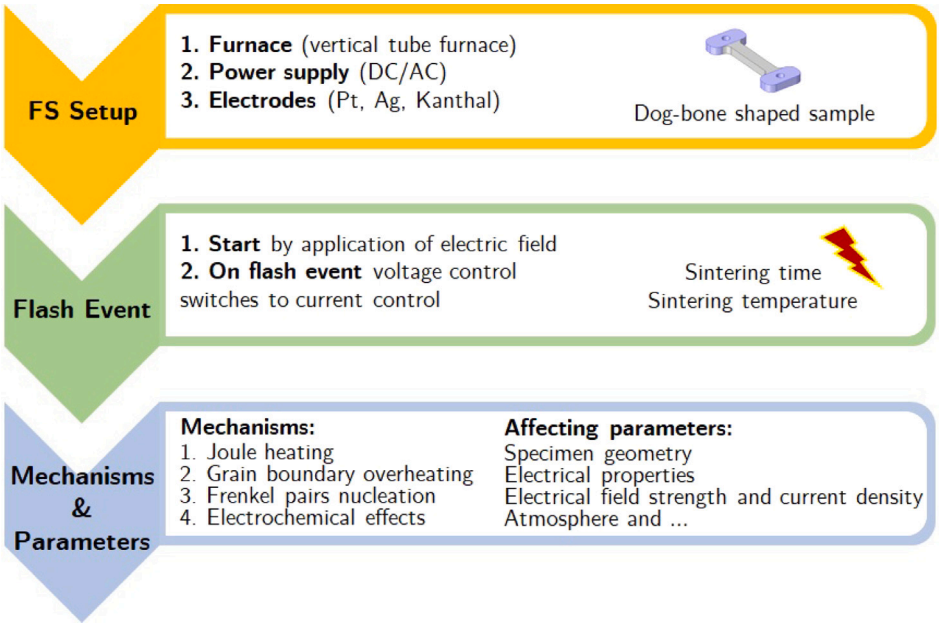


**Fig. 35.** A glimpse into the energy-efficient method of FS.

This innovative technique allows ceramics to be sintered within a matter of seconds, presenting three prominent advantages compared to traditional sintering: lower furnace temperature requirements, faster heating rates, and shorter overall sintering duration. Furthermore, when compared to SPS, FS demonstrates additional benefits that make it an attractive choice in certain scenarios. One notable advantage of FS over SPS is the inherent simplicity and lower cost of equipment required for FS. Unlike SPS, which necessitates specialised tooling, such as a sample chamber with graphite die and punches, FS can be performed using relatively simpler setups. This not only reduces the initial investment required but also lowers maintenance costs. However, FS does pose several challenges that need to be addressed. The creation of temperature gradients is a crucial problem as it is directly linked to the creation of preferred current routes inside the ceramic sample. Localised hot pathways and localised overheating may result from these thermal gradients. One of the primary limitations of the FS process is the formation of hot spots, which has led researchers to focus on finding technical solutions. The generation of hot spots is triggered by temperature inhomogeneity, which can arise from a temperature gradient between the core and surface or microstructural heterogeneity and local melting [120–122]. Dong's [156] predictive model for hot-spot formation during FS successfully identified a critical perturbation size that triggers localised thermal runaway and the occurrence of hot spots. To prevent hot spot formation, it was suggested to use of travelling electrodes, which are the most straightforward solution [156]. Fig. 35 provides a comprehensive overview of FS. It visually summarises the process, key mechanisms, and crucial affecting parameters.

In the realm of SSBs, FS is employed to shape and sinter multi-material systems. In a study conducted by Lachal et al. [157], FS was utilised to densify LCO as the ideal material for ensuring a fast charge transfer reaction. To enable FS in $Li^+$, $Na^+$, $K^+$, or other ionic conductors, a reversible electrochemical reaction between alkaline cations and electrons is crucial for triggering the flash event through DC polarisation [158]. Interestingly, LCO, a mixed conductor of electronic and $Li^+$, demonstrated the ability to undergo FS without the need for an interfacial electrochemical reaction. The research also explored the use of multi-layer systems, including a configuration with LCO or a LATP+LCO composite as electrodes and LATP as the electrolyte, which exhibited promising results with reduced mechanical stresses at the interface between the layers. As shown in Fig. 36(a) and (b), FS can enhance the ionic conductivity and activation energy compared to conventional sintering. SEM image — Fig. 36(c) — shows some cracks

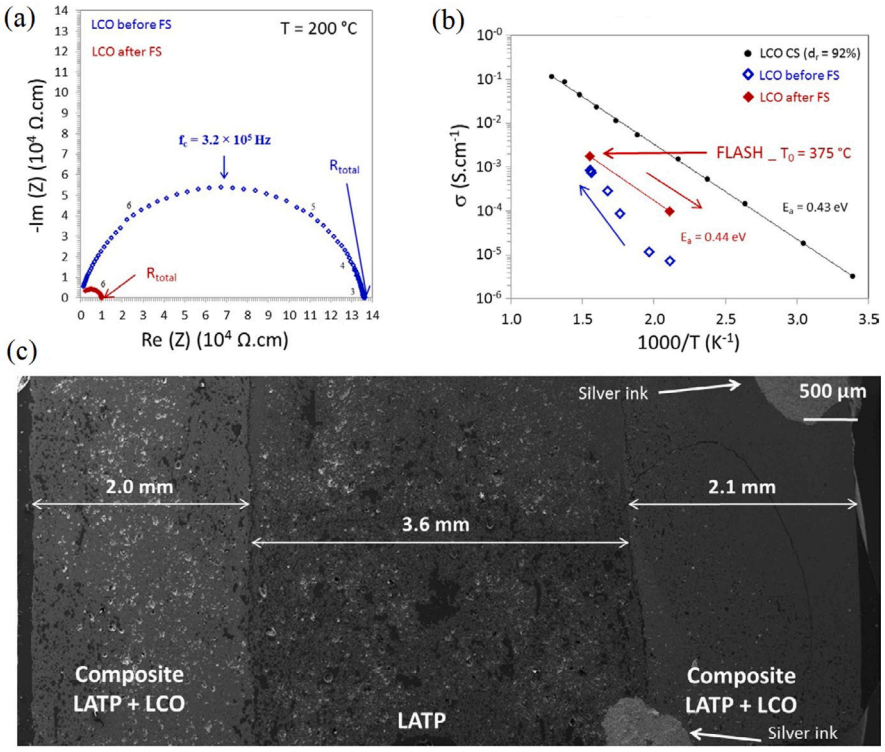


**Fig. 36.** (a) Arrhenius plots of the green LCO sample before (blue diamonds) and after (red diamonds) FS in comparison to traditional sintering of the LCO pellets; (b) Nyquist plot at 200 °C before and after FS on LCO sample; (c) Composite/LATP interface SEM picture — copied with permission from [157]. (For interpretation of the references to colour in this figure legend, the reader is referred to the web version of this article.)

at the interface between LATP and the LCO+LATP composite, but no delamination. Using this composite has reduced mechanical stresses at the interface [157].

In another study conducted by Ren et al. [159], FS was employed to densify NZSP ($NaZr_2(PO_4)_3$) under both direct current (DC) and alternating current (AC) electric fields, with measurements taken to evaluate the resulting ceramic conductivity. FS was conducted at a furnace temperature of 700 °C. The results showed that the DC flash-sintered NZSP sample exhibited impurity phases such as $Na_2ZrSi_2O_7$ and m-$ZrO_2$, attributed to the accumulation of sodium at the cathode during FS (See Fig. 37(b) and (c)). In contrast, the AC flash-sintered NZSP sample demonstrated near-pure NZSP composition with minimal traces of $ZrO_2$, indicating improved stoichiometric control, which can be seen in Fig. 37(a). Notably, the flash-sintered NZSP samples exhibited higher conductivities compared to pressure-less sintered NZSP samples. Clemenceau et al. [160] used FS to densify LLZO at 190 mA mm$^{-2}$ at 850 °C and achieved a relative density of 96%. In another study, Sazvar et al. [161] demonstrated that increasing the electric field strength from 40 to 100 V cm$^{-1}$ in FS of LALZO significantly reduced the incubation time, reaching as low as 2 s at 100 V cm$^{-1}$. This finding highlights the strong influence of voltage on the sintering kinetics and suggests the potential for efficient and rapid densification of LALZO materials.

Reactive flash sintering (RFS) is a variation technique that may be customised to produce non-equilibrium metastable materials by lowering furnace temperature and processing periods. RFS settings may be varied over time in-situ measurements, which can show how they affect crystallisation routes [162]. As an alternative, ex-situ characterisations, which halt the flash experiment many times, are an effective strategy. One class of LIB materials that stands to gain from RFS's shortened manufacturing time is SSE. Avila et al. [163] employed RFS to fabricate Al-LLZO ceramics using a chemically prepared multiphase precursor powder. The highly reactive powder was prepared through the Pechini method, enabling the production of single-phase Al-LLZO ceramics within a specific range of electrical parameters (50 V cm$^{-1}$ and 150 mA mm$^{-2}$) at an isothermal condition of 600 °C for 30 s. The study suggests that RFS holds promise for stabilising phases under kinetic control and highlights the observation of asymmetric effects, including cation migration, during the FS process. In-situ X-ray diffraction measurements revealed that the field process favoured the formation of intermediates, altering the phase evolution of the material. Moreover, Campos et al. [164] successfully demonstrated the first simultaneous sintering and crystallisation of LAGP ($Li_{1.5}Al_{0.5}Ge_{1.5}(PO_4)_3$) samples using FS. By varying the holding time at a furnace temperature of 500 °C, it was observed that higher current densities and longer holding times promoted larger crystallite sizes without significant lithium volatilisation (Fig. 38). This highlights the potential of flash sinter-crystallisation, a variant of FS, to rapidly obtain glass-ceramics from LAGP glasses within seconds using electric field and Joule heating as primary energy sources. Also, FS has achieved a significant milestone by successfully synthesising spinel $Li_4Ti_5O_{12}$ (LTO) in just 5 min at a furnace temperature of 580 °C, as reported by Liu et al. [165] the flash-sintered samples showcased higher initial discharge capacity, increased discharge capacity, and improved cycling stability when compared to conventionally synthesised samples. This enhanced performance can be attributed to FS's ability to inhibit lithium volatilisation and reduce particle size, leading to an increased active surface area and a shortened lithium-ion transfer path.

### 3.5. Sintering modelling

The simulation of the CSP process remains relatively scarce in the current literature, with a notable lack of studies focusing on its application to battery-related materials [143]. Typically, models are derived from the liquid-phase sintering paradigm. This process necessitates particle rearrangement facilitated by the sliding motion of solid particles against each other, aided by a lubricating liquid film [166]. In one study, a theoretical model based on ordinary differential equations (ODEs) was devised for BaTiO3 particles. This model posited the

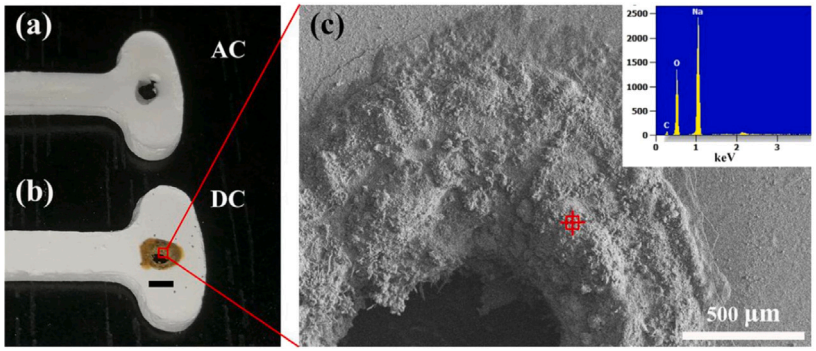


**Fig. 37.** (a) AC and (b) DC images of flash-sintered samples; (c) SEM image of the cathode zone under a DC electric field — copied with permission from [159].

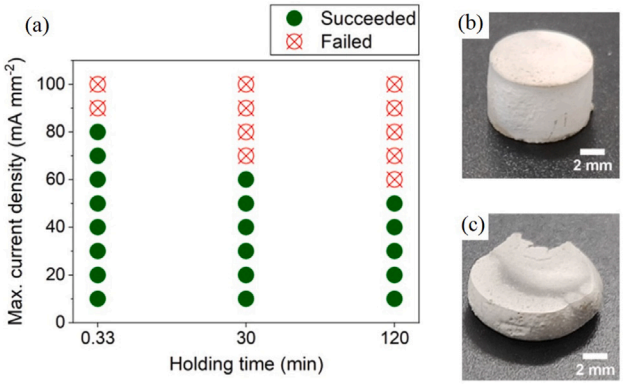


**Fig. 38.** (a) LAGP glass-ceramic sinter-crystallisation processing map with current ramp control. (b) flash sinter-crystallised sample with a maximum current density of 40 mA $mm^{-2}$, (c) failed flash sinter-crystallised sample with a maximum current density of 60 mA $mm^{-2}$ — copied with permission from [164].

formation of amorphous BaTiO3 particles through chemical reactions followed by nucleation from the aqueous solution, consistent with Ostwald's rule of stages [167]. In another investigation, a distinct model was formulated to elucidate the CSP of lead zirconate titanate (PZT) utilising moistened lead nitrate as a sintering aid. This model assumed plastic deformation of lead nitrate under uniaxial pressure in an attempt to define the effects of temperature and pressure during CSP [168]. Finally, one study utilised ReaxFF molecular dynamics (MD) simulations to investigate zinc cation recrystallisation under varying acidic conditions, revealing surface adsorption as a potential rate-limiting factor in CSP [169]. The ReaxFF MD simulations are capable of modelling reactive liquid/solid interfaces at high temperatures and pressures [169,170].

In the field of FS, there is a predominance of numerical studies. Advancing in this area requires a deeper understanding of the complex and dynamic nature of FS. The electrical response of the specimen during the FS process is complicated by various factors, such as the transformation from a powder compact to a dense ceramic and the surge in current during the "flash event" [124]. In this context, numerical simulations play a crucial role in understanding and optimising the FS process. These simulations allow researchers to study the complex phenomena occurring during FS, which are often difficult to observe experimentally. This helps in reducing the need for extensive experimental trials, saving time and resources. By using numerical simulations, researchers can gain insights into the temperature distribution, electric field distribution, and material behaviour during FS [23,155]. This information helps in identifying the optimal parameters for achieving desired material properties and enhanced sintering efficiency. Furthermore, numerical simulations aid in understanding the underlying mechanisms of FS, enabling researchers to propose new theories and hypotheses. These insights can then guide further experimental investigations and contribute to advancing the understanding of this innovative sintering technique. It is worth mentioning that several mathematical models have been proposed to explain specific stages or phenomena of flash, including the thermal runaway model, the black body radiation model, and the dog-bone model [121,124,171]. Many articles in the field have utilised COMSOL Multiphysics for simulating various aspects of the process. Its versatility and ability to model coupled multiphysics phenomena make it a valuable tool for studying FS [155].

Successful simulation of FS within the COMSOL Multiphysics framework requires a rigorous consideration of key equations and a precise characterisation of electric field distributions. Maxwell's equations form the cornerstone for this endeavour:

$$\nabla \mathbf{J} = 0, \tag{4}$$

$$\mathbf{E} = -\nabla U, \tag{5}$$

$$\mathbf{J} = \sigma \mathbf{E}, \tag{6}$$

where $\nabla$, $\sigma$, $U$, $\mathbf{E}$, and $\mathbf{J}$ represent the spatial gradients, the electrical conductivity, the electric potential, the electrical field vector, and the current density vector. The distribution of electric current within the sample is pivotal for comprehending the FS process. The flow of electric current can be described by the third equation, often referred to as Ohm's Law [172].

Joule heating arises due to electrical resistance within the material, resulting in the conversion of electrical energy into heat. The Joule heating equation is succinctly expressed:

$$Q_e = (-\nabla U)\sigma(-\nabla U) \tag{7}$$

And the final Heat transfer equation is:

$$\int \rho C_p \frac{\partial T}{\partial t} dV = \int \nabla(k \nabla T) dV + \int Q_e dV \tag{8}$$

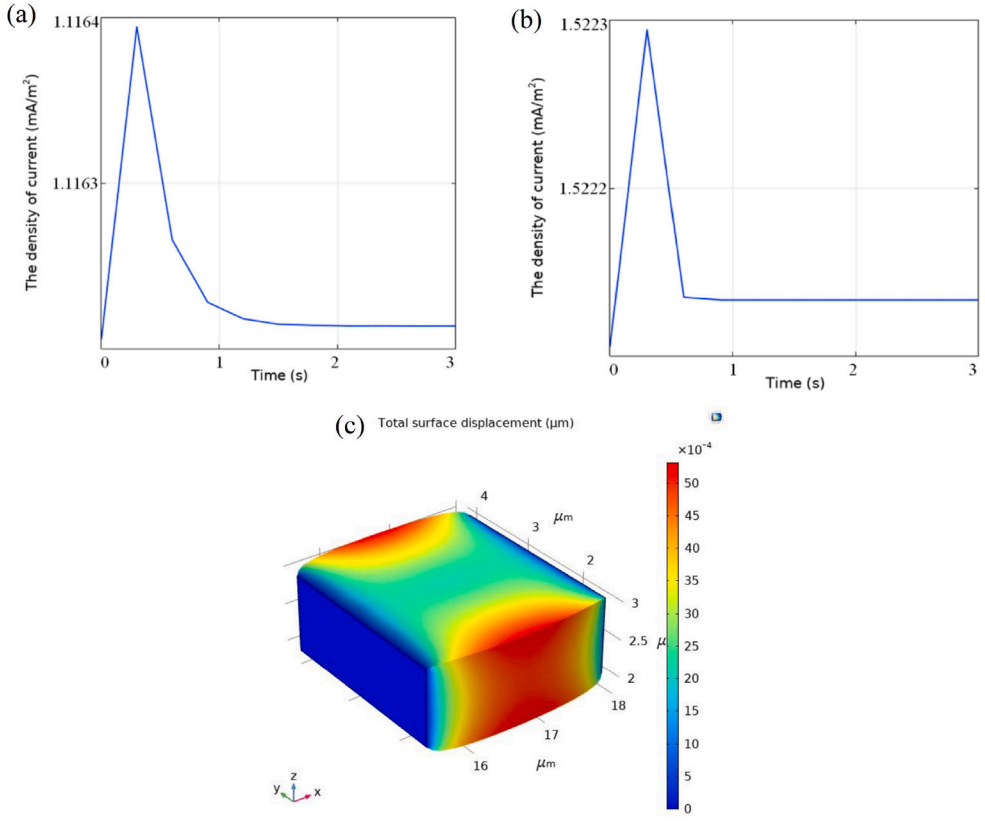


**Fig. 39.** Change in current density with time in (a) 150 V cm$^{-1}$, (b) 300 V cm$^{-1}$ electric field. (c) Change in sample surface displacement when 300 V cm$^{-1}$ electric field intensity is applied — copied with permission from [175].

where $\rho$, $C_p$, $T$, $t$, $V$, and $k$ are the density, specific heat, temperature, time, volume, and thermal conductivity, respectively. In COMSOL Multiphysics, these equations are coupled, enabling the simultaneous simulation of electrical, thermal, and, if applicable, phase-change phenomena [121,171,173].

Depending on the material and any associated phase changes during FS, phase transformation equations may be incorporated, accounting for phase transitions, latent heat, and other material-specific properties [174]. The densification of the material is described with a partial differential equation linking the rate of change of the density with the temperature and instantaneous density:

$$\left(\frac{1}{\rho^*}\right)\left(\frac{\partial \rho^*}{\partial t}\right) = f(\rho^*)g(T) \tag{9}$$

where $\rho$ is relative density and then $f(\rho^*)$ and $g(T)$ are functions of relative density and temperature, respectively, which are derived from the experimental results. Using the thermal strain multiphysics feature in the "Solid Mechanics" COMSOL module, the rise in density is converted into uniform isotropic shrinkage, assuming a small amount of mass loss during the sintering process:

$$\epsilon_t = \left(\frac{\rho_g}{\rho}\right)^{\left(\frac{1}{3}\right)} - 1 \tag{10}$$

where $\epsilon_t$ is the linear thermal strain [171].

The observation of electro-luminescence during FS suggests the generation of defect states with accessible energy levels in the bandgap of the material, indicating the presence of unique energy states during the flash event. Mesoscopic models, such as the free energy formulation proposed by Vikrant et al. [176], contribute to a thermodynamically consistent description of charged interfaces in ionic ceramics, filling an important knowledge gap in understanding macroscopic transport properties. Previous work has explored classic mesoscopic models for FS, highlighting that local Joule heating hot spots alone cannot physically justify the large thermal gradients observed on longer timescales. Moreover, atomistic simulations and experimental results indicate that the motion of defects and electrically charged grain boundaries play a significant role in the rapid atomic reconfiguration, grain growth, and densification processes observed during FS [155,177].

In one study, FS of alumina samples was studied using two simulation models. Material Studio, a simulation software, was employed to apply boundary conditions of electric field intensity and external temperature for FS simulations [175,178]. The results showed that under high temperatures and high electric field intensity, the atoms in the alumina material became more densely arranged, leading to increased densification. The bond length of the alumina unit cell was observed to decrease as temperature and electric field intensity increased, reaching a peak where the density remained constant. Also, COMSOL Multiphysics was utilised to simulate the FS process by considering electrical, thermal, and other physical fields, including Joule heat and thermal expansion [175,179]. The FS simulation involved four steps: geometric model construction, addition of materials, setting of boundary conditions, and mesh division. The FEM simulation method revealed a temperature gradient between the surface and inside of the sample during FS, with several regions on the sample surface exceeding 800 K. In Fig. 39(a), the curve of the current density through the sample changing with time is shown with 150 V cm$^{-1}$ electric field intensity. Compared to Fig. 39(b), the electric field intensity becomes smaller and the incubation phase lasts longer. It shows that the intensity of the electric field affects the incubation time. Additionally, it was observed that current density influenced the temperature, displacement of the sample surface, and grain size, all of which are crucial factors in determining the microstructure and properties of ceramic materials during the sintering process [175](see Fig. 39 (c) for example).

The FS phenomenon was simulated by varying the electric power supplied to the samples under electric fields ranging from 60 to 120 V

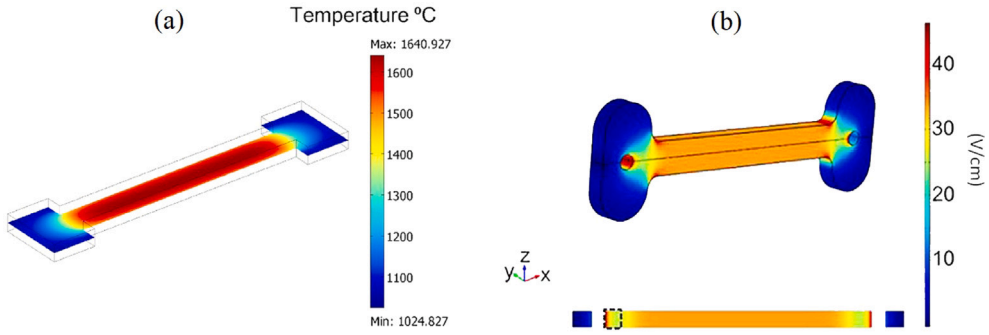


**Fig. 40.** (a) FEM simulation shows the temperature distribution of the 3YSZ sample under the assumption that a 70 W electric power source is applied for three seconds. Along the sample gauge portion, there was an electric field of 120 V $cm^{-1}$. Before the application of the 120 V $cm^{-1}$ electric field, the temperature of the furnace sample was 850 °C — copied with permission from [173], (b) FEM modelling results for the electric field strength at the sample's surface and taken from a plane perpendicular to the *z*-axis within the sample's volume — copied with permission from [180].

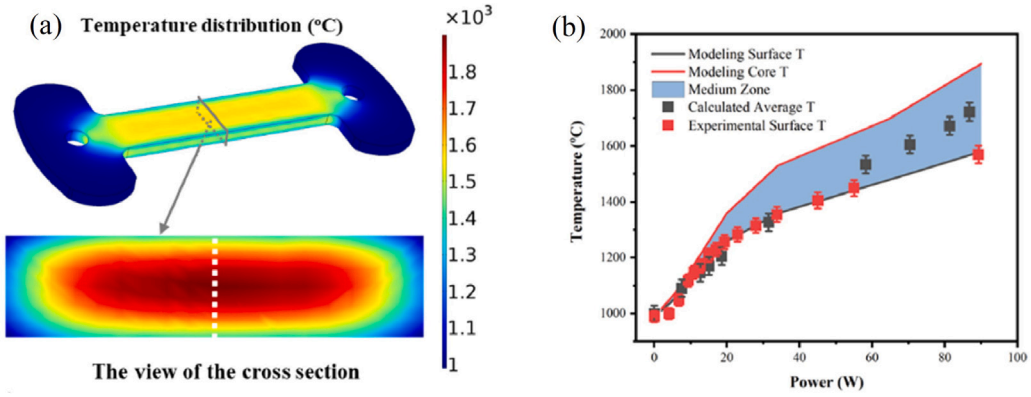


**Fig. 41.** (a) The YSZ/PVA-0.5 specimen's temperature distribution during free FS at 1000 °C; (b) A comparison between the temperature derived from FEM modelling, the experimental surface temperature, and the calculated average temperature — copied with permission from [181].

$cm^{-1}$ (Fig. 40(a)). Due to the high heating rate and small sample cross-section, reliable temperature measurements were challenging to obtain. By solving the governing equations, including Maxwell's equation and the energy balance equation, along with considering heat conduction, convection, and radiation, the simulations accurately captured the temperature rise during FS. The results demonstrated that the sudden increase in electric current corresponded to the FS phenomenon, with the temperature of the zirconia samples rising rapidly within a few seconds [173]. In a different study, Qin et al. [180], investigates the microstructure evolution in DC and AC FS processes. Their findings emphasise the need to consider electrode effects during microstructure formation, as evidenced by significant grain size gradients near the cathode in DC-sintered samples. The inhomogeneous grain size distributions observed near the electrodes in both AC and DC flash-sintered specimens further support the influence of electrode effects in the sintering process. Inhomogeneity of the current passage resulted in non-uniform properties and potential cracking, which could be addressed by modifying the electrode configuration to enhance current homogeneity — see Fig. 40(b).

Xiao et al. [181] explored the impact of FS on constrained sintering in a bilayer of 3 mol% yttria-stabilised zirconia (3YSZ) with Polyvinyl alcohol (PVA), uncovering insights into stress development at the YSZ interface under varying electrical fields. Their findings revealed that FS mitigates the constrained sintering effect by promoting vacancy and interstitial defect formation, facilitating accelerated shear stress relaxation. The cross section temperature distribution can be seen in Fig. 41(a). The low viscosity achieved during FS, primarily induced by the electrical field, enhances plastic deformation capability and activates grain boundary-related mechanisms during critical densification stages, resulting in reduced stress levels. Additionally, experimental validation of temperature measurements, depicted in Fig. 41(b), corroborated the model's accuracy. In a complementary study, simulations using COMSOL software by Li et al. [182] elucidated the significant influence of the electric arc's proximity to the sample in 3YSZ FS on heat conduction efficiency. Proximity between the arc and sample correlated positively with heat conduction efficiency, thereby enhancing FS initiation and overall energy efficiency.

Accelerated atomic diffusion is thought to be a critical element in explaining the higher densification seen during FS of ceramics [183]. Although the rapid diffusional mass transfer during the flash event is predicted to be greatly aided by the elevated specimen temperature, kinetic studies have revealed that the thermal effect is not entirely responsible for the observed accelerated densification [184]. While isolating the thermal contribution of the electric field and current from their overall effect on mass transport remains challenging, the increase in specimen temperature due to Joule heating can be confirmed through both experimental measurements and numerical calculations. To analyse the temperature distributions, a FEM approach was employed, with the electrical conductivity of 3YSZ representing the increased conductivity during the flash event. The Boltzmann–Bieler–Riedel (BBR) model predicts an increase in specimen temperature during the flash event. A voltage loss at the electrodes during the flash occurrences, however, is suggested by the mismatch between predictions and tests. According to the FEM calculations, the temperature within the specimen matches the pyrometer results, with the BBR model overestimating the temperature by less than 50 °C — c.f. Fig. 42. The ratio of touch resistance to apparent specimen resistance helps to explain this overestimation [185]. Furthermore, simulation models on Samarium doped ceria were performed Utilising FEM. The results of these simulations demonstrate significant thermal gradients between

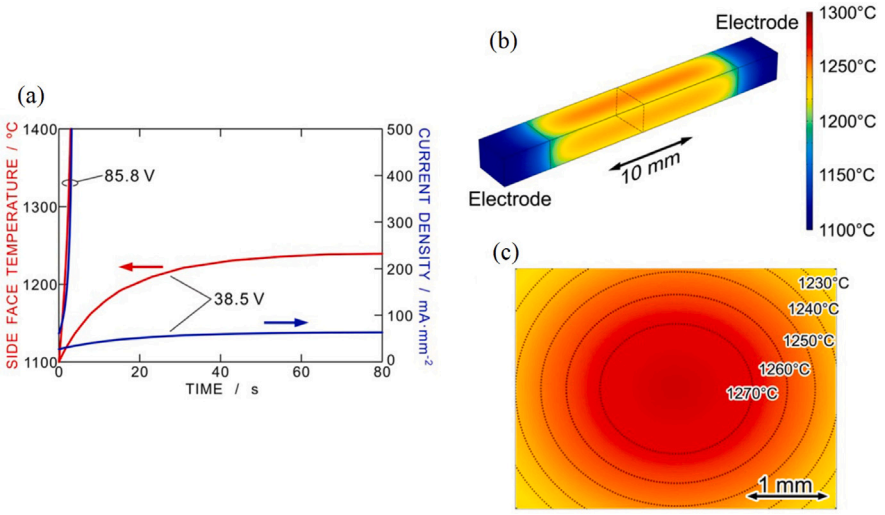


**Fig. 42.** (a) The specimen side temperature and current density with time under various electric field applications of 38.5 and 85.8 V; (b) the overview and (c) the cross-section temperature distributions at 120 s following the application of 38.5 V of electric field. These are the results of the FEM calculation — copied with permission from [185].

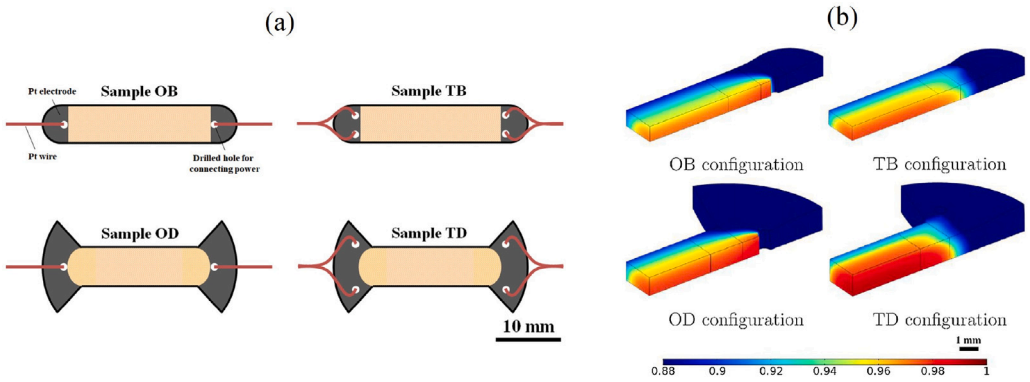


**Fig. 43.** (a) An outline of the four 3YSZ samples that were flash sintered is as follows: There are four samples: Sample OB, which is formed like a bar and has two drilled holes on each end; Sample TB; Sample OD; Sample TD; and Sample OB, which is shaped like a dog bone and has one drilled hole on each end. Pt paste is represented by grey areas, and Pt wire is used to link drilled holes to the power source, (b) Numerical analysis of the relative density distribution in four 3YSZ samples after FS — copied with permission from [171].

the surface and interior of strip-shaped samples. It is important to note that the temperature, density, and particle size distributions within flash-sintered specimens are not homogeneous, indicating the complex nature of the process [172].

Another model accurately replicated the resistivity-temperature behaviour observed in pre-sintered 3YSZ samples, validating the effectiveness of the 4-terminal test configuration for these specimens [171]. The study focuses on four different specimen configurations, namely Original Base (OB), Thin Base (TB), Original Dogbone (OD), and Thin Dogbone (TD) (Fig. 43(a)). By considering symmetry assumptions, the model simplifies the numerical formulation and neglects electrochemical reduction phenomena related to the different electric polarities of the voltage feed. The (TD) specimen showed the highest final average density and a uniform microstructure. The simulations revealed that the electrical heating was concentrated off-centre, primarily along the line connecting the contact points at the top of the holes (Fig. 43(b)). The non-uniform temperature and current density distributions highlighted the influence of specimen size, shape, and current limits on the accuracy of the analysis method [171]. In another simulation of the FS, electrodes were positioned at the top of the holes and covered around 1/6 of the cylindrical surface. The resistivity of the samples reduced when the voltage was increased under constant furnace temperature, increasing electrical loading, voltage control, and current control. This was thought to be the result of the ongoing development of particle contact. With varying specimen sizes, shapes, or current restrictions, the straightforward analytical approach may be less accurate. The reduced cross-sectional area in the specimen centre in Fig. 44 may compensate for the non-uniform temperature and current density [186].

In a study conducted by Serrazina et al. [187], the researchers highlighted the importance of including grain boundaries in the model for accurately describing the formation of a liquid phase during FS of Potassium Sodium Niobate (KNN). The researchers used a FEM to simulate the electric field and current control during the three stages of FS. The model demonstrated that temperature differences in particles the size of microns are not only caused by Joule heating. Rather, to explain liquid phase development at particle interactions, grain boundaries are essential. Previous models had proposed the relevance of compositional changes due to current flow and the production of large temperature gradients during FS. Interestingly, the proposed model contradicted these findings, emphasising the necessity of considering grain boundaries. [176,187]. It considered a linear shrinkage of 4% after stage II and an increase in contact area for edge and vertex contact cases. To simplify the model, heat dissipation from the particles to the surrounding environment was not considered, and the integration time was assumed to be less than that measured experimentally. Grain boundaries were also not included in this simplified model. The simulations also revealed different behaviours for Joule heating distributions in face/edge and face/vertex particle configurations during the three stages of FS. The maximum Joule heating

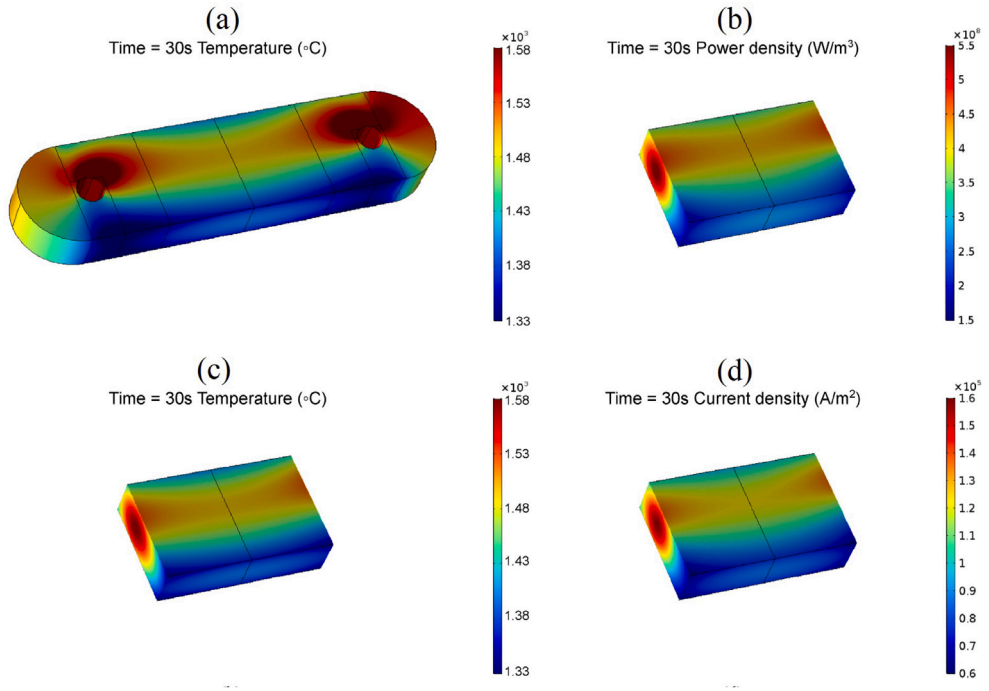


**Fig. 44.** Model distributions for the high current specimen (118 mA $mm^{-2}$) as predicted by the model. (a) The specimen's overall temperature, (b) central section between inner terminals, (c) power density, and (d) current density — copied with permission from [186].

was found to be two orders of magnitude higher in face/face contact compared to face/vertex contact, with higher values typically observed during stage II [179,187]. Moreover, simulations of the monolithic KNN block allowed for a comprehensive analysis of the current density and temperature distribution during FS. The results revealed a distinct spatial temperature dependence within the ceramic, with the core experiencing higher temperatures. This temperature rise in the core was found to be correlated with a decrease in the niobium-oxygen (Nb-O) bond and indicative of a unit cell compression [188].

FS has paved the way for the development of various methods and techniques that leverage its principles to achieve rapid and efficient material processing. Three notable methods derived from FS are flash spark plasma sintering (FSPS), selective laser flash sintering (SLFS), and electric resistance flash sintering (ERFS). SLFS utilises a focused laser beam to selectively sinter specific regions on the surface of a pellet or powder bed. It leverages the localised heating and intense energy provided by the laser to achieve rapid densification in targeted areas. SLFS offers precise control over the sintering process and is particularly useful for complex geometries and fine-feature fabrication [189]. Hagen et al. [190] utilise 2 models for SLFS: Model 1 is a 3D time-dependent model that focuses on determining the temperature distribution in the powder bed due to laser heating — see Fig. 45. The results show that the temperature behind the laser spot decreases over time, reaching 600 K when the laser reaches the second electrode. Model 2 is also a 3D time-dependent model, but it specifically examines the effects of Joule heating on FS. This model analyses the neck radius ratios and their impact on electrical current and temperature changes after the initiation of FS. The simulations demonstrate that the temperature and current density linearly increase after a transient period, with the peak values depending on the initial neck radius ratio. In another study, their focus was on understanding the charge transport mechanisms during stage I of SLFS for 8YSZ [191]. The results indicate that charge transport occurs via a continuous hot path between the two electrodes during the onset of SLFS. The data supported the existence of two concurrent charge transport mechanisms in SLFS of 8YSZ: continuous charge carrier transport and discrete charge carrier transport.

The thermal runaway phenomenon in binder-less tungsten carbide (WC) green bodies was investigated using FEM [192]. The ERFS process was simulated by coupling the equations governing heat generation and transfer with the electric current flow through the WC pellet. The simulation results, as shown in Fig. 46, demonstrated that increasing the interface resistivity allowed for locally high temperatures to initiate the thermal runaway at lower applied voltages. The effectiveness of cylindrical metallic electrodes in maintaining a high current density during FS of metallic ceramics was also explored [192]. Finally, researchers focused on consolidating a nanocomposite Cu–Cr powder using FSPS [193] —- see Fig. 47(a). However, the microstructure of the resulting alloys was found to be nonuniform under the extreme conditions of FSPS. In numerical simulations, heat conduction and electric field equations were utilised to analyse current and temperature distributions within the sample (Fig. 47 (b) and (c)). The simulations revealed disparate current density distributions within the sample, with higher values at the edges and lower values at the centre. The temperature distribution also showed agreement with experimental findings, and the temperature difference between the centre and edges of the sample increased with higher applied electrical power. The simulations suggested that self-diffusion played a dominant role in mass transport during FSPS, but high heating rates could induce partial melting and intensify mass transport.

## 4. Future directions and challenges

The SSB market is still emerging, with current use mainly in low-volume EVs and small portable devices. Most SSBs are polymer-based, with some micro-batteries using oxide-thin film electrolytes. Global SSB production is under 2 GWh, less than 0.5% of LIBs' capacity. However, production is expected to grow significantly by oxide and sulfide electrolyte-based SSBs [5]. As SSBs advance, several new trends and research gaps emerge, which will shape sintering technique development. Future research and development efforts will be guided by these trends and gaps (see Fig. 48). Technological advancements are expected in the sintering field. The use of flash sintering in industrial applications is rare and hot spot problem needs to be mitigated. Cold sintering is the only method that does not involve high heating rates and it has relatively low equipment costs, however not all materials

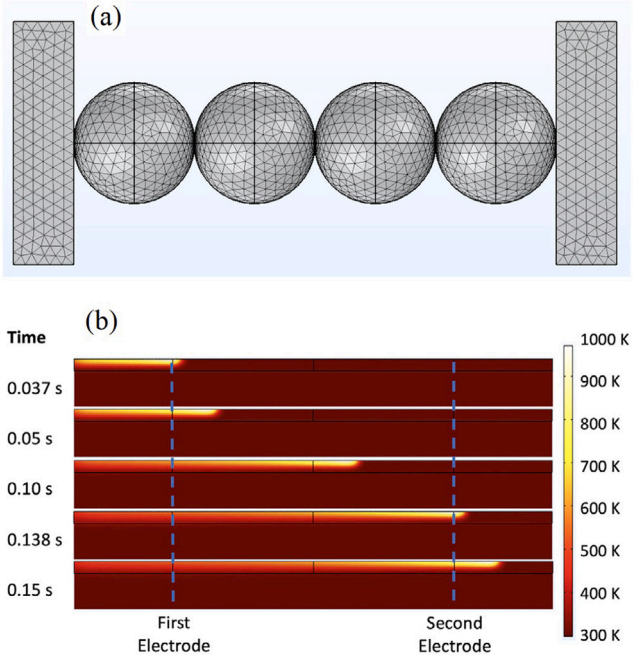


**Fig. 45.** (a) Four spheres of 8% yttria-stabilised zirconia (8-YSZ) are shown in the 3D FEM as being situated between the matching mesh and parallel copper electrodes. (b) Plan view displaying the half-symmetrical laser profile's expected temperature profile from Model 1 on the pellet surface at five different time intervals while scanning at a laser strength of 7.7 W into the pre-sintered pellet at 1100 °C — copied with permission from [190].

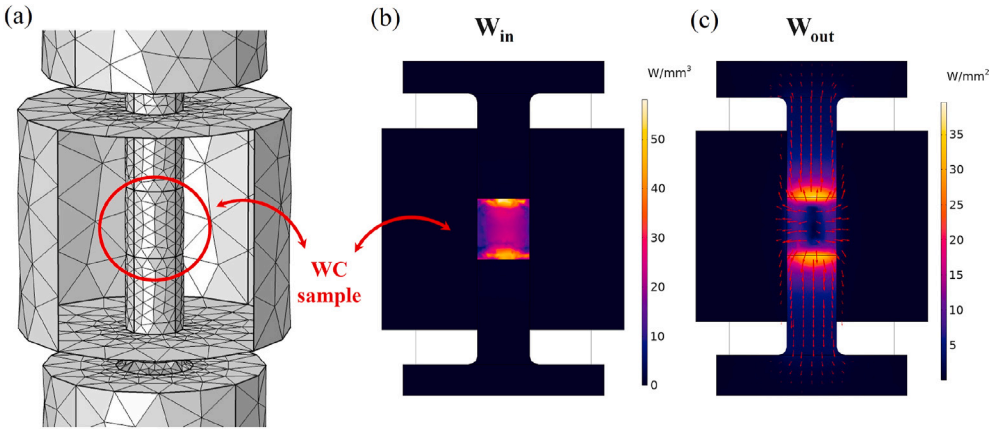


**Fig. 46.** The simulation results at 6.5 V during the flash event (t = 6.8 s) are displayed in detail in the mesh within the zirconia insulating die (a) and its cross sections (b, c). (b) $W_{out}$ = heat losses (conduction, convection, and radiation); (c) $W_{in}$ = heat produced in the WC sample by Joule heating — copied with permission from [192]. (For interpretation of the references to colour in this figure legend, the reader is referred to the web version of this article.)

can be densified using this process. Nevertheless, the major advantage of this method is its potential to achieve exceptionally low sintering temperatures, allowing for material combinations that are otherwise not feasible (e.g., polymer–ceramic) [194]. These New materials and techniques will improve the safety, efficiency, and power of SSBs. Sintering techniques may enable these materials to enhance SSBs' performance and safety. Several other technologies are being used to optimise the sintering process, such as ML and AI. It is possible to predict optimal sintering parameters using AI algorithms, reducing the need for extensive experimentation. However, the transition from laboratory-scale sintering to large-scale industrial production remains challenging. It is necessary to develop cost-effective, efficient methods to scale up sintering techniques without compromising quality. To integrate CSP and FS into industrial-scale SSB production, scalability needs to be addressed [195]. Furthermore, sintered SSB components must be mechanically durable. The long-term mechanical behaviour of sintered materials under demanding operational conditions exists as a research gap.

## 5. Conclusion

In conclusion, sintering techniques have revealed a dynamic landscape of opportunities to advance energy storage technology within SSBs, and since the demand for energy storage solutions is growing, we need new technologies to make batteries more powerful, safer, and less environmentally damaging in the future. We have examined the foundational principles of sintering, particularly cold and flash sintering, documenting the synergies in material processing. A promising solution to densification is CS, which allows heat-sensitive materials to be preserved, and which extends the range of materials that can be processed. While FS poses thermal management and uniformity challenges, it is capable of rapidly densifying materials, which holds considerable promise for accelerating SSB component manufacturing. SSBs can greatly benefit from these sintering techniques. Looking ahead, research directions will include material science advancements to discover materials optimised for sintering techniques. In addition, they

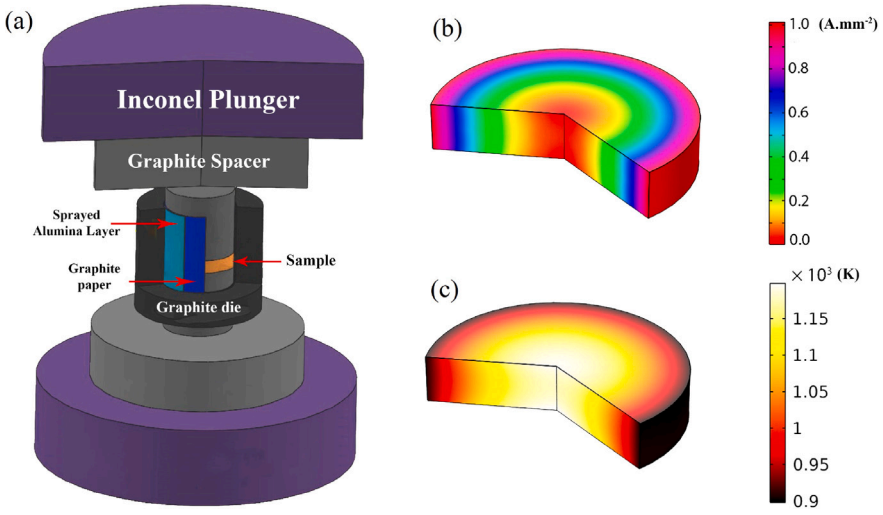


**Fig. 47.** (a) schematic of the FSPS sintering tooling, (b) Distribution of the dimensionless current density, and (c) Temperature distribution (K) at the end of the experiment — copied with permission from [193].

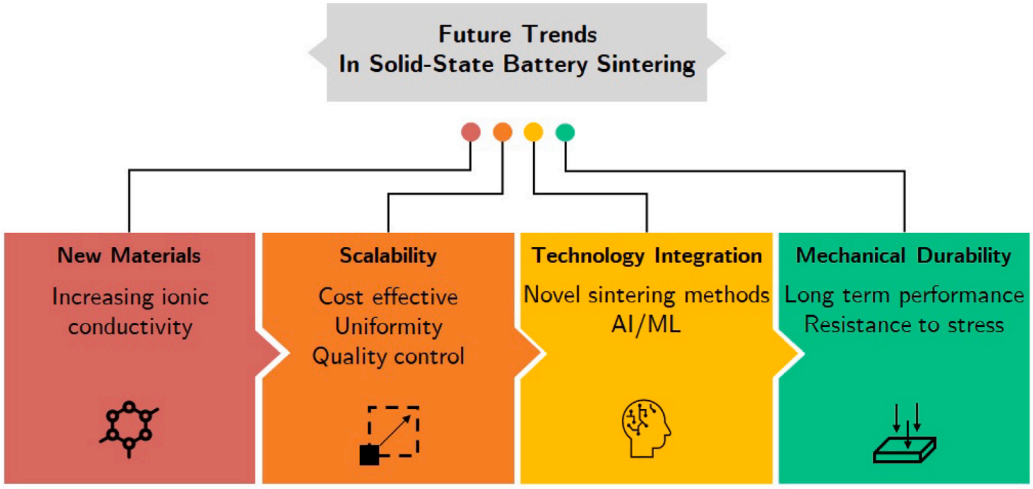


**Fig. 48.** Future trends in SSB sintering.

address the challenge of scaling laboratory sintering to industrial applications efficiently. In conclusion, cold and flash sintering techniques are not only innovative but herald an era in energy storage. They hold the key to an electrified and sustainable future. Researchers collaborate to maximise their potential while embracing emerging trends, ensuring safety, and promoting sustainability.

## CRediT authorship contribution statement

**Amirreza Sazvar:** Writing – review & editing, Writing – original draft, Methodology, Formal analysis, Conceptualization. **Masoumeh Hajibandeh:** Writing – review & editing, Writing – original draft, Methodology, Formal analysis. **Pariya Vafaei:** Writing – review & editing, Writing – original draft, Methodology, Formal analysis. **Elham Hosseinzadeh:** Writing – review & editing, Supervision. **Masoud Jabbari:** Writing – review & editing, Supervision, Conceptualization.

## Declaration of competing interest

The authors declare that they have no known competing financial interests or personal relationships that could have appeared to influence the work reported in this paper.

## Data availability

No data was used for the research described in the article.

## Acknowledgements

For the purpose of open access, the author has applied a Creative Commons Attribution (CC BY) license to any Author Accepted Manuscript version arising from this submission.

## References

[1] C. Bubulinca, N.E. Kazantseva, V. Pechancova, N. Joseph, H. Fei, M. Venher, A. Ivanichenko, P. Saha, Development of all-solid-state li-ion batteries: From key technical areas to commercial use, Batteries 9 (3) (2023) 157.

[2] S. Afyon, K.V. Kravchyk, S. Wang, J. van den Broek, C. Hänsel, M.V. Kovalenko, J.L.M. Rupp, Building better all-solid-state batteries with Li-garnet solid electrolytes and metalloid anodes, J. Mater. Chem. A 7 (2019) 21299–21308, http://dx.doi.org/10.1039/C9TA04999A.

[3] J. Janek, W.G. Zeier, Challenges in speeding up solid-state battery development, Nat. Energy 8 (3) (2023) 230–240.

[4] Q. Zhao, S. Stalin, C.-Z. Zhao, L.A. Archer, Designing solid-state electrolytes for safe, energy-dense batteries, Nat. Rev. Mater. 5 (2020) 229–252, http://dx.doi.org/10.1038/s41578-019-0165-5.

[5] F. Thomas, L. Mahdi, J. Lemaire, D.M. Santos, Technological advances and market developments of solid-state batteries: A review, Materials 17 (1) (2024) 239.

[6] R.K. Bordia, S.J.L. Kang, E.A. Olevsky, Current understanding and future research directions at the onset of the next century of sintering science and technology, J. Am. Ceram. Soc. 100 (2017) 2314–2352, http://dx.doi.org/10.1111/jace.14919.

[7] F. Pinto, R. Silva, F. La Porta, Overview of conventional and unconventional sintering methods, in: Green Sustainable Process for Chemical and Environmental Engineering and Science, Elsevier, 2021, pp. 15–35.

[8] H. Zhu, J. Liu, Emerging applications of spark plasma sintering in all solid-state lithium-ion batteries and beyond, J. Power Sources 391 (2018) 10–25.

[9] J. Nanda, C. Wang, P. Liu, Frontiers of solid-state batteries, MRS Bull. 43 (10) (2018) 740–745.

[10] D.J. Green, O. Guillon, J. Rödel, Constrained sintering: A delicate balance of scales, J. Eur. Ceram. Soc. 28 (7) (2008) 1451–1466.

[11] E.A. Olevsky, Theory of sintering: from discrete to continuum, Mater. Sci. Eng. R Rep. 23 (2) (1998) 41–100.

[12] E.A. Olevsky, V. Tikare, T. Garino, Multi-scale study of sintering: a review, J. Am. Ceram. Soc. 89 (6) (2006) 1914–1922.

[13] V. Tikare, M. Braginsky, E.A. Olevsky, Numerical simulation of solid-state sintering: I, sintering of three particles, J. Am. Ceram. Soc. 86 (1) (2003) 49–53.

[14] A.R. Symington, J. Purton, J. Statham, M. Molinari, M.S. Islam, S.C. Parker, Quantifying the impact of disorder on Li-ion and Na-ion transport in perovskite titanate solid electrolytes for solid-state batteries, J. Mater. Chem. A 8 (37) (2020) 19603–19611.

[15] H. Rahbar, E. Goudeli, M.R. Kholghy, Sintering rate of nickel nanoparticles by molecular dynamics, J. Phys. Chem. C 127 (14) (2023) 6802–6812.

[16] A.C. Rios, E. Olevsky, E. Hryha, M. Persson, R.K. Bordia, Analytical models for initial and intermediate stages of sintering of additively manufactured stainless steel, Acta Mater. 249 (2023) 118822.

[17] L. Benabou, X. Wang, Simulation of silver nanoparticles sintering at high temperatures based on theoretical evaluations of surface and grain boundary mobilities, Int. J. Comput. Methods Eng. Sci. Mech. 21 (6) (2020) 331–342.

[18] H. Shi, D. Giuntini, H. van Dommelen, M.G. Geers, J.J. Remmers, Efficient modelling of ceramic sintering processes: Application to bilayers and membranes, J. Eur. Ceram. Soc. 43 (11) (2023) 4939–4949.

[19] A. Eqbal, K.S. Arya, T. Chakrabarti, In-depth study of the evolving thermal runaway and thermal gradient in the dog bone sample during flash sintering using finite element analysis, Ceram. Int. 46 (8) (2020) 10370–10378.

[20] B. Paredes-Goyes, D. Jauffres, J.-M. Missiaen, C.L. Martin, Grain growth in sintering: A discrete element model on large packings, Acta Mater. 218 (2021) 117182.

[21] M. So, G. Inoue, K. Park, K. Nunoshita, S. Ishikawa, Y. Tsuge, Simulation of the compaction of an all-solid-state battery cathode with coated particles using the discrete element method, J. Power Sources 530 (2022) 231279.

[22] M.H.P. Teixeira, V. Skorych, R. Janssen, S.Y.G. González, A. De Noni Jr., J.B.R. Neto, D. Hotza, M. Dosta, High heating rate sintering and microstructural evolution assessment using the discrete element method, Open Ceram. 8 (2021) 100182.

[23] M. Braginsky, V. Tikare, E. Olevsky, Numerical simulation of solid state sintering, Int. J. Solids Struct. 42 (2) (2005) 621–636.

[24] J. Xu, X. Cai, S. Cai, Y. Shao, C. Hu, S. Lu, S. Ding, High-energy lithium-ion batteries: recent progress and a promising future in applications, Energy Environ. Mater. 6 (5) (2023) e12450.

[25] Y.-Y. Sun, Q. Zhang, L. Yan, T.-B. Wang, P.-Y. Hou, A review of interfaces within solid-state electrolytes: fundamentals, issues and advancements, Chem. Eng. J. 437 (2022) 135179.

[26] R. Chen, Q. Li, X. Yu, L. Chen, H. Li, Approaching practically accessible solid-state batteries: stability issues related to solid electrolytes and interfaces, Chem. Rev. 120 (14) (2019) 6820–6877.

[27] Y. Horowitz, C. Schmidt, D.-h. Yoon, L.M. Riegger, L. Katzenmeier, G.M. Bosch, M. Noked, Y. Ein-Eli, J. Janek, W.G. Zeier, et al., Between liquid and all solid: a prospect on electrolyte future in lithium-ion batteries for electric vehicles, Energy Technol. 8 (11) (2020) 2000580.

[28] C. Li, Z.-y. Wang, Z.-j. He, Y.-j. Li, J. Mao, K.-h. Dai, C. Yan, J.-c. Zheng, An advance review of solid-state battery: Challenges, progress and prospects, Sustain. Mater. Technol. 29 (2021) e00297.

[29] T. Famprikis, P. Canepa, J.A. Dawson, M.S. Islam, C. Masquelier, Fundamentals of inorganic solid-state electrolytes for batteries, Nature Mater. 18 (12) (2019) 1278–1291.

[30] Z. Li, Q. Liu, Y. Deng, M. Zhou, W. Tang, H. Dong, W. Zhao, R. Liu, In situ cross-linked plastic crystal electrolytes toward superior lithium metal batteries, Mater. Today Energy 31 (2023) 101198.

[31] J.G. Kim, B. Son, S. Mukherjee, N. Schuppert, A. Bates, O. Kwon, M.J. Choi, H.Y. Chung, S. Park, A review of lithium and non-lithium based solid state batteries, J. Power Sources 282 (2015) 299–322.

[32] K. Kerman, A. Luntz, V. Viswanathan, Y.-M. Chiang, Z. Chen, Practical challenges hindering the development of solid state Li ion batteries, J. Electrochem. Soc. 164 (7) (2017) A1731.

[33] H. Zhang, B.M. May, F. Omenya, M.S. Whittingham, J. Cabana, G. Zhou, Layered oxide cathodes for Li-ion batteries: oxygen loss and vacancy evolution, Chem. Mater. 31 (18) (2019) 7790–7798.

[34] R. Pacios, A. Villaverde, M. Martínez-Ibañez, M. Casas-Cabanas, F. Aguesse, A. Kvasha, Roadmap for competitive production of solid-state batteries: How to convert a promise into reality, Adv. Energy Mater. 13 (30) (2023) 2301018.

[35] A. Chakraborty, S. Kunnikuruvan, S. Kumar, B. Markovsky, D. Aurbach, M. Dixit, D.T. Major, Layered cathode materials for lithium-ion batteries: review of computational studies on LiNi1–x–y Co x Mn y O2 and LiNi1–x–y Co x Al y O2, Chem. Mater. 32 (3) (2020) 915–952.

[36] M.M. Thackeray, K. Amine, Layered Li–Ni–Mn–Co oxide cathodes, Nat. Energy 6 (9) (2021) 933.

[37] S. Zhang, X. Zhou, S. Li, Z. Feng, X. Fan, D. Sun, H. Wang, Y. Tang, Construction of a nickel-rich $LiNi_{0.83}Co_{0.11}Mn_{0.06}O_2$ cathode with high stability and excellent cycle performance through interface engineering, Mater. Chem. Front. 7 (3) (2023) 490–501.

[38] Z. Tan, X. Chen, Y. Li, X. Xi, S. Hao, X. Li, X. Shen, Z. He, W. Zhao, Y. Yang, Enabling superior cycling stability of $LiNi_{0.9}Co_{0.05}Mn_{0.05}O_2$ with controllable internal strain, Adv. Funct. Mater. (2023) 2215123.

[39] M. Tebyetekerwa, T.T. Duignan, Z. Xu, X. Song Zhao, Rechargeable dual-carbon batteries: a sustainable battery technology, Adv. Energy Mater. 12 (44) (2022) 2202450.

[40] H. Zhang, Y. Yang, D. Ren, L. Wang, X. He, Graphite as anode materials: Fundamental mechanism, recent progress and advances, Energy Storage Mater. 36 (2021) 147–170.

[41] H. Yan, D. Zhang, X. Duo, X. Sheng, et al., A review of spinel lithium titanate (Li4Ti5O12) as electrode material for advanced energy storage devices, Ceram. Int. 47 (5) (2021) 5870–5895.

[42] D.K. Singh, T. Fuchs, C. Krempaszky, B. Mogwitz, S. Burkhardt, F.H. Richter, J. Janek, Overcoming anode instability in solid-state batteries through control of the lithium metal microstructure, Adv. Funct. Mater. 33 (1) (2023) 2211067.

[43] M. Feng, C.-T. Yang, Y. Qi, The critical stack pressure to alter void generation at Li/solid-electrolyte interfaces during stripping, J. Electrochem. Soc. 169 (9) (2022) 090526.

[44] X. Gu, J. Dong, C. Lai, Li-containing alloys beneficial for stabilizing lithium anode: A review, Eng. Rep. 3 (1) (2021) e12339.

[45] J.A. Lewis, K.A. Cavallaro, Y. Liu, M.T. McDowell, The promise of alloy anodes for solid-state batteries, Joule 6 (7) (2022) 1418–1430.

[46] T. Fuchs, J. Becker, C.G. Haslam, C. Lerch, J. Sakamoto, F.H. Richter, J. Janek, Current-dependent lithium metal growth modes in "Anode-Free" solid-state batteries at the Cu | LLZO interface, Adv. Energy Mater. 13 (1) (2023) 2203174.

[47] L. Qian, Y. Zheng, T. Or, H.W. Park, R. Gao, M. Park, Q. Ma, D. Luo, A. Yu, Z. Chen, Advanced material engineering to tailor nucleation and growth towards uniform deposition for anode-less lithium metal batteries, Small 18 (50) (2022) 2205233.

[48] J. Oh, S.H. Choi, J.Y. Kim, J. Lee, T. Lee, N. Lee, T. Lee, Y. Sohn, W.J. Chung, K.Y. Bae, et al., Anode-less all-solid-state batteries operating at room temperature and low pressure, Adv. Energy Mater. 13 (38) (2023) 2301508.

[49] T.T. Vu, H.J. Cheon, S.Y. Shin, G. Jeong, E. Wi, M. Chang, Hybrid electrolytes for solid-state lithium batteries: Challenges, progress, and prospects, Energy Storage Mater. (2023) 102876.

[50] M. Keller, A. Varzi, S. Passerini, Hybrid electrolytes for lithium metal batteries, J. Power Sources 392 (2018) 206–225.

[51] P. Jiang, G. Du, J. Cao, X. Zhang, C. Zou, Y. Liu, X. Lu, Solid-state li ion batteries with oxide solid electrolytes: Progress and perspective, Energy Technol. 11 (3) (2023) 2201288.

[52] R. Kali, A. Mukhopadhyay, Spark plasma sintered/synthesized dense and nanostructured materials for solid-state Li-ion batteries: Overview and perspective, J. Power Sources 247 (2014) 920–931.

[53] H. Kwak, J.-S. Kim, D. Han, J.S. Kim, J. Park, G. Kwon, S.-M. Bak, U. Heo, C. Park, H.-W. Lee, et al., Boosting the interfacial superionic conduction of halide solid electrolytes for all-solid-state batteries, Nat. Commun. 14 (1) (2023) 2459.

[54] K. Nagao, M. Nose, A. Kato, A. Sakuda, A. Hayashi, M. Tatsumisago, Preparation and characterization of glass solid electrolytes in the pseudoternary system Li3BO3-Li2SO4-Li2CO3, Solid State Ion. 308 (2017) 68–76.

[55] H. Zhu, J. Liu, Emerging applications of spark plasma sintering in all solid-state lithium-ion batteries and beyond, J. Power Sources 391 (2018) 10–25, URL https://www.sciencedirect.com/science/article/pii/S0378775318303975.

[56] M. Abedi, S. Sovizi, A. Azarniya, D. Giuntini, M.E. Seraji, H.R.M. Hosseini, C. Amutha, S. Ramakrishna, A. Mukasyan, An analytical review on Spark Plasma Sintering of metals and alloys: From processing window, phase transformation, and property perspective, Crit. Rev. Solid State Mater. Sci. 48 (2) (2023) 169–214.

[57] H. Yang, N. Wu, Ionic conductivity and ion transport mechanisms of solid-state lithium-ion battery electrolytes: A review, Energy Sci. Eng. 10 (5) (2022) 1643–1671.

[58] Y. Liu, J. Liu, Q. Sun, D. Wang, K.R. Adair, J. Liang, C. Zhang, L. Zhang, S. Lu, H. Huang, X. Song, X. Sun, Insight into the microstructure and ionic conductivity of cold sintered NASICON solid electrolyte for solid-state batteries, ACS Appl. Mater. Interfaces 11 (31) (2019) 27890–27896, http://dx.doi.org/10.1021/acsami.9b08132, PMID: 31298519.

[59] M. Jia, M. Khurram Tufail, X. Guo, Insight into the key factors in high Li+ transference number composite electrolytes for solid lithium batteries, ChemSusChem 16 (2) (2023) e202201801.
[60] C. Monroe, J. Newman, Dendrite growth in lithium/polymer systems: A propagation model for liquid electrolytes under galvanostatic conditions, J. Electrochem. Soc. 150 (10) (2003) A1377.
[61] M. Golmohammad, A. Sazvar, M.M. Shahraki, M. Salimi, Effects of Nd and Al co-doping on the microstructure and lithium-ion transport in Li7La3Zr2O12 solid-state batteries, Solid State Ion. 412 (2024) 116598.
[62] B. Zhang, R. Tan, L. Yang, J. Zheng, K. Zhang, S. Mo, Z. Lin, F. Pan, Mechanisms and properties of ion-transport in inorganic solid electrolytes, Energy Storage Mater. 10 (2018) 139–159.
[63] X. Li, J.T. Kim, J. Luo, C. Zhao, Y. Xu, T. Mei, R. Li, J. Liang, X. Sun, Structural regulation of halide superionic conductors for all-solid-state lithium batteries, Nature Commun. 15 (1) (2024) 53.
[64] M. Ma, M. Zhang, B. Jiang, Y. Du, B. Hu, C. Sun, A review of all-solid-state electrolytes for lithium batteries: high-voltage cathode materials, solid-state electrolytes and electrode–electrolyte interfaces, Mater. Chem. Front. 7 (2023) 1268–1297.
[65] K.V. Kravchyk, H. Zhang, F. Okur, M.V. Kovalenko, Li–garnet solid-state batteries with LLZO scaffolds, Acc. Mater. Res. 3 (4) (2022) 411–415, http://dx.doi.org/10.1021/accountsmr.2c00004.
[66] K.V. Kravchyk, D.T. Karabay, M.V. Kovalenko, On the feasibility of all-solid-state batteries with LLZO as a single electrolyte, Sci. Rep. 12 (1) (2022) 1177.
[67] Y. Nikodimos, W.-N. Su, B.J. Hwang, Halide solid-state electrolytes: stability and application for high voltage all-solid-state Li batteries, Adv. Energy Mater. 13 (3) (2023) 2202854.
[68] K.T. Kim, J. Woo, Y.-S. Kim, S. Sung, C. Park, C. Lee, Y.J. Park, H.-W. Lee, K. Park, Y.S. Jung, Ultrathin superhydrophobic coatings for air-stable inorganic solid electrolytes: Toward dry room application for all-solid-state batteries, Adv. Energy Mater. (2023) 2301600.
[69] P. Ganesan, M. Soans, M.A. Cambaz, R. Zimmermanns, R. Gond, S. Fuchs, Y. Hu, S. Baumgart, M. Sotoudeh, D. Stepien, et al., Fluorine-substituted halide solid electrolytes with enhanced stability toward the lithium metal, ACS Appl. Mater. Interfaces 15 (32) (2023) 38391–38402.
[70] T. Yu, J. Liang, L. Luo, L. Wang, F. Zhao, G. Xu, X. Bai, R. Yang, S. Zhao, J. Wang, et al., Superionic fluorinated halide solid electrolytes for highly stable Li-metal in all-solid-state Li batteries, Adv. Energy Mater. 11 (36) (2021) 2101915.
[71] M. Wang, J. Sakamoto, Correlating the interface resistance and surface adhesion of the Li metal-solid electrolyte interface, J. Power Sources 377 (2018) 7–11.
[72] L. Zhang, Y. Liu, Y. You, A. Vinu, L. Mai, NASICONs-type solid-state electrolytes: The history, physicochemical properties, and challenges, Interdiscip. Mater. 2 (1) (2023) 91–110.
[73] H. Raj, T. Fabre, M. Lachal, A. Neveu, J. Jean, M.C. Steil, R. Bouchet, V. Pralong, Stabilizing the NASICON solid electrolyte in an inert atmosphere as a function of physical properties and sintering conditions for solid-state battery fabrication, ACS Appl. Energy Mater. 6 (3) (2023) 1197–1207.
[74] Y. Pang, J. Pan, J. Yang, S. Zheng, C. Wang, Electrolyte/electrode interfaces in all-solid-state lithium batteries: a review, Electrochem. Energy Rev. 4 (2021) 169–193.
[75] M. Clausnitzer, M. Ihrig, L. Cressa, S. Hein, M. Finsterbusch, S. Eswara, L.-Y. Kuo, T. Danner, P. Kaghazchi, D. Fattakhova-Rohlfing, et al., Impact of degradation mechanisms at the cathode/electrolyte interface of garnet-based all-solid-state batteries, Energy Storage Mater. (2024) 103262.
[76] T. Demuth, T. Fuchs, F. Walther, A. Pokle, S. Ahmed, M. Malaki, A. Beyer, J. Janek, K. Volz, Influence of the sintering temperature on LLZO-NCM cathode composites for solid-state batteries studied by transmission electron microscopy, Matter 6 (7) (2023) 2324–2339.
[77] Y. Kim, I. Waluyo, A. Hunt, B. Yildiz, Avoiding CO2 improves thermal stability at the Interface of Li7La3Zr2O12 electrolyte with layered oxide cathodes, Adv. Energy Mater. 12 (13) (2022) 2102741.
[78] S. Hong, S.H. Song, M. Cho, S. Kim, S.-H. Yu, D. Lee, H. Kim, Structural and chemical compatibilities of Li1- xNi0. 5Co0. 2Mn0. 3O2 cathode material with garnet-type solid electrolyte for all-solid-state batteries, Small 17 (46) (2021) 2103306.
[79] M. Malaki, A. Pokle, S.-K. Otto, A. Henss, J.P. Beaupain, A. Beyer, J. Müller, B. Butz, K. Wätzig, M. Kusnezoff, et al., Advanced analytical characterization of interface degradation in Ni-rich NCM cathode co-sintered with LATP solid electrolyte, ACS Appl. Energy Mater. 5 (4) (2022) 4651–4663.
[80] C. Rosenbach, F. Walther, J. Ruhl, M. Hartmann, T.A. Hendriks, S. Ohno, J. Janek, W.G. Zeier, Visualizing the chemical incompatibility of halide and sulfide-based electrolytes in solid-state batteries, Adv. Energy Mater. 13 (6) (2023) 2203673.
[81] J. Zhang, X. Yao, R.K. Misra, Q. Cai, Y. Zhao, Progress in electrolytes for beyond-lithium-ion batteries, J. Mater. Sci. Technol. 44 (2020) 237–257.
[82] X. Yao, E. Olsson, M. Wang, J. Wang, Q. Cai, N. Peng, R. Webb, Y. Zhao, Xenon ion implantation induced surface compressive stress for preventing dendrite penetration in solid-state electrolytes, Small 18 (23) (2022) 2108124.
[83] C. Yuan, B.W. Sheldon, J. Xu, Heterogeneous reinforcements to mitigate Li penetration through solid electrolytes in all-solid-state batteries, Adv. Energy Mater. 12 (39) (2022) 2201804.
[84] H. Duan, C. Wang, R. Yu, W. Li, J. Fu, X. Yang, X. Lin, M. Zheng, X. Li, S. Deng, et al., In situ constructed 3D lithium anodes for long-cycling all-solid-state batteries, Adv. Energy Mater. (2023) 2300815.
[85] W. Xia, B. Xu, H. Duan, Y. Guo, H. Kang, H. Li, H. Liu, Ionic conductivity and air stability of Al-doped Li7La3Zr2O12 sintered in alumina and Pt crucibles, ACS Appl. Mater. Interfaces 8 (8) (2016) 5335–5342.
[86] Z. Ning, G. Li, D.L. Melvin, Y. Chen, J. Bu, D. Spencer-Jolly, J. Liu, B. Hu, X. Gao, J. Perera, et al., Dendrite initiation and propagation in lithium metal solid-state batteries, Nature 618 (7964) (2023) 287–293.
[87] X. Su, K. Guo, T. Ma, P.A. Tamirisa, H. Ye, H. Gao, B.W. Sheldon, Deformation and chemomechanical degradation at solid electrolyte–electrode interfaces, ACS Energy Lett. 2 (8) (2017) 1729–1733.
[88] B.S. Vishnugopi, K.G. Naik, H. Kawakami, N. Ikeda, Y. Mizuno, R. Iwamura, T. Kotaka, K. Aotani, Y. Tabuchi, P.P. Mukherjee, Asymmetric contact loss dynamics during plating and stripping in solid-state batteries, Adv. Energy Mater. 13 (8) (2023) 2203671.
[89] D. Spencer Jolly, Z. Ning, G.O. Hartley, B. Liu, D.L. Melvin, P. Adamson, J. Marrow, P.G. Bruce, Temperature dependence of lithium anode voiding in argyrodite solid-state batteries, ACS Appl. Mater. Interfaces 13 (19) (2021) 22708–22716.
[90] Q. Li, T. Yi, X. Wang, H. Pan, B. Quan, T. Liang, X. Guo, X. Yu, H. Wang, X. Huang, et al., In-situ visualization of lithium plating in all-solid-state lithium-metal battery, Nano Energy 63 (2019) 103895.
[91] L. Zhou, N. Minafra, W.G. Zeier, L.F. Nazar, Innovative approaches to Li-argyrodite solid electrolytes for all-solid-state lithium batteries, Acc. Chem. Res. 54 (12) (2021) 2717–2728.
[92] C.F. Marchiori, R.P. Carvalho, M. Ebadi, D. Brandell, C.M. Araujo, Understanding the electrochemical stability window of polymer electrolytes in solid-state batteries from atomic-scale modeling: the role of Li-ion salts, Chem. Mater. 32 (17) (2020) 7237–7246.
[93] P. Vadhva, A.M. Boyce, A. Hales, M.-C. Pang, A.N. Patel, P.R. Shearing, G. Offer, A.J. Rettie, Towards optimised cell design of thin film silicon-based solid-state batteries via modelling and experimental characterisation, J. Electrochem. Soc. 169 (10) (2022) 100525.
[94] L. Raijmakers, D. Danilov, R.-A. Eichel, P. Notten, An advanced all-solid-state Li-ion battery model, Electrochim. Acta 330 (2020) 135147.
[95] L. Sultanova, Ł. Figiel, Microscale diffusion-mechanics model for a polymer-based solid-state battery cathode, Comput. Mater. Sci. 186 (2021) 109990.
[96] G. Bucci, T. Swamy, Y.-M. Chiang, W.C. Carter, Modeling of internal mechanical failure of all-solid-state batteries during electrochemical cycling, and implications for battery design, J. Mater. Chem. A 5 (36) (2017) 19422–19430.
[97] D. Diddens, W.A. Appiah, Y. Mabrouk, A. Heuer, T. Vegge, A. Bhowmik, Modeling the solid electrolyte interphase: Machine learning as a game changer? Adv. Mater. Interfaces 9 (8) (2022) 2101734.
[98] E.W.C. Spotte-Smith, S.M. Blau, X. Xie, H.D. Patel, M. Wen, B. Wood, S. Dwaraknath, K.A. Persson, Quantum chemical calculations of lithium-ion battery electrolyte and interphase species, Sci. Data 8 (1) (2021) 203.
[99] M. Bin Jassar, C. Michel, S. Abada, T. De Bruin, S. Tant, C. Nieto-Draghi, S.N. Steinmann, A perspective on the molecular modeling of electrolyte decomposition reactions for solid electrolyte interphase growth in lithium-ion batteries, Adv. Funct. Mater. (2024) 2313188.
[100] L.J. Miara, W.D. Richards, Y.E. Wang, G. Ceder, First-principles studies on cation dopants and electrolyte— cathode interphases for lithium garnets, Chem. Mater. 27 (11) (2015) 4040–4047.
[101] T. Cheng, B.V. Merinov, S. Morozov, W.A. Goddard III, Quantum mechanics reactive dynamics study of solid Li-electrode/Li6PS5Cl-electrolyte interface, ACS Energy Lett. 2 (6) (2017) 1454–1459.
[102] H. Liu, S. Ma, J. Wu, Y. Wang, X. Wang, Recent advances in screening lithium solid-state electrolytes through machine learning, Front. Energy Res. 9 (2021) 639741.
[103] E. Choi, J. Jo, W. Kim, K. Min, Searching for mechanically superior solid-state electrolytes in Li-Ion batteries via data-driven approaches, ACS Appl. Mater. Interfaces 13 (36) (2021) 42590–42597.
[104] Y.-T. Chen, M. Duquesnoy, D.H. Tan, J.-M. Doux, H. Yang, G. Deysher, P. Ridley, A.A. Franco, Y.S. Meng, Z. Chen, Fabrication of high-quality thin solid-state electrolyte films assisted by machine learning, ACS Energy Lett. 6 (4) (2021) 1639–1648.
[105] K. Fujimura, A. Seko, Y. Koyama, A. Kuwabara, I. Kishida, K. Shitara, C.A. Fisher, H. Moriwake, I. Tanaka, Accelerated materials design of lithium superionic conductors based on first-principles calculations and machine learning algorithms, Adv. Energy Mater. 3 (8) (2013) 980–985.
[106] E.D. Cubuk, A.D. Sendek, E.J. Reed, Screening billions of candidates for solid lithium-ion conductors: A transfer learning approach for small data, J. Chem. Phys. 150 (21) (2019).
[107] Z. Ahmad, T. Xie, C. Maheshwari, J.C. Grossman, V. Viswanathan, Machine learning enabled computational screening of inorganic solid electrolytes for suppression of dendrite formation in lithium metal anodes, ACS Cent. Sci. 4 (8) (2018) 996–1006.

[108] D. Cheng, W. Sha, L. Wang, S. Tang, A. Ma, Y. Chen, H. Wang, P. Lou, S. Lu, Y.-C. Cao, Solid-state lithium battery cycle life prediction using machine learning, Appl. Sci. 11 (10) (2021) 4671.
[109] R. Wang, Q. Dong, C. Wang, M. Hong, J. Gao, H. Xie, M. Guo, W. Ping, X. Wang, S. He, et al., High-temperature ultrafast sintering: exploiting a new kinetic region to fabricate porous solid-state electrolyte scaffolds, Adv. Mater. 33 (34) (2021) 2100726.
[110] Z. Sun, M. Liu, Y. Zhu, R. Xu, Z. Chen, P. Zhang, Z. Lu, P. Wang, C. Wang, Issues concerning interfaces with inorganic solid electrolytes in all-solid-state lithium metal batteries, Sustainability 14 (15) (2022) 9090.
[111] K. Lu, Sintering of nanoceramics, Int. Mater. Rev. 53 (1) (2008) 21–38.
[112] R.K. Bordia, S.-J.L. Kang, E.A. Olevsky, Current understanding and future research directions at the onset of the next century of sintering science and technology, J. Am. Ceram. Soc. 100 (6) (2017) 2314–2352.
[113] X. Liu, A. Martín-Calvo, E. McGarrity, S.K. Schnell, S. Calero, J.-M. Simon, D. Bedeaux, S. Kjelstrup, A. Bardow, T.J. Vlugt, Fick diffusion coefficients in ternary liquid systems from equilibrium molecular dynamics simulations, Ind. Eng. Chem. Res. 51 (30) (2012) 10247–10258.
[114] B.P. Van Milligen, P. Bons, B.A. Carreras, R. Sanchez, On the applicability of Fick's law to diffusion in inhomogeneous systems, Eur. J. Phys. 26 (5) (2005) 913.
[115] R.H. Castro, D. Gouvêa, Sintering and nanostability: the thermodynamic perspective, J. Am. Ceram. Soc. 99 (4) (2016) 1105–1121.
[116] J. Guo, R. Floyd, S. Lowum, J.-P. Maria, T. Herisson de Beauvoir, J.-H. Seo, C.A. Randall, Cold sintering: progress, challenges, and future opportunities, Annu. Rev. Mater. Res. 49 (2019) 275–295.
[117] S. Grasso, M. Biesuz, L. Zoli, G. Taveri, A.I. Duff, D. Ke, A. Jiang, M.J. Reece, A review of cold sintering processes, Adv. Appl. Ceram. 119 (3) (2020) 115–143.
[118] T. Yu, J. Cheng, L. Li, B. Sun, X. Bao, H. Zhang, Current understanding and applications of the cold sintering process, Front. Chem. Sci. Eng. 13 (2019) 654–664.
[119] H. Usui, Y. Domi, S.-i. Izaki, A. Nasu, A. Sakuda, A. Hayashi, H. Sakaguchi, Room-temperature preparation of all-solid-state lithium batteries using TiO2 anodes and oxide electrolytes, J. Phys. Chem. C 126 (25) (2022) 10320–10326.
[120] M. Biesuz, V.M. Sglavo, Flash sintering of ceramics, J. Eur. Ceram. Soc. 39 (2–3) (2019) 115–143.
[121] M. Yu, S. Grasso, R. Mckinnon, T. Saunders, M.J. Reece, Review of flash sintering: materials, mechanisms and modelling, Adv. Appl. Ceram. 116 (1) (2017) 24–60.
[122] R. Raj, A. Kulkarni, J.-M. Lebrun, S. Jha, Flash sintering: A new frontier in defect physics and materials science, MRS Bull. 46 (2021) 36–43.
[123] J.S. Francis, R. Raj, Influence of the field and the current limit on flash sintering at isothermal furnace temperatures, J. Am. Ceram. Soc. 96 (9) (2013) 2754–2758.
[124] R. Todd, E. Zapata-Solvas, R. Bonilla, T. Sneddon, P. Wilshaw, Electrical characteristics of flash sintering: thermal runaway of Joule heating, J. Eur. Ceram. Soc. 35 (6) (2015) 1865–1877.
[125] J.G.P. da Silva, M. Bram, A.M. Laptev, J. Gonzalez-Julian, Q. Ma, F. Tietz, O. Guillon, Sintering of a sodium-based NASICON electrolyte: A comparative study between cold, field assisted and conventional sintering methods, J. Eur. Ceram. Soc. 39 (8) (2019) 2697–2702.
[126] G. Yan, S. Yu, J.F. Nonemacher, H. Tempel, H. Kungl, J. Malzbender, R.-A. Eichel, M. Krüger, Influence of sintering temperature on conductivity and mechanical behavior of the solid electrolyte LATP, Ceram. Int. 45 (12) (2019) 14697–14703.
[127] Y. Liu, Q. Sun, D. Wang, K. Adair, J. Liang, X. Sun, Development of the cold sintering process and its application in solid-state lithium batteries, J. Power Sources 393 (2018) 193–203.
[128] H. Geng, A. Mei, Y. Lin, C. Nan, Effect of sintering atmosphere on ionic conduction and structure of Li0. 5La0. 5TiO3 solid electrolytes, Mater. Sci. Eng. B 164 (2) (2009) 91–95.
[129] C. Schwab, G. Häuschen, M. Mann, C. Roitzheim, O. Guillon, D. Fattakhova-Rohlfing, M. Finsterbusch, Towards economic processing of high performance garnets–case study on zero Li excess Ga-substituted LLZO, J. Mater. Chem. A 11 (11) (2023) 5670–5680.
[130] T. Park, S. Lee, D.-M. Kim, Low-temperature manufacture of cubic-phase Li7La3Zr2O12 electrolyte for all-solid-state batteries by bed powder, Crystals 14 (3) (2024) 271.
[131] X. Huang, Y. Lu, H. Guo, Z. Song, T. Xiu, M.E. Badding, Z. Wen, None-mother-powder method to prepare dense Li-garnet solid electrolytes with high critical current density, ACS Appl. Energy Mater. 1 (10) (2018) 5355–5365.
[132] X. Huang, Y. Lu, Z. Song, K. Rui, Q. Wang, T. Xiu, M.E. Badding, Z. Wen, Manipulating Li2O atmosphere for sintering dense Li7La3Zr2O12 solid electrolyte, Energy Storage Mater. 22 (2019) 207–217.
[133] A.M. Laptev, H. Zheng, M. Bram, M. Finsterbusch, O. Guillon, High-pressure field assisted sintering of half-cell for all-solid-state battery, Mater. Lett. 247 (2019) 155–158.
[134] H.-Y. Li, B. Huang, Z. Huang, C.-A. Wang, Enhanced mechanical strength and ionic conductivity of LLZO solid electrolytes by oscillatory pressure sintering, Ceram. Int. 45 (14) (2019) 18115–18118.
[135] S. Valiyaveettil-SobhanRaj, P. Głuchowski, P. López-Aranguren, F. Aguesse, R. Sampathkumar, T. Thompson, C. Rojviriya, W. Manalastas Jr., M. Srinivasan, M. Casas-Cabanas, High-pressure low-temperature densification of NASICON-based LATP electrolytes for solid-state lithium batteries, Materialia 33 (2024) 101999.
[136] G. Accardo, A. Orue, D. Chatzogiannakis, P. Gluchowski, M. Casas-Cabanas, P. López-Aranguren, Fast and low-temperature densification of highly conductive Li7La3Zr2O12 ceramic electrolytes for solid-state batteries, J. Power Sources 585 (2023) 233632.
[137] M. Ihrig, M. Finsterbusch, C.-L. Tsai, A.M. Laptev, C.-h. Tu, M. Bram, Y.J. Sohn, R. Ye, S. Sevinc, S.-k. Lin, et al., Low temperature sintering of fully inorganic all-solid-state batteries–Impact of interfaces on full cell performance, J. Power Sources 482 (2021) 228905.
[138] Y. Wang, X. Guo, Z. Lin, Y. Yang, L. Wu, H. Liu, H. Yu, Dense sphene-type solid electrolyte through rapid sintering for solid-state lithium metal battery, Chem. Res. Chin. Univ. 36 (2020) 439–446.
[139] A. Sazvar, H. Sarpoolaky, M. Golmohammad, Enhanced densification and ionic conductivity of LLZO by flash sintering, Adv. Appl. Ceram. (2023) 1–11.
[140] H. Zhou, X. Li, Y. Zhu, J. Liu, A. Wu, G. Ma, X. Wang, Z. Jia, L. Wang, Review of flash sintering with strong electric field, High Volt. 7 (1) (2022) 1–11.
[141] A. Galotta, V.M. Sglavo, The cold sintering process: A review on processing features, densification mechanisms and perspectives, J. Eur. Ceram. Soc. 41 (16) (2021) 1–17.
[142] H. Guo, A. Baker, J. Guo, C.A. Randall, Protocol for ultralow-temperature ceramic sintering: an integration of nanotechnology and the cold sintering process, ACS Nano 10 (11) (2016) 10606–10614.
[143] M. Biesuz, G. Taveri, A.I. Duff, E. Olevsky, D. Zhu, C. Hu, S. Grasso, A theoretical analysis of cold sintering, Adv. Appl. Ceram. 119 (2) (2020) 75–89.
[144] W. Lee, C.K. Lyon, J.-H. Seo, R. Lopez-Hallman, Y. Leng, C.-Y. Wang, M.A. Hickner, C.A. Randall, E.D. Gomez, Ceramic–salt composite electrolytes from cold sintering, Adv. Funct. Mater. 29 (20) (2019) 1807872.
[145] J.-H. Seo, Z. Fan, H. Nakaya, R. Rajagopalan, E.D. Gomez, M. Iwasaki, C.A. Randall, Cold sintering, enabling a route to co-sinter an all-solid-state lithium-ion battery, Japan. J. Appl. Phys. 60 (3) (2021) 037001.
[146] B. He, S. Kang, X. Zhao, J. Zhang, X. Wang, Y. Yang, L. Yang, R. Liao, Cold sintering of Li6. 4La3Zr1. 4Ta0. 6O12/PEO composite solid electrolytes, Molecules 27 (19) (2022) 6756.
[147] L. Li, J. Andrews, R. Mitchell, D. Button, D.C. Sinclair, I.M. Reaney, Aqueous cold sintering of Li-based compounds, ACS Appl. Mater. Interfaces 15 (16) (2023) 20228–20239.
[148] J.-H. Seo, K. Verlinde, J. Guo, D.S.B. Heidary, R. Rajagopalan, T.E. Mallouk, C.A. Randall, Cold sintering approach to fabrication of high rate performance binderless LiFePO4 cathode with high volumetric capacity, Scr. Mater. 146 (2018) 267–271.
[149] J.-H. Seo, J. Guo, H. Guo, K. Verlinde, D.S.B. Heidary, R. Rajagopalan, C.A. Randall, Cold sintering of a Li-ion cathode: LiFePO4-composite with high volumetric capacity, Ceram. Int. 43 (17) (2017) 15370–15374.
[150] J.-H. Seo, K. Verlinde, R. Rajagopalan, E.D. Gomez, T.E. Mallouk, C.A. Randall, Cold sintering process for fabrication of a high volumetric capacity Li4Ti5O12 anode, Mater. Sci. Eng. B 250 (2019) 114435.
[151] S.S. Berbano, J. Guo, H. Guo, M.T. Lanagan, C.A. Randall, Cold sintering process of Li1. 5Al0. 5Ge1. 5 (PO4) 3 solid electrolyte, J. Am. Ceram. Soc. 100 (5) (2017) 2123–2135.
[152] H. Leng, J. Huang, J. Nie, J. Luo, Cold sintering and ionic conductivities of Na3. 256Mg0. 128Zr1. 872Si2PO12 solid electrolytes, J. Power Sources 391 (2018) 170–179.
[153] D.S.B. Heidary, J. Guo, J.-H. Seo, H. Guo, R. Rajagopalan, C.A. Randall, Microstructures and electrical properties of V2O5 and carbon-nanofiber composites fabricated by cold sintering process, Japan. J. Appl. Phys. 57 (2) (2018) 025702.
[154] J. Guo, H. Guo, A.L. Baker, M.T. Lanagan, E.R. Kupp, G.L. Messing, C.A. Randall, Cold sintering: a paradigm shift for processing and integration of ceramics, Angew. Chem. 128 (38) (2016) 11629–11633.
[155] K. Vikrant, X. Phuah, J. Lund, H. Wang, C. Hellberg, N. Bernstein, W. Rheinheimer, C. Bishop, H. Wang, R. García, Modeling of flash sintering of ionic ceramics, MRS Bull. 46 (2021) 67–75.
[156] Y. Dong, I.-W. Chen, Predicting the onset of flash sintering, J. Am. Ceram. Soc. 98 (8) (2015) 2333–2335.
[157] M. Lachal, H. El Khal, D. Bouvard, J.-M. Chaix, R. Bouchet, M.C. Steil, Flash sintering of cationic conductive ceramics: A way to build multilayer systems, J. Am. Ceram. Soc. 104 (8) (2021) 3845–3854.
[158] L.B. Caliman, R. Bouchet, D. Gouvea, P. Soudant, M.C. Steil, Flash sintering of ionic conductors: The need of a reversible electrochemical reaction, J. Eur. Ceram. Soc. 36 (5) (2016) 1253–1260.
[159] K. Ren, Y. Cao, Y. Chen, G. Shao, J. Dai, Y. Wang, Flash sintering of Na3Zr2 (SiO4) 2 (PO4) solid-state electrolyte at furnace temperature of 700 °C, Scr. Mater. 187 (2020) 384–389.
[160] T. Clemenceau, N. Andriamady, P.K. MK, A. Badran, V. Avila, K. Dahl, M. Hopkins, X. Vendrell, D. Marshall, R. Raj, Flash sintering of Li-ion conducting ceramic in a few seconds at 850 °C, Scr. Mater. 172 (2019) 1–5.
[161] A. Sazvar, H. Sarpoolaky, M. Golmohammad, The effects of electric field on physical properties of LLZO made by flash sintering method, Solid State Ion. 386 (2022) 116054.

[162] B. Yoon, V. Avila, I.R. Lavagnini, J.V. Campos, L.M. Jesus, Reactive flash sintering of ceramics: a review, Adv. Eng. Mater. 25 (5) (2023) 2200731.
[163] V. Avila, B. Yoon, S. Ghose, R. Raj, L.M. Jesus, Phase evolution during reactive flash sintering of Li6. 25Al0. 25La3Zr2O12 starting from a chemically prepared powder, J. Eur. Ceram. Soc. 41 (8) (2021) 4552–4557.
[164] J.V. Campos, I.R. Lavagnini, V.M. Zallocco, E.B. Ferreira, E.M. Pallone, A.C. Rodrigues, Flash sintering with concurrent crystallization of Li1. 5Al0. 5Ge1. 5 (PO4) 3 glass, Acta Mater. 244 (2023) 118593.
[165] F. Liu, B. Bai, L. Cheng, C. Xu, Rapid synthesis of Li4Ti5O12 as lithium-ion battery anode by reactive flash sintering, J. Am. Ceram. Soc. 105 (1) (2022) 419–427.
[166] K. Yasui, K. Hamamoto, Comparison between cold sintering and dry pressing of CaCO3 at room temperature by numerical simulations, AIP Adv. 12 (4) (2022).
[167] K. Yasui, K. Hamamoto, Numerical simulations of reactive cold sintering of BaTiO3, J. Eur. Ceram. Soc. 44 (5) (2024) 2777–2786.
[168] D. Wang, K. Tsuji, C.A. Randall, S. Trolier-McKinstry, Model for the cold sintering of lead zirconate titanate ceramic composites, J. Am. Ceram. Soc. 103 (9) (2020) 4894–4902.
[169] A. Ndayishimiye, M.Y. Sengul, S.H. Bang, K. Tsuji, K. Takashima, T.H. de Beauvoir, D. Denux, J.-M. Thibaud, A.C. van Duin, C. Elissalde, et al., Comparing hydrothermal sintering and cold sintering process: Mechanisms, microstructure, kinetics and chemistry, J. Eur. Ceram. Soc. 40 (4) (2020) 1312–1324.
[170] M.Y. Sengul, J. Guo, C.A. Randall, A.C. van Duin, Water-mediated surface diffusion mechanism enables the cold sintering process: a combined computational and experimental study, Angew. Chem. 131 (36) (2019) 12550–12554.
[171] Y. Li, R. Torchio, S. Falco, P. Alotto, Z. Huang, R.I. Todd, Promoting core/surface homogeneity during flash sintering of 3YSZ ceramic by current path management: experimental and modelling studies, J. Eur. Ceram. Soc. 41 (13) (2021) 6649–6659.
[172] J. Li, L. Guan, W. Zhang, M. Luo, J. Song, X. Song, S. An, Sintering behavior of samarium doped ceria under DC electrical field, Ceram. Int. 44 (2) (2018) 2470–2477.
[173] S. Grasso, Y. Sakka, N. Rendtorff, C. Hu, G. Maizza, H. Borodianska, O. Vasylkiv, Modeling of the temperature distribution of flash sintered zirconia, J. Ceram. Soc. Japan 119 (1386) (2011) 144–146.
[174] I.R. Lavagnini, J.V. Campos, E.M. Pallone, Microstructure evaluation of 3YSZ sintered by two-step flash sintering, Ceram. Int. 47 (15) (2021) 21618–21624.
[175] Y. Liu, X. Huang, Effects of flash sintering parameters on performance of ceramic insulator, Energies 14 (4) (2021) 1157.
[176] K. Vikrant, H. Wang, A. Jana, H. Wang, R.E. García, Flash sintering incubation kinetics, npj Comput. Mater. 6 (1) (2020) 98.
[177] J. Narayan, Unified model of field assisted sintering and related phenomena, Scr. Mater. 176 (2020) 117–121.
[178] L. Bai, W. Xue, Y. Xue, H. Qin, Y. Li, Y. Li, J. Sun, Interfacial ion-transport mechanism of Li7 (Al0. 1) La3Zr2O12 solid electrolyte modified by using a spark plasma sintering method, Chem. Electro. Chem. 5 (24) (2018) 3918–3925.
[179] R. Serrazina, P.M. Vilarinho, A.M. Senos, L. Pereira, I.M. Reaney, J.S. Dean, Modelling the particle contact influence on the Joule heating and temperature distribution during FLASH sintering, J. Eur. Ceram. Soc. 40 (4) (2020) 1205–1211.
[180] W. Qin, H. Majidi, J. Yun, K. van Benthem, Electrode effects on microstructure formation during flash sintering of yttrium-stabilized zirconia, J. Am. Ceram. Soc. 99 (7) (2016) 2253–2259.
[181] W. Xiao, N. Ni, W. Cheng, Y. Li, C. Zheng, Y. Yu, D. Peng, Reduced interfacial stresses in laminated ceramics during flash sintering enabled by an extremely low uniaxial viscosity, Acta Mater. 246 (2023) 118688.
[182] Y. Li, Y. Zhu, N. Yan, X. Wang, Z. Jia, Model of the effect of arc on flash sintering at room temperature, in: 2022 IEEE International Conference on High Voltage Engineering and Applications, ICHVE, IEEE, 2022, pp. 1–4.
[183] M. Biesuz, V.M. Sglavo, Microstructural temperature gradient-driven diffusion: possible densification mechanism for flash sintering of zirconia? Ceram. Int. 45 (1) (2019) 1227–1236.
[184] C. Manière, C. Harnois, S. Marinel, Role of microstructure reactivity and surface diffusion in explaining flash (ultra-rapid) sintering kinetics, J. Eur. Ceram. Soc. 43 (5) (2023) 2057–2068.
[185] H. Motomura, D. Tamao, K. Nambu, H. Masuda, H. Yoshida, Athermal effect of flash event on high-temperature plastic deformation in Y2O3-stabilized tetragonal ZrO2 polycrystal, J. Eur. Ceram. Soc. 42 (12) (2022) 5045–5052.
[186] M. Yoshida, S. Falco, R.I. TODD, Measurement and modelling of electrical resistivity by four-terminal method during flash sintering of 3YSZ, J. Ceram. Soc. Japan 126 (7) (2018) 579–590.
[187] R. Serrazina, A.M. Senos, L. Pereira, J.S. Dean, I.M. Reaney, P.M. Vilarinho, The role of particle contact in densification of FLASH sintered potassium sodium niobate, Eur. J. Inorg. Chem. 2020 (39) (2020) 3720–3728.
[188] R. Serrazina, M. Gomes, R. Vilarinho, L. Pereira, J.S. Dean, I.M. Reaney, A.M. Senos, P.M. Vilarinho, J.A. Moreira, Induced internal stresses and their relation to FLASH sintering of KNN ceramics, J. Mater. Chem. C 10 (30) (2022) 10916–10925.
[189] D. Hagen, J.J. Beaman, D. Kovar, Selective laser flash sintering of 8-YSZ, J. Am. Ceram. Soc. 103 (2) (2020) 800–808.
[190] D. Hagen, J.J. Beaman, D. Kovar, Effects of interparticle neck size on initiation of selective laser flash sintering of 8-YSZ, J. Am. Ceram. Soc. 105 (10) (2022) 6023–6040.
[191] D. Hagen, J.J. Beaman, D. Kovar, Mechanisms responsible for the onset of selective laser flash sintering of 8-YSZ, J. Am. Ceram. Soc. (2023).
[192] I. Mazo, B. Palmieri, A. Martone, M. Giordano, V.M. Sglavo, Flash sintering in metallic ceramics: finite element analysis of thermal runaway in tungsten carbide green bodies, J. Mater. Res. Technol. 23 (2023) 5993–6004.
[193] M. Abedi, A. Asadi, S. Sovizi, D. Moskovskikh, K. Ostrikov, A. Mukasyan, Electrical and heat distributions and their influence on the mass transfer during the flash spark plasma sintering of a Cu/Cr nanocomposite: Experiments and numerical simulation, Materials 15 (20) (2022) 7366.
[194] O. Guillon, W. Rheinheimer, M. Bram, A perspective on emerging and future sintering technologies of ceramic materials, Adv. Eng. Mater. 25 (18) (2023) 2201870.
[195] Y.B. Song, K.H. Baeck, H. Kwak, H. Lim, Y.S. Jung, Dimensional strategies for bridging the research gap between lab-scale and potentially practical all-solid-state batteries: The role of sulfide solid electrolyte films, Adv. Energy Mater. 13 (32) (2023) 2301142.